NORTHWESTERN UNIVERSITY

Multi-Scale Assessment of the Role of the Particle Shape on the Crushability of Sand

A DISSERTATION

SUBMITTED TO THE GRADUATE SCHOOL
IN PARTIAL FULFILLMENT OF THE REQUIREMENTS

for the degree

DOCTOR OF PHILOSOPHY

Field of Civil and Environmental Engineering

By

Dawa Seo

EVANSTON, ILLINOIS

August 2022

ABSTRACT

Granular materials consisting of discrete particles, are a pervasive material in nature and play a major role in disparate fields of science and technology. To control and manipulate the granular materials in engineering, enriching our understanding of their fundamental characteristics and mechanical behavior is crucial. In this context, one of the major challenges concerning particulate materials composed of fragile particles is their response at high pressure. The extreme conditions cause the evolution of size and shape of their grains, a phenomenon referred to as breakage. The evolving particle-scale attributes induce the critical change in rearrangement of microstructures leading to macroscopic deteriorations, affecting the safety and serviceability of the granular system. Therefore, it is essential to comprehend the effect of size reduction and shape alterations in crushable granular materials at the multi-scale mechanics. The goal of this study is therefore to enhance our understanding of crushable granular materials mechanics, especially in light of the effect of particle shape and the evolution of shape attributes under continuous breakage.

In this thesis, first, high-pressure compression tests with concurrent 3D X-ray tomography were conducted at assembly scale with two different morphological types of sand. The attained digital images during the experiments were used in conjunction with a tracking algorithm able to quantify the consecutive response of sand grains. The tracking algorithm, for example, allowed the isolation of the individual breakage events and the quantification of number and geometry of the fragments resulting from each grain rupture in the packed sand experiencing collective comminution.

Furthermore, the shape-dependent breakage models at grain scale were proposed to predict the failure strength of crushable grains with particle-scale attributes, size, and shape. The performance

of the proposed models was assessed with the measured particle failure strength through the diametral compression test which was conducted on single particles of varying size and shape.

Moreover, a level-set discrete element method was used to replicate the oedometric compression test to investigate the evolving response of stress distribution in the assembly of a crushable granular system. With the benefit of computational modeling, the role of geometric modelling in a discrete element method was examined to evaluate the optimal level of particle geometry representation. Furthermore, the virtual laboratory experiments were examined to validate the possibility of attaining ultimate size and shape attractors. The conclusion summarizes the main findings of the thesis and discusses the possible direction of applicable contribution of this thesis and future research.

ACKNOWLEDGEMENTS

Countless people supported my research efforts toward the doctoral degree at Northwestern University. First and foremost, I am extremely grateful to my supervisor, Dr. Giuseppe Buscarnera. He has not only provided invaluable advice, continuous support, and patience, but also cultivated my fundamental knowledge during my PhD study. Under his outstanding supervision, I have had invaluable opportunities in my academic career and his guidance helped me throughout the research and writing of this thesis. Besides my advisor, I would like to thank the rest of my thesis committee: Dr. James Hambleton, Dr. Alessandro Rotta Loria and Dr. Gianluca Cusatis for their supports and appraisals. Their insightful comments, encouragement and discussion have expanded my comprehensive understanding in geotechnical engineering. I am indebted to my colleagues, Dr. Changbum Sohn and Dr. Mehmet Burak Cil for sharing their expertise and experience during the several stages of this research. Special thanks to: Dr. Cino Viggiani, Dr. Alessandro tengattini and Dr. José Adrade. Their kind support made my study and life in Univ. Grenoble Alpes, France and Caltech a wonderful time. Dr. Mark Rivers for hands-on assistance to the use of synchrotron X-ray microtomography at 13-BM-D facility of the Advanced Photon Source in Argonne National Laboratory, Illinois. Without his precious support it would not be possible to conduct this research. I would like to thank my friends, lab mates, colleagues, and research team, especially in AG32, for the sleepless nights we were working together before deadlines, and for all the fun we have had in the last five years. Lastly, my family deserves endless gratitude: my parents and my brother for supporting me spiritually throughout my life and writing this thesis.

LIST OF NOTATIONS AND ABBREVIATIONS

Latin Symbols

a', b': collective coefficient in particle fracture energy models

a, b : the long and short semiaxes of elliptical area of contact

a_c : contact radius

$\overline{AR}$, AR_p : the mean and mode of the aspect ratio frequency

B : breakage value or index

B_0 : the reference breakage index

B_t : current breakage integral

B_p : total breakage integral

$\dot{B}$: breakage growth rate

C_u : the coefficient of uniformity

ΔC_u variation of coefficient of uniformity

d : diameter of a given particle

d_0 : diameter to have a 37% survival probability at that state

d_d: distance from discretized point to surface

D_{50} : median grain size

D_{eq} : equivalent volumetric diameter

D_p : particle diameter

$D_{p,mode}$: the modal value of Particle diameter

e, e_0 : void ratio

E : elastic modulus

E_B : breakage energy

E_c : critical breakage energy

E_{pc} : particle fracture energy per unit volume

E^* : an equivalent elastic stiffness

F : force at failure

F_0 : initial cumulative grain size distribution

F_c : contact force

$F_{current}$: current cumulative grain size distribution

F_f : failure load in single particle for diametral compression test

F_n : normal contact force

F_u : ultimate cumulative grain size distribution

G_{IC} : critical energy release rate

k_n , k_s: normal and shear stiffness

K , G : bulk and shear modulus

K_I : stress intensity factor at mode I

K_{IC} : critical stress intensity factor of mode I crack

l , l_0.: the mean shortest-path distance and initial value of the mean shortest-path distance

L, I, S : the longest, intermediate and shortest length

L_0, I_0, S_0 : the reference value of the longest, intermediate and shortest length

m : the Weibull modulus

M: slope of critical state line in p-q space

n : porosity

n : the stress corrosion value

p: mean stress

p_d, p_{di} : surface discretized point

P_f : the probability of failure based on Weibull's theory

q: deviatoric stresses

r_x , r_y : the radius of curvature of single particle contacting to a rigid plate

R : particle radius

SA : surface area of particle

V, V^P: particle volume

$V_{largest\ child}$: volume of the largest child particle belonging to one parent particle

V_{parent} : volume of parent particle

w : the Weibull modulus

w' : a power law coefficient determined from data-driven fashion

x_c : branch vector

y_B : yield function

z, z_0 : mean degree and initial value of mean connectivity

Greek Symbols

α : fractal dimension

α_f : cumulated fragments produced by an individual crushed particle

$\bar{\alpha}_f$: average number of cumulated fragments produced by crushed particles

β_f : new fragments generated by an individual particle upon a loading increment

$\bar{\beta}_f$: average number of new fragments generated upon a loading increment

δ : displacement by contact

δ^* : a dimensionless contact deformation

ε, ε_d : strain at initiation of breakage

ε_p : prediction error

$d\varepsilon_{ij}^{vp}$: the rate of viscoplastic strain tensor

$\mathcal{F}(\kappa)$, $\mathcal{E}(\kappa)$: complete elliptic integrals of the first and second kinds

ξ : scaling factor

κ : ellipticity parameter

μ : friction

N_f^i : number of fragments generated by a broken particle

N_{pj} : number of crushed particles identified at step 'j'

N_{nf}^{i} : number of newly generated fragments at a given loading step 'j+1'

N_{np}^{i} : number of particles at step 'j' which will generate fragments at the subsequent step, 'j+1'

ρ : density of a single particle

ρ_x , ρ_y : two contact curvatures of single particle contacting to a rigid plate

σ : current stress of a given particle

σ^{max} : the maximum principle stress

σ_{c0} : stress to have a 37% survival probability at that state

σ_{model} : the strength predicted with each model with the average AR and D_p from measured values of each batch

$\bar{\sigma}^{p}$: average particle characteristic stress

$\sigma_{pc,0}$: particle strength

σ_t : the tensile stress at the surface contact

σ_{tc} : the tensile stress initiating crack growth

σ_{test} : the average strength belonging to each batch of tested materials

σ_y : macroscopic yield stress

ν : poisson ratio

φ, φ_i : discrete level set

ϕ : the porosity field

Φ : the rate of energy dissipation of the system

ω : breakage-friction coupling angle

Abbreviations

2D : two-dimensional/ dimension

3D : three-dimensional/ dimension

ANL : Argonne National Laboratory

AR : aspect ratio

AR_i : batches classified into their aspect ratio

AR_{avg} : the average value of Aspect Ratio

BC : betweenness centrality

CCD : charge coupled device

CT-FE : the computerized-tomography to finite-element

DEM : discrete element method

dDIC : discrete digital image correlation

DIC : digital image correlation

EI : elongation index

EI_0 : reference value of the Elongation index

FE : flatness-elongation ratio

FI : flatness index

FI_0 : reference value of the Flatness index

GSD : grain size distribution

IDL : interactive data language

LS-DEM : level-set discrete element method

LVDT : linear variable differential transformer

MIE : moment of inertia ellipsoid

MVB : minimum volumetric box

MVE : minimum volumetric ellipsoid

REV : representative elementary volume

SEM : scanning electron microscope

SMT : synchrotron microtomography

This thesis is completely dedicated to my family, Yeongman Seo, Jaeyoung Seol, and Joohyung Seo, whose love and unconditional support helped to accomplish my work with truthful self-confidence.

TABLE OF CONTENTS

LIST OF FIGURES

LIST OF TABLES

Chapter 1. INTRODUCTION

Granular materials play a crucial role across a wide range of industrial applications, including civil engineering, mining technology and the energy sector (Yang et al., 2010; Arshad et al., 2014). A challenge concerning particulate materials consisting of brittle particles is the evolution of the size and shape of their grains when subjected to high pressures, a phenomenon often referred to as breakage. The crushing of brittle grains is among the primary causes of changes in surface area, porosity, and physical properties of granular solids subjected to high pressure. The implications of grain crushing, such as size reduction and shape alteration, may deteriorate the stability of underground systems subjected to burial, penetration, and impact, with major consequences for the safety and serviceability of the affected systems. For example, variations in particle-scale features may cause the early-stage sediment compaction, which leads to upper crustal deformation, permeability and deterioration of the long-term performance of rockfill dams and railway ballast (Chuhan et al., 2003; Antonellini et al., 1994; Chester et al., 2004; Alonso et al., 2011). In this context, the intricacies of the mechanics of crushable sands motivates the extensive efforts made to explore the grain-scale processes contributing to their macroscopic behavior via experimental, analytical, and numerical methods, especially when the goal is to elucidate the role played by the complex initial and evolving morphology of their particles.

For example, modern experimental techniques based on high-resolution imaging (e.g., 3D X-ray tomography) allow observation of geometric changes of the scanned systems while simultaneously acquiring mechanical response data. The increasing application of these techniques in conjunction with micromechanics therefore opens a new era for geotechnical modeling. In fact, thanks to the access to 3D digital imagery of individual particles, numerous advanced shape descriptors have

been proposed to quantify the particle form (e.g., sphericity, aspect ratio) and surface textures (e.g., roughness). Numerous studies explored the role of the shape of the particles on continuum-scale properties such as stiffness (Cho et al., 2006), as well as with reference to how contact configuration and fracture types affected the onset of breakage (Zhao et al., 2015; Karatza et al., 2019). Those studies revealed that shape analyses for brittle granular materials should be given priority to comprehend their micromechanics. However, most breakage studies considering shape effects are still limited to individual particles or to the first occurrence of breakage. The evolving features of the grains (e.g., fragment morphology, fracture modes) have instead received less attention, especially in the context of constitutive laws.

Among the available continuum frameworks, Breakage Mechanics has been proposed to connect the distributed rupture of brittle grains and the development of permanent porosity changes (Einav, 2007). However, this approach assumed spherical grains, thus restricting its applicability real sands made of particles exhibiting deviations from perfect sphericity (Zhao et al., 2015). To consider the effect of non-spherical particle geometries, different contact and fracture modes at particle level were proposed and an upscaling law bridged that micromechanics with continuum model (Zhang et al., 2016). However, most of these fracture laws include size as the only geometric descriptor influencing the particle resistance, thus excluding shape descriptors. Furthermore, one of the most commonly ignored effects of the particle shape is its ability to cause non-negligible crushing prior to the standard yielding point, thus severely affecting both elastic and inelastic properties (Karatza et al., 2019). These phenomena require thorough examination in order to identify their grain-scale origin and explain how their effect propagates across length scales.

This thesis is motivated by these premises and aims to enhance our understanding of the breakage of granular materials in light of particle shape effects. The research work discussed in the following chapters has the goal to characterize the evolution of breakage in individual particles, as well as how breakage events can emerge in distributed form across an assembly of packed grains. Changes of particle shape indicators upon breakage will be tracked and quantified through a 3D tracking algorithm specialized for the analysis of grain breakage processes. Furthermore, such indicators will be used to feed micromechanical models of contact deformation and fracture, with the goal to estimate a shape-dependent energy threshold for breakage initiation in single particles. In this context, the recently proposed model by Zhang et al (2016) considering only particle size effects on crack growth and breakage dissipation will be used as a reference. To build a comprehensive understanding of the mechanical response in a crushable granular continuum, assembly-scale simulations will be performed to examine how the shape of the particles affects force transmission and grain kinematics. Such analyses will be based on a Level-Set Discrete Element Method (LS-DEM). Furthermore, preliminary results illustrating the potential of linking the digital data analysis methods formulated in this thesis will be briefly discussed with reference to the construction of a network model and the incorporation of digital datasets into the workflow of finite element models based on Continuum Breakage Mechanics models. In summary, the goals of this thesis can be summarized as follows:

1. To assess the evolution of different grain-scale attributes (e.g., size, shape, and fracture mode) of sand grains subjected to oedometric compression tests by means of laboratory experiments assisted by in-situ 3D X-ray tomography scans.

2. To examine quantitatively the microscopic mechanical response of granular materials through a novel 3D tracking algorithm specialized for particle breakage, thus enabling the use of digital technologies to guide mechanics-based modeling techniques for crushable granular media.
3. To develop closed-form analytical models able to quantify the crushing strength of individual particles as a function of shape descriptors.
4. The replicate computationally the interparticle contact interactions emerging during the high-pressure compression of sand by means of DEM simulations based on exact virtual replicas of the tested sand grains replicated via level-sets (LS-DEM), as well as to use the calibrated model to infer the possibility for the size and shape of crushed particles to converge towards ultimate attractors emerging under extreme pressure levels.

The thesis is structured as follows. Chapter 2 discusses the laboratory experiments available to explore particle-scale and assembly-scale breakage in granular media. In addition, the analytical and theoretical frameworks available to study shape effect in granular materials through digital image analysis and computational modeling are introduced. Chapter 3 outlines the characteristics of the testing methodology and the tested materials in the context of laboratory experiments conducted in conjunction with in-situ 3D X-ray tomography. Chapter 4 presents a novel algorithm able to process digital images collected from 3D X-ray tomography scans and aimed at quantifying microstructure evolution and sequence of breakage events during confined compression. Chapter 5 assesses the crushing behavior of granular materials by comparing assemblies having different particle sizes and shapes. Oedometer test are carried out through a custom-designed compression apparatus to capture sequential response under continuous breakage at the sample-scale. In Chapter 6, failure models for non-spherical particles are proposed by considering multiple contact scenarios and failure mechanisms. To validate the performance of those proposed analytical models, a series

of diametral compression test is conducted at particle-scale by quantifying the particle-scale attributes through X-ray scans. Chapter 7 discusses the computational assessment of crushing in granular materials through LS-DEM simulations by using particle replicas generated from the 3D tomography images. To illustrate the opportunities opened by this particular combination of digital model initialization and computational method, the crushing behaviors is examined by using the output of the model to infer quantities not accessible from direct visualization (e.g., contact forces). Finally, Chapter 8 highlights the key findings of this thesis and suggests potential future directions for this research area.

Chapter 2. TECHNICAL BACKGROUND

2.1 Effect of the Particle Shape on Crushable Granular Materials

The grain morphology influences the performance of geotechnical infrastructures and energy geosystems (Brzesowsky et al., 2014; Oldecop and Alonso, 2001; Yang et al., 2010). The particle shape also influences the mechanical behavior, from particle-scale interactions such as force transfers to macroscale deformation (Santamarina and Cho., 2004). Specifically, it has shown that the grain geometry determines microscopic slip, contact deformation, rotation and arrangement (Mair et al., 2002; Anthony and Marone, 2005), with effects that propagate across the entire system to vary bulk density, flowability, compaction and strength (Antonellini et al., 1994; Radjai et al., 1999; Goldenberg and Goldhirsch, 2005). One of the most common ignored effects of the particle shape is its ability to cause non-negligible crushing prior to the standard yielding point, thus severely affecting both elastic and inelastic properties in the granular system (McDowell and Bolton, 1998; Coop et al., 2004; Brzesowsky et al., 2014). For example, assemblies made of spherical grains tend to transition sharply from elastic to plastic compaction, while angular particles produce a smoother transition (Nakata et al., 2001). Furthermore, in the context of plastic deformation, assemblies with flaky or elongated particles have been found to suffer more severe degradation and larger deformation upon loading compared to sands consisting of round grains (Alonso et al., 2011). Despite such recognition of the relevance of particle shape effects, most existing continuum theories for engineering applications either do not account explicitly for the geometry of the particles or only encompass the particle size as a unique descriptor of the grain geometry.

In this context, a challenge in crushable granular system is the evolution of the size and shape of their grains under breakage. The variation in size and shape of particles by breakage induces redistribution of local stress with, as well as variations in contact fabric. This effect extends to the macroscale response leading to changes in compressibility and shear strength (Pestana and Whittle 1995; Marsal 1967). In nature, such effects can be found in multiple settings, such as during the early-stage sediments compaction, upper crustal deformation, permeability change, infrastructure deterioration, and ground instability (Chuhan et al., 2002; Antonellini et al., 1994; Chester et al., 2004). Those responses in granular materials motivate extensive scientific efforts to explore the granular mechanics with the evolving particle-scale features under continuous breakage, the goal of this study is therefore to enhance our understanding of the breakage of granular materials especially in light of particle shape effects.

2.1.1 Particle shape descriptors and their quantification via digital image analysis

During the last few decades, the quantification of the particle shape and the analysis of its role on the mechanical response of granular materials has been studied extensively through digital image analysis. Due to the limited capacity of imaging technologies and the use of simple measurement techniques, numerous studies have applied 2D shape descriptors defined based on 2D projections collected from scanning electron microscopes (SEM) or photographs (Blott and Pye., 2008; Li et al., 2016). However, 2D methods are dependent on planar projections of the object of interest, thus introducing inconsistencies in the quantitative assessment of the value of shape descriptors (Zhao and Wang, 2016). For example, discs or cylindrical forms can appear identical to spheres if their geometry is projected on a plane parallel to their cross-section, while result into obviously different geometries such as flat or rectangular shapes if projected on planes perpendicular to the cross section. This example highlights the inherent limitations of 2D imaging. Regarding this point,

three-dimensional features of particle shape have been studied and measured by X-ray tomography or 3D laser scanner, by benefiting from the rise of new technologies over the last decades (Zhao et al., 2015; Seo et al., 2020; Zheng et al., 2020).

Generally, the particle geometry is described with three important scales at particle level: global form, roundness, and surface texture, as described in Figure 2.1a (Barrett., 1980; Mitchell and Soga., 2005; ISO., 2008). Those three shape scales are independent descriptors as each scale value can be various regardless the change in other scale descriptors (Wadell, 1932; Barrett, 1980.; Cho et al., 2006). The overall form of a particle can be readily described through its principal lengths (i.e., longest length (L), intermediate length (I) and shortest length (S), $L \geq I \geq S$) by measuring these lengths with respect to a particle-specific Cartesian coordinate system (Blott and Pye., 2016). Standard examples of particle form descriptors are sphericity, elongation (I/L), flatness (S/I), and aspect ratio (AR = S/L), see Chapter 4 for more details.

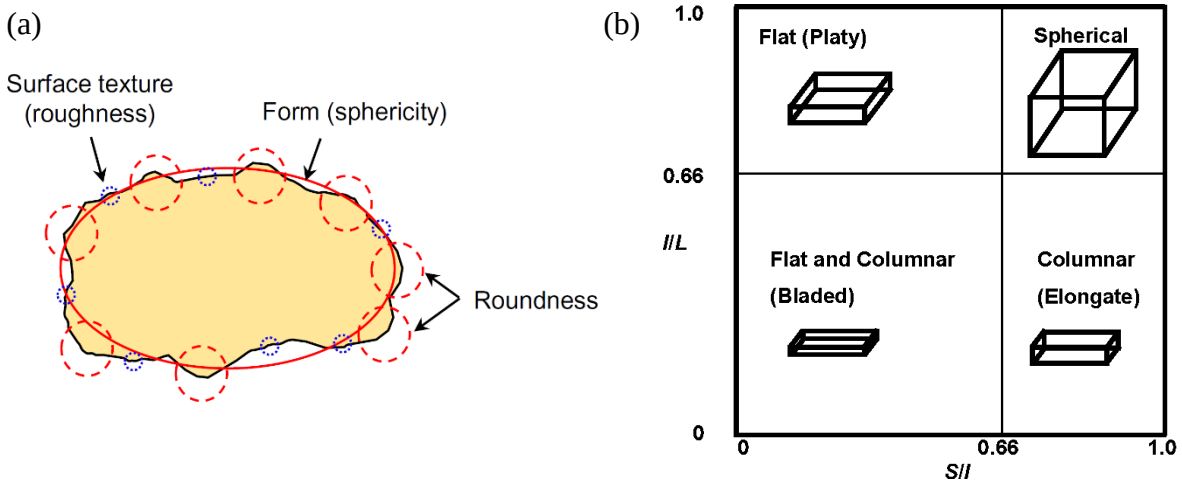

Figure 2.1. (a) Particle shape descriptors at different scales (Zheng & Hryciw., 2015) (b) Zingg plane (redrawn from Zingg, 1935, alternative descriptors in brackets selected from Blott and Pye, 2008) (Pen et al., 2013)

With form descriptors, particles can be classified into different classes by setting threshold values for selected sets of shape indicators. A classic example widely used in sedimentology is the so-called Zingg plane (Zingg, 1935), introducing four shape classes (i.e., spheroid, oblate, prolate, and blade) depending on the values of EI and FI with respect to a threshold reference number of 2/3 (i.e., spheroids involve elongation >2/3; flatness > 2/3) in Figure 2.1b. Another representative descriptor of the particle form is sphericity, i.e., a quantity reflecting how closely the shape of an object resembles a perfect disk/sphere (Wadell, 1932). All the above descriptors have a range from 0 (i.e., flat/elongated) to 1 (i.e., spherical). The second scale of interest to quantify the shape of particles is the roundness, addressing lower-scale irregularities not affecting the overall particle form (e.g., angularity and presence of sharp corners). Roundness quantification typically involves the computation of local curvatures at the surface of particles. This value is based on two-dimensional projected area of the particles and reflects morphological features of the corners as a ratio of the average radius of curvature of the particle corners to the radius of the maximum inscribed circle (Wadell, 1932), the details in Chapter 4. Figure 2.1a shows an example of geometric irregularities affecting the particle roundness at major corners along with the geometric features defining the particle form. This feature can be changed by weathering or abrasion without impacting the form (Zhao and Wang., 2016). Finally, the smallest length scale of shape irregularities is the surface roughness, i.e., a metric of the surface texture of a particle (Zhao and Wang., 2016) requiring very high imaging resolution. Although surface roughness has been found to play a role in soil properties, such as interparticle friction (Sandeep and Senetakis., 2018; Yao et al., 2021), it is typically inaccessible with common high-resolution imaging techniques and its quantification has been considered outside of the scope of this thesis. In this sense, most studies have focused on particle form and roundness. However, despite the abundance of characterization

methods defining the intrinsic particle shape and its effects on the mechanical response of granular systems, morphological features are rarely incorporated into geomechanical models due to the difficulty of bridging the influence of the particle shape with the macroscopic deformation behaviors of granular materials.

2.1.2. Laboratory experiments quantifying particle shape effects in sand

Numerous experimental works have explored particle shape effect at both micro and macro scales. Cho et al. (2006) studied the packing density and the strain response influenced by particle shape of sand and shows that the more angular sands tend to have higher void ratio and decrease in stiffness (Figure 2.2). Also, Yang and Luo (2015) presented shape parameters (i.e., AR, sphericity, overall regularity, and convexity) influences the critical properties (i.e., effective stress ratio, critical state friction angle, void ratio intercept and the slope of the critical state locus). Specifically, in undrained and drained tests with same effective confining stress and void ratio, particles with high regularity reduced the intercept and the slope of the critical state locus and were more susceptible to liquefaction due to the decrease in the required void ratio. In the context of particle breakage, the relevance of shape effects has been widely recognized. Hiramatsu and Oka (1966) found non-negligible difference of material strengths between irregular solid and spheroidal glass and insisted the 0.9 times critical load of spherical grain can be considered as the tensile strength of irregular solid. In agreement with this finding, Tang et al. (2001) observed that disk tends to have 21 % higher maximum load than irregular particles, in that irregularly shaped solids may deform due to more severe tensile stress concentration within the solid and this triggers crack initiation extensively. With novel techniques such as 3D X-ray tomography, substantial efforts have been made to quantify the morphological variables affecting the initiation of particle breakage and its evolution (Zhao et al., 2015; Karatza et al., 2018). Karatza et al. (2019) explored the

correlation between broken particles and their sphericity in the assembly and found more breakage in flatter grains under oedometer compression test as shown in Figure 2.3. Similarly, other studies found that specimens consisting of angular particles displayed more breakage than an assembly with round sand at the similar particle size (Sohn et al., 2017; Zhu and Zhao, 2019).

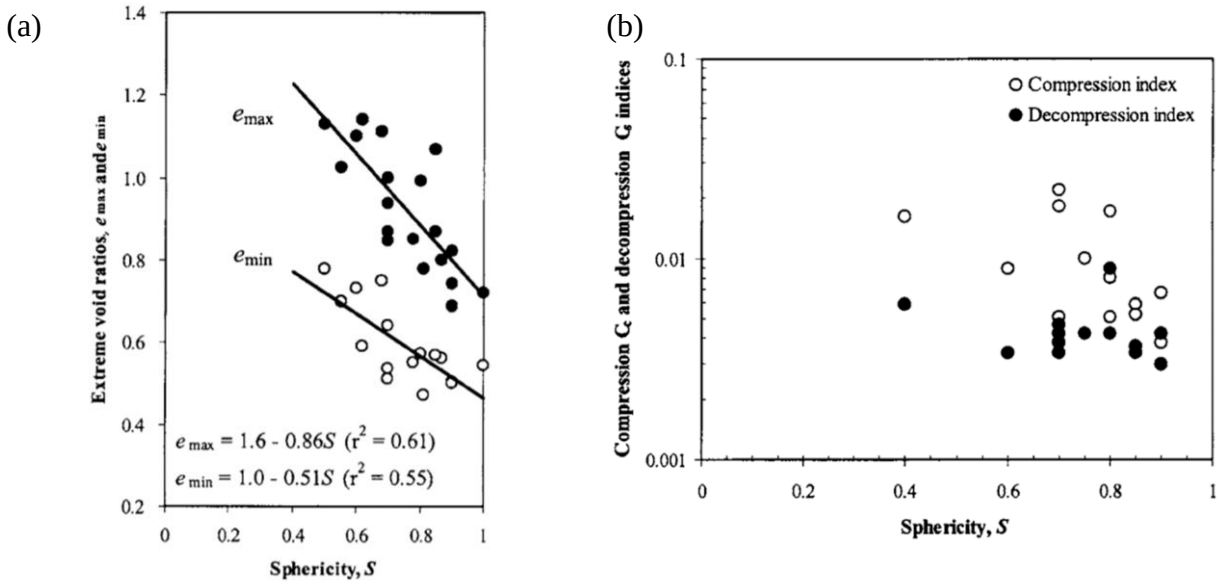

Figure 2.2. Effect of particle on (a) maximum and minimum void ratios and (b) compression and decompression coefficients measured with oedometric loading/unloading tests (Cho et al., 2006)

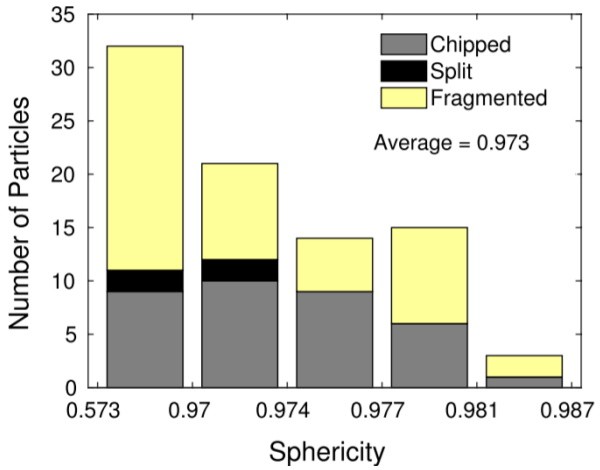

Figure 2.3. Effect of the particle sphericity on the collective breakage of packed sand specimens (Karatza et al., 2019)

2.1.3 Theoretical models of shape dependency

Despite the important role of the geometry of particles documented by experiments, most theoretical models for the crushing of individual grains and assemblies consider only the particle size in their computations, thus excluding shape effects from their analyses. Therefore, the challenge is to extent constitutive laws by incorporating the effect of the particle shape on grain fracture responses through measurable geometric attributes of natural and/or engineered particles.

In the context of continuum-scale constitutive laws for brittle particulate materials, Breakage Mechanics is a widely used framework (Einav, 2007; Zhang et al., 2016; Buscarnera and Einav., 2021). Rooted on methods of continuum thermodynamics, this approach uses analytical expressions of stored elastic strain energy and breakage dissipation to formulate constitutive equations describing the stress-strain behavior of a granular material subjected to high pressure, along with the evolution of the grain size distribution (GSD). In this framework, grain fracture processes are quantified through a new internal variable, Breakage, B, measured on the basis of the relative proximity of the current GSD from the initial (B_0) and ultimate distributions (B_t), quantified as Eq. (2.1), to consider the evolving GSD as described in Figure 2.4.

$$B = \frac{B_t}{B_p} \tag{2.1}$$

The residual breakage energy, i.e., the amount of elastic strain energy stored in the system and available for further crushing, is used to define a dissipation equation. When the energy released upon the evolving GSD, the breakage energy reaches a critical threshold, macroscopic yielding occurs. However, this approach has been established based on the assumption of either circular or spherical particles and pursued mainly by expressing the size effect rather than the role of the grain morphology.

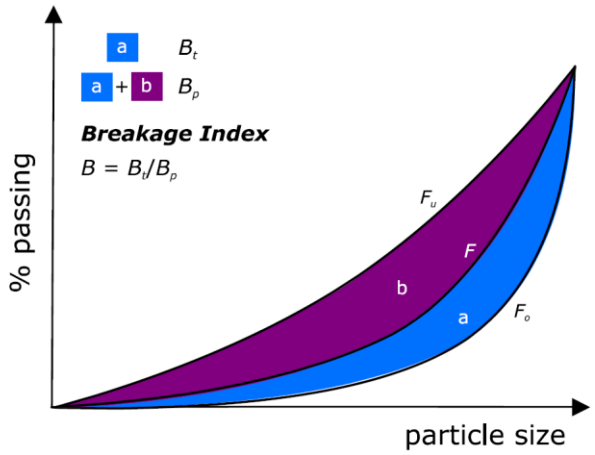

Figure 2.4. Definition of the breakage index, *B* (Einav, 2007)

To overcome these limitations, upscaling techniques can be used to bridge the micromechanics of grain fracture to continuum scales, in that grain-scale phenomena impacts the constitutive properties, such as yield pressure and plastic compressibility (McDowell and Bolton., 1998, Coop et al., 2004, Brzesowsky et al., 2014). An example is the work by Zhang et al. (2016), who used an energy scaling hypothesis to integrate breakage and fracture mechanics based on the grain-scale contact models (e.g., linear, Hertzian or conical contacts; Goddard., 1990; Jäger., 1999; Timoshenko and Goodier., 1951) and fracture criteria (e.g., central split, contact cracks or Weibull failure; Timoshenko and Goodier., 1951; Hiramatsu and Oka., 1966; Nakata et al., 1999) (Figure 2.5). Contact models were used to quantify the elastic strain energy stored within individual particles prior to a fracture event depending on the deformation between a grain and a rigid plate (e.g., flat, spherical and conical contacts in Figure 2.5a, 2.5b and 2.5c), while fracture criteria were used to quantify the maximum compressive force applicable to the particle prior to the generation of a tensile crack along its median axis or at its point of application (Figure 2.5d and 2.5e). In addition, failure conditions were also interpreted statistically through the Weibull's weakest link theory of flaws distributed randomly within the volume (Figure 2.5f).

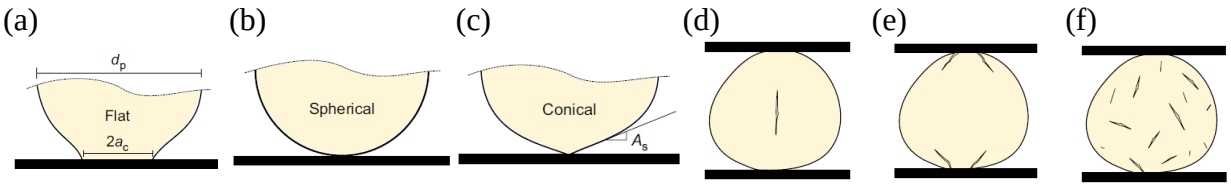

Figure 2.5. Schematic diagram of contact models: (a) flat (b) spherical (c) conical contact, and failure models: (d) centre (e) contact (f) random crack (Zhang et al., 2016)

Sohn et al. (2017) verified through laboratory experiments the ability of the suggested contact models to explain crushing mechanisms in sands with different particle shapes, finding that data for irregular quartz sand were well captured by contact crack models, while those for spherical glass beads were well replicated by a central fracture model, as shown in Figure 2.6. Notably, this result was found to be valid both at the scale of individual particles and for sand assemblies undergoing collective breakage.

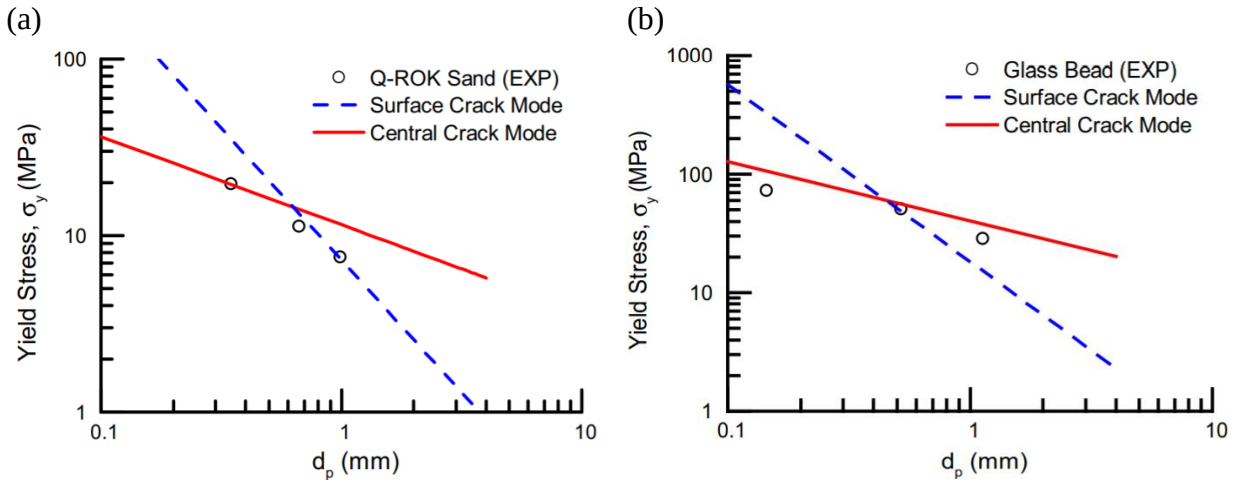

Figure 2.6. Correlation between the average particle size and macroscopic yielding stresses upon oedometric compression for (a) angular Q-ROK sand and (b) spherical glass beads with the corresponding performance of both contact and central fracture models (Sohn et al., 2016)

In this analysis, the critical breakage energy for the assembly was calculated from the particle fracture energy with packing porosity, n, and a scaling factor, ξ (Eq. 2.2).

$$E_c = (1 - n)\xi E_{pc} \tag{2.2}$$

$$\frac{E_B}{E_c}(1-B)^2 + \left(\frac{q}{Mp}\right)^2 - 1 \leq 0 \tag{2.3}$$

With the system-scale breakage energy and the breakage index, the clastic yielding at continuum scale was determined with stress ratio, *M*, mean stress, *p*, and deviatoric stresses, q in Eq. (2.3). However, even with this upscaling approach, most models for granular materials are based on energy dissipation methods associated with only the particle size.

With analogy with this case, previous studies have taken into account the shape-dependency with an indirect strategy based on size-dependent models. Brzesowsky et al. (2011) suggested an empirical model for non-spherical grain failure force on the basis of Hertzian contact mechanics with the size of pre-existing flaw size and surface curvature. This work concludes that model considering surface asperities explained better the measured grain failure for non-spherical grains rather than Weibull weakest link model derived from volume-dependent flaw. However, sphericity and roundness of tested materials display a similar relation between radius of curvature and size, there is no clear physical distinction between shape and size dependency in the particle strength. Regarding statistical models considering geometry of the tested specimen, an example is the modified Weibull theory proposed by Lei et al. (2019), where the length-to-diameter ratio is used to quantify changes in the tensile strength statistics. However, this method is limited to 2D applications, in that it does not allow the use of three-dimensional descriptors of the particle geometry. It is thus apparent that augmented analytical models accounting for the 3D particle geometry are required to explain and quantify how changes in particle shape influence the crushing resistance of individual particles and the collective crushability of sand specimens.

2.2 X-ray Microtomography Image Analysis

While the significant role of the particle shape in the behavior of granular materials has been widely recognized, a standardized study of particle shape effects and underlying micromechanics has been unavailable due to the difficulty to address their complex features systematically. With this regard, X-ray tomography has been used in conjunction with laboratory tests to resolve simultaneously macroscopic behavior and microstructural changes. A non-destructive technique, x-ray tomography imaging allows the quantification of sand microstructure, including particle and pore morphologies, their spatial distribution and connectivity, previously not accessible without interrupting the experiment (Farber et al, 2003).

To quantify the movement of each grain in an assembly with successive scans, image analysis methods have been developed especially by using tomography technologies and its analysis methods. For example, Digital Image Correlation (DIC) detects the variation in the system by paring the highest normalized mean greyscale value in the searching window between two sequential images (Tudisco et al., 2017). With those correlated windows, DIC defines the spatial coordinates of the deformation. To detect the broken particles, discrete DIC techniques (dDIC) have been applied by exclusively correlating the segmented particles. In this manner, failed attempts at correlating particles were considered as breakage events, as shown in Figure 2.7 (Karatza et al., 2019). Another strategy is ID-tracking identifying each grain based on their own features, such as geometry and initial location, and matching them in successive images. Ando et al (2012) compared the two classes of image analysis and concluded that ID-Track provides a significantly faster performance than DIC due to the use of comparison methods based on quantifiable metrics rather than using correlation features of the image itself.

By applying the image analysis method, previous studies have characterized microscale response for significant macroscale events (Andò et al., 2012, Karatza et al., 2018). For example, the initiation and evolution of shear bands was explored by quantifying local changes and it was found that the full development of a shear band started from a single point with significant breakage characteristics in the deformation zone (Alikarami et al., 2015 and Karatza et al., 2019). Hurley et al. (2018) explored the correlation between particle breakage and distribution of force by assembly-scale experiments with concurrent synchrotron X-ray microtomography (SMT). It was found that stresses in grains prior to fracture vary widely across the sample, as well as those fractured grains experience forces statistically higher than those of intact grains. With the benefit of quantitative data, breakage of single particle under compression was explored with different types of sand to comprehend fracture patterns and evolution of shape parameters (Zhao et al., 2015). This study verified that more complex geometry and internal microstructures led to much richer fragments, while the result is restricted to single particles and qualitative observation. Under

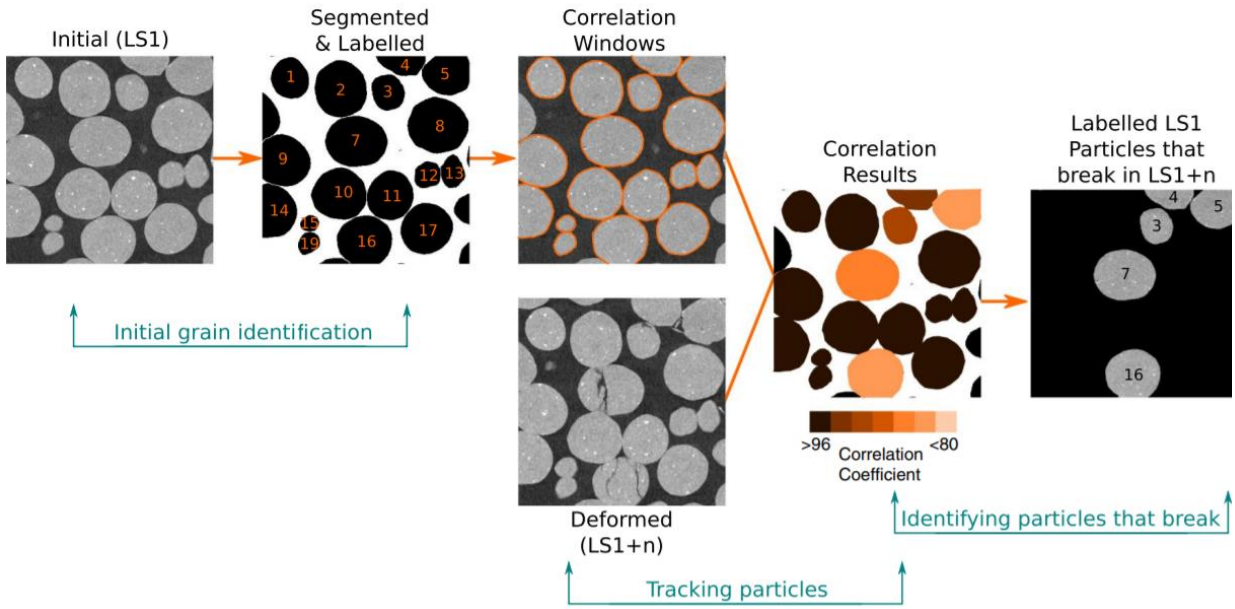

Figure 2.7. Schematic of dDIC algorithm with the broken particle colored in light color (Karatza et al., 2019)

oedometric compression, the different fracture types at the onset of particle breakage appeared depending on the heterogeneity of the particle morphology, as described in Figure 2.3. However, the evolution of the fracture patterns and fragment features has never been addressed despite its importance under on-going breakage (Einav, 2007). In summary, advanced image analysis desired for particle breakage is and it is required to comprehend shape effects on evolving state of crushable particulate systems.

2.3 Discrete Element Modeling for Crushable Granular Materials

2.3.1 DEM for brittle materials

Computational modeling has led to unprecedented progress in the numerical analysis of granular materials. It has provided us with extensive information and deeper insight into the behavior of granular media, especially by providing access to quantities that are not directly obtainable from experiments (e.g., contact forces). Discrete Element Modeling (DEM), originally proposed by Cundall and Strack (1979), has been widely used as a numerical method for granular materials. One of the challenges that DEM faces today is how to accurately account for the complicated shapes of arbitrary particles in the modelling, and to implement particle breakage in classical DEM, where each particle is a sphere. A common strategy to address this problem involves each particle being represented by smaller spheres bonded together (Cil and Alshibli, 2014, Cheng et al., 2003). Using this technique, Cil et al. (2019) simulated breakage via DEM by applying a linear parallel bond model to generate each particle, to which a Hertzian interparticle contacts behavior was assigned (Figure 2.8). The study showed the particle-size dependence of the yielding stress, with a satisfactory match between simulations and experimental results, despite the challenges in replicating the real particle shape and packing conditions. Specifically, such strategy requires large

number of small particles to describe accurate shape of fragments under continuous breakage and this requires high computational costs. A different strategy to simulate breakage in DEM frameworks involves replacing a particle with smaller spherical units modeling the fragments produced by a breakage event. While simpler, this strategy involves complications related with the choice of the number of replacement particle, the loss of mass, and the destabilization of the assembly during the procedure of particle removal/reinsertion (Ben-Num and Einav, 2010, McDowell and de Bono, 2013). With this method McDowell and de Bono (2013) replicated qualitatively with DEM analyses experiments of one-dimensional compression by using an Octahedral shear stress and Weibull distribution to determine the particle failure. While this study showed small broken particles contribute to the resulting macroscopic response, including the post-yielding compressibility, their computations tended to be largely inaccurate from a quantitative standpoint, mostly because of the severe approximations resulting from the use of spherical particles.

As most existing DEM approaches over-simplify particle features, hybrid computational framework based on peridynamics have been suggested. Peridynamics is a continuum mesh free method combining to simulate fracture mechanisms (Zhu and Zhao., 2019; Wan et al., 2020). This method simulates the rigid body motion of particles and inter-particle interactions for irregular shape; however, the particle should always have local concave features, and this limits the possibility to describe concave particles. In this context, DEM with Fourier descriptors have been suggested to simulate non-convex particles, but their use has been limited to the simulation of intact particles not undergoing breakage. This indicates that other strategy in DEM is required to describe accurate shape and its variation in crushable granular system.

(a) (b)

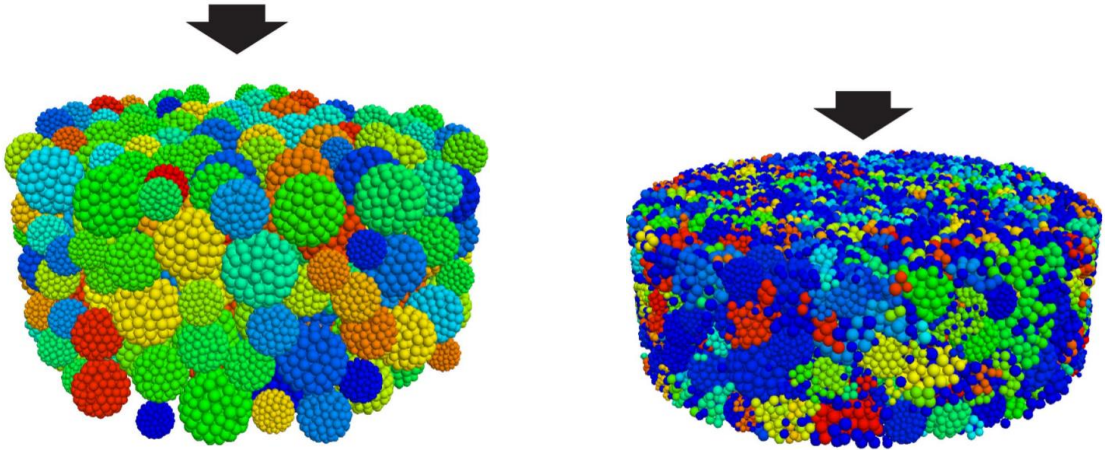

Figure 2.8. (a) Before; and (b) after oedometric compression simulation with DEM (Cil et al., 2019)

2.3.2 LS-DEM

The recent proposition of LS-DEM, originally introduced in Kawamoto et al. (2016) is an advanced DEM that fully captures the shape of every particle with level set functions by generating 3D particle avatars from X-ray tomography images. Level set functions define the particle geometry by using both a discrete level set, φ, equal to the signed distance, d_d, to the surface (Eq. 2.4)

$$\varphi(x) = \pm d_d \tag{2.4}$$

The particle interaction is calculated from the level set values with a set of surface discretized points, p_d, having the discrete level set to 0 (Figure 2.9). To check the contact, the points of leader (i.e., master) at surface (φ_1) and the follower (i.e., slave) from level set points (φ_2) are compared. When any points of the surface $\varphi_2(p_{di})$ has a negative value, it is considered as overlapped. The contact forces and moments are integrated for each time step by explicit scheme. LS-DEM computes the frictional forces by Coulomb friction and linear contact models, although it enables the use of Hertzian contact laws depending on the goals of the analysis.

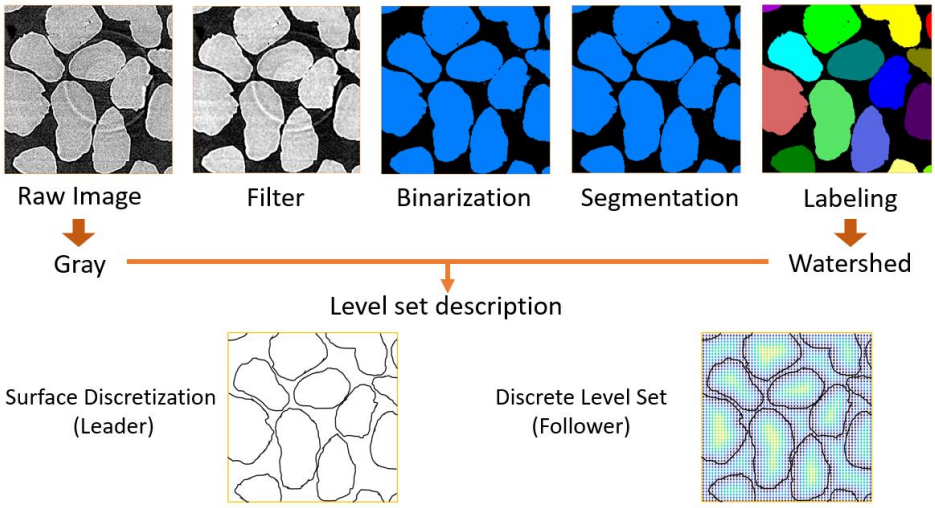

Figure 2.9. Schematics of Post-image processing and level set image preparation

Under unbreakable conditions, LS-DEM has been validated with stress-strain and volume-strain relations observed in triaxial test as shown in Figure 2.10 (Kawamoto et al., 2016). LS-DEM has also been recently augmented to simulate particle breakage by adopting a particle splitting strategy (Harmon et al., 2020). Specifically, the average stress of single discrete level sets is obtained as a maximum principal stress while other strength criteria, such as von Mises and the Tresca failure conditions, can be used. Eq (2.5) shows the calculation of maximum principal stress with volume, V^p, branch vectors, x_c , and the contact forces, F_c. When the average stress exceeds the yielding criterions, particle breakage initiates and the critical stress of the particle is calculated based on Weibull's theory considering particle material and size (Weibull, 1951) (Eq. (2.6)).

$$\bar{\sigma}^p = \frac{1}{V^p}\sum_{c=1}^{N_c} x_c \otimes F_c \tag{2.5}$$

$$P_f(\sigma \geq \sigma^{max}) = 1 - exp\{-\left(\frac{d}{d_0}\right)^3 \left(\frac{\sigma}{\sigma_{c0}}\right)^m\} \tag{2.6}$$

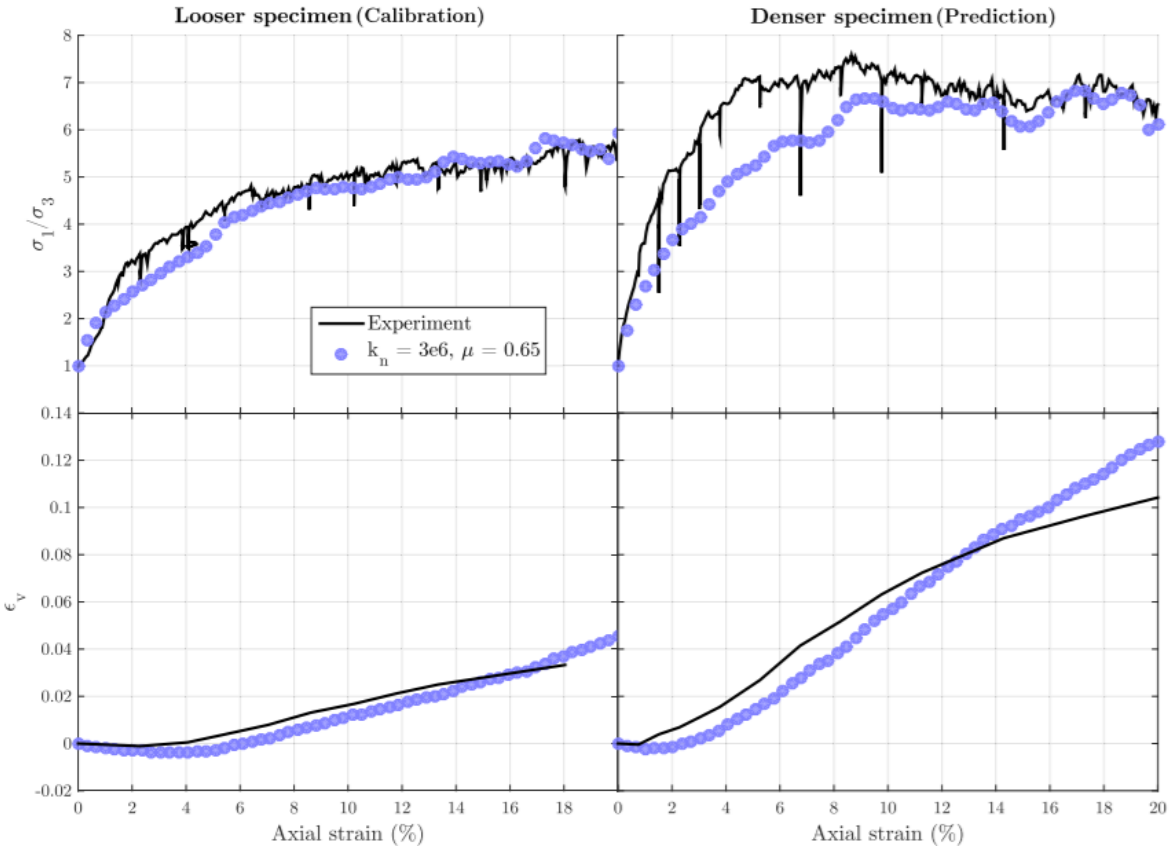

Figure 2.10. LS-DEM simulation results: stress–strain and volume–strain curves for on looser (left) and denser (right) samples (Kawamoto et al., 2016)

Figure 2.11 shows the details of the procedure, according to which the original level set, φ_1 with the splitter, φ_2 generates two new particles φ_3 and φ_4. For simplicity, the split surface is shaped to flat plane, but arbitrary shapes can in principle be used. At breakage, φ_2 is set to the plane passing the three highest contact forces on φ_1 or the plane determined with two contact forces combined with the particle centroid when the degree of particle coordination is two.

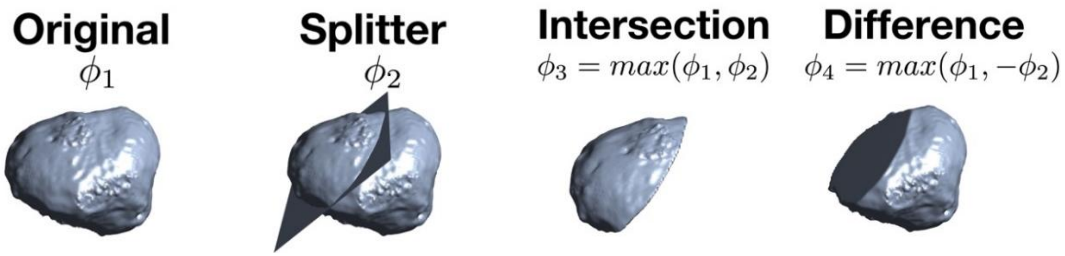

Figure 2.11. Schematic of particle breakage in LS-DEM (Harmon et al., 2022)

Recent work for particle breakage with LS-DEM verified its ability to solve the previously mentioned challenges in modeling morphological changes during breakage (Zhao et al., 2019). The results of LS-DEM reasonably mimic the experimental data of oedometric test with silica sand not only in terms of stress-strain curves, but also particle size distribution at initial and final states in Figure 2.11 (Harmon et al., 2020, Nakata et al., 2001). Therefore, LS-DEM can provide an avenue to quantify information inaccessible from x-ray tomography experiments. In this study, with the benefits of LS-DEM, computational analyses will be conducted to quantify properties (i.e., contact forces) unavailable from image analysis.

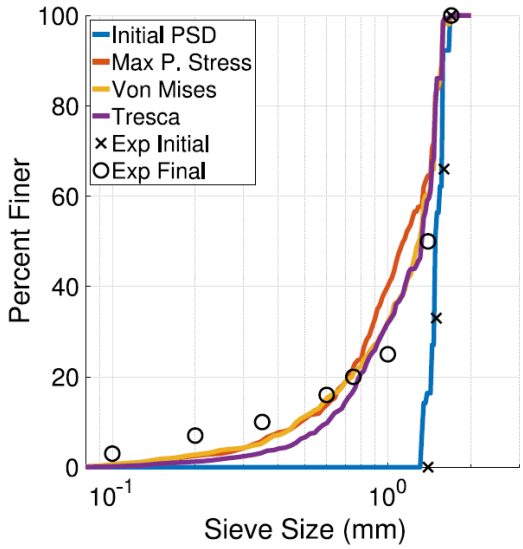

Figure 2.12. Validation of LS-DEM with experimental data at the initial and final particle size distributions (Harmon et al., 2020)

Chapter 3. LABORATORY EQUIPMENT AND METHODOLOGY WITH X-RAY TOMOGRAPHY

3.1 Introduction

The advent of non-destructive testing techniques (e.g., 3D X-ray tomography) in laboratory geomechanics has allowed the direct observation of the particle-scale response of granular systems in 3D. Such use of imaging techniques during an experiment is often referred to as *in-situ testing*. Over the last decades, the developments of in-situ tests have led to a new era of micromechanics in geophysics and geomechanics by quantifying underlying behaviors not accessible until few decades ago. With the benefits of non-destructive methods, this chapter provides the details of testing materials and the description of two types of tests of granular materials in conjunction with 3D X-ray tomography (i.e., oedometric test and diametral test). Specifically, in-situ tests for two types of sample-scale (i.e., single particles and assembly) are conducted by a customized compression apparatus to characterize the sequential breakage of granular materials while the details of 3D X-ray tomography will be discussed in the next chapter.

3.2 Tested Materials

To explore the role of the particle shape on the mechanism of collective breakage in an assembly of granular materials under uniaxial compression, two quartz sands with similar average particle size (with a specific gravity of 2.65) are tested: subrounded Ottawa (US Silica, Inc.) and subangular Q-ROK#2 (Corpuscular, Inc.). The morphological features of each type of sand can be visually inspected through scanning electron microscopy (SEM; Figure 3.1), displaying that Ottawa sand

grains have relatively smooth surfaces compared to the irregular surfaces of QROK. Specifically, the attributes of Ottawa sand are a median diameter of 600 μm, roundness of 0.294 and sphericity of 0.701 and those of Q-ROK#2 are a median diameter of 670 μm, roundness of 0.630 and sphericity of 0.855. In brief, the diameter of sand is measured based on the equivalent volume of the scanned images, the roundness is calculated with the strategy suggested by Zheng and Hryciw (2015) based on the two-dimensional image of the cross-sectional area, and the sphericity is calculated based on the equation suggested by Wadell (1951). Further details about the methods to quantify morphological sand properties will be discussed in Chapter 4.

(a) (b)

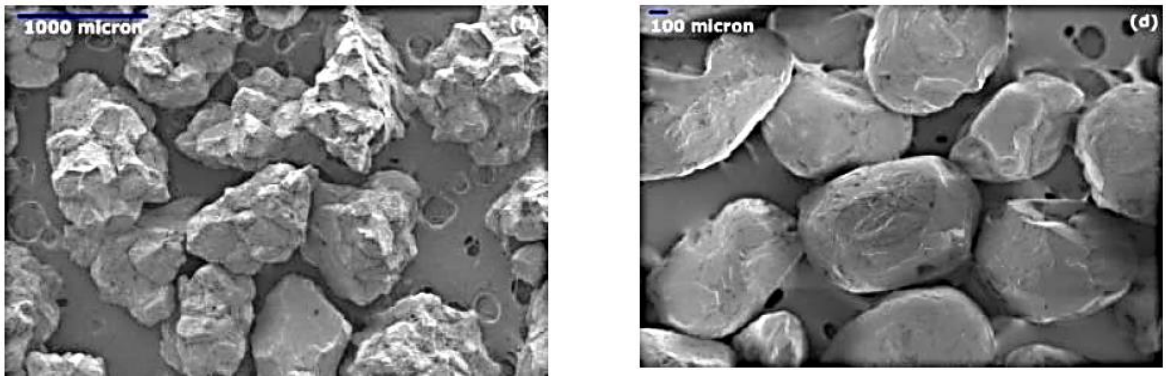

Figure 3.1. SEM images of (a) subangular QROK#2 sands; (b) subround Ottawa sands (Sohn, 2017)

Each sand was sieved between standard ASTM sieves #20 (840 μm) and #40 (420 μm), washed with distilled water, and oven-dried at 110°C for 24 hours. The grains were then placed in cylindrical aluminum tubes with a diameter of 4.1 mm and a height of 5.0 mm through dry pluviation. The samples were densified by repeating tamping and vibration into multiple layers, in accordance with standard procedures (ASTM D4253). This strategy ensures that both subrounded and subangular samples reach their maximum packing density (i.e., eo = 0.60 and eo = 0.80, respectively) in this study. At this point, it is worthy to know that the difference in assembly-scale

properties (e.g., void ratio) is acceptable as such gap is an inevitable result from various morphological features of the two tested sand (Cho et al., 2006).

Figure 3.2 shows the grain size distribution (GSD) curves of two tested sand at initial stage. The GSD is calculated through the image analysis and the percentage mass finer indicates the mass of the tested particle smaller than a given sphere-equivalent diameter. Both GSD shows narrow size variability while QROK#2 is slightly less uniform than Ottawa sand. Again, the slight gap of two prepared samples is an unavoidable feature due to the particle morphology.

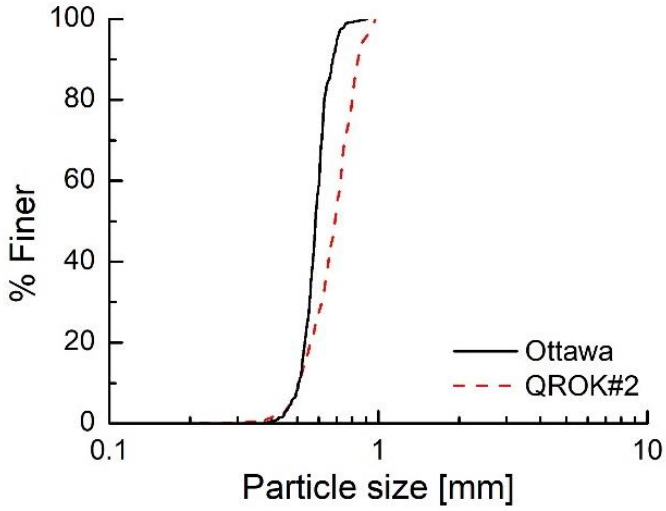

Figure 3.2. Initial grain size distribution curves of Ottawa and QROK#2 sand

To explore particle shape effects on the strength of single grains, diametral tests were conducted. Single particles of Ottawa sand were prepared in the same way abovementioned. 100 single particles are selected manually to reserve a broad range of particle shape. Here it is assumed that the expected erratic factors such as pre-existing internal flaws of the particle, materials constituents, and surface roughness, are constant in the same type of sand. The selected grains therefore will provide the opportunity to distinguish shape effect from the failure response influenced by other factors such as size which will be discussed in Section 6. The median diameter

of the tested particles is 0.707 mm, and this median diameter may be different from the representative median diameter of Ottawa sand itself as the particles are chosen to involve diverse shapes.

3.3 Miniaturized Test Apparatus

To quantify sand characteristics and its mechanics sequentially, in-situ tests have been performed via a customized miniatured compression loading apparatus. This apparatus is designed to target relatively small specimens sized to fit in in-situ test for 3D X-ray microtomography imaging acquisition and manufactured by Romus Inc., Illinois, USA. The miniaturized loading apparatus enables a versatile performance in both the uniaxial compression testing and the local failure modes of single solid of geomaterials and records force-displacement data automatically. Figure 3.3 shows the apparatus consisting of the main testing body connecting to a data recording system sensor, a National Instrument USB-6216, to digitize the measurement. The main testing body is composed of a load cell, a linear variable differential transducer (LVDT), loading pistons made of stainless steel, an acrylic cylindrical frame, and an actuator. The load cell (Model LC302- 250 Omega, Inc.) allows to impose uniaxial compression forces up to 1112 N with a resolution of 0.10 N by contacting the top loading platen. The LVDT (Model LD620-25, Omega Inc.) a 30 mm range of vertical motion. The acrylic cylindrical frame (an inner diameter of 44 mm and a height of 132 mm) supports the main body of the load cell while securing the X-ray penetration to scan the particle sample located between two loading pistons. The actuator (Model CPM-MCVC-2310P-RLN, Teknic Inc.) controls the force-displacement movement with displacement rate (0.01 mm/min – 20 mm/min). This apparatus is controlled and data are acquired through a LABVIEW

software specifically designed for this class of experiments (e.g., strain-controlled uniaxial compression test) as shown in Figure 3.3.

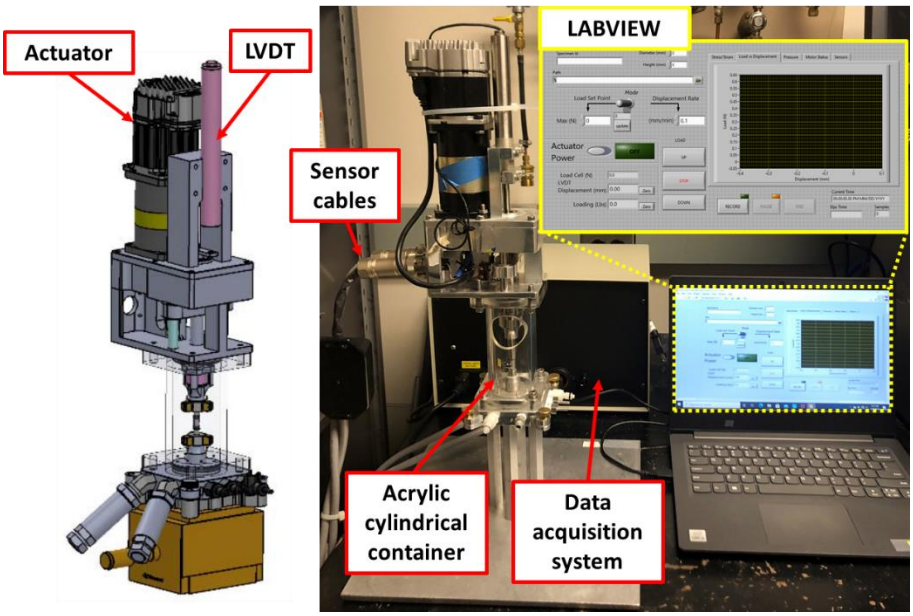

Figure 3.3. The miniature compression test cell and a layout of the LABVIEW software for data acquisition of force and displacement measurements

3.4 Test in conjunction with 3D X-ray Microtomography

Tomography is a non-destructive imaging method reconstructing the internal structure of the object with radiographs resulting from the attenuated X-rays during penetrating inside an object. To examine particle-scale processes, microtomography has been used through in-situ tests. Such in-situ tests in conjunction with X-ray microtomography enable the sequential microscopic response to be captured without interruption of the loading process. The testing cell prepared as described in the previous section is mounted on the 3D X-ray tomography system and the compression tests are conducted while simultaneously acquiring compression loading data (i.e., the force-displacement) and scanned images.

3.4.1 Imaging facility at Argonne National Laboratory, IL USA & 3SR, FRANCE

X-ray microtomography scanning has been conducted at two facilities: GeoSoilEnviroCARS (Sector 13-BMD) of the Advanced Photon Source (APS) in Argonne National Laboratory (ANL), Illinois, USA and Laboratorie 3SR, Grenoble, France. While most in-situ tests have been done at the Argonne National Laboratory, part of diametral compression test is performed at Laboratorie 3SR as a part of research collaboration.

The X-ray facility at ANL provides synchrotron X-ray microtomography (SMT) images. It is worthy to know that SMT acquires high spatial resolution images faster than regular x-rays (Alshibli et al., 2014; Afshar et al., 2018; Hurley et al., 2018). Figure 3.4 displays the loading device setup in the X-ray beamline. SMT offers a high energy X-ray beam ranging from 4.5 to 80keV and the scanning in this study is conducted through pink beam microtomography which transmits a wide range of energy bandwidth and acquires image rapidly while monochromatic beam provides a narrow energy of radiation bandwidth (Rivers, 2016). Pink beams penetrate the prepared specimen positioned between X-ray beam source and a charge coupled device (CCD) imaging detector system. The traveled beam is converted to visible state by a built-in scintillator and a Grasshopper3 CMOS camera acquires this incoming X-ray source with 1.5 mrad grazing incidence angle with 1 mm of Titanium filter. This filter is capable of optimum contrast of the scanned images. In this setup, the bandwidth of pink beam is in 40 keV with an exposure time of 0.008 seconds. It is worthy to know that the solid and pore phases in 3D images can be acquired in the energy range between 25 to 40 keV. The rotation intervals of the sample are 0.1° per projection for 180° about an axis perpendicular to penetrating beam, the total collection of the scan is therefore 1800 radiographs. In this study, the image resolution is 4.28 μm per pixel at the prepared sampled condition (i.e., a diameter of 4.1 mm and height of 5.0 mm). This resolution is

high enough to detect the variation of particle-scale response following the purpose of this study. To convert the raw tomography images to processable data, 3D spatial distribution map is reconstructed by stacking 2D raw tomography slices through an Interactive Data Language (IDL) software.

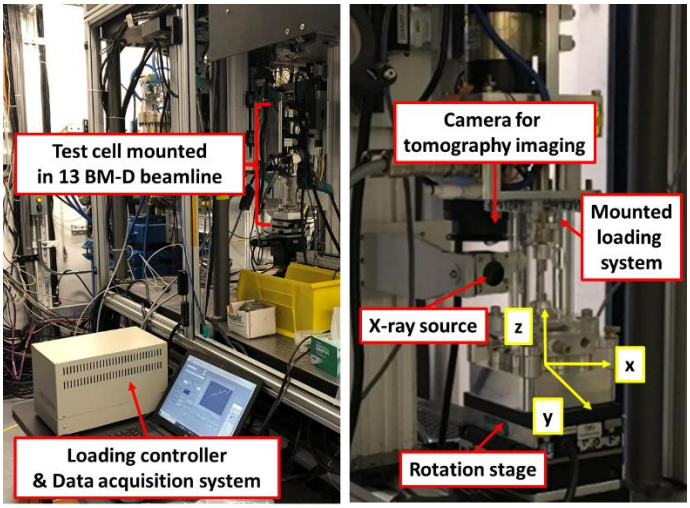

Figure 3.4. Miniaturized loading device mounted at GSECARS 13-BM-D, APS, Argonne National Laboratory

The X-ray tomography device at Laboratoire 3SR is built as a laboratory-scale scanner inside a lead-lined cabin supplied by RX-Solution, Annecy in Figure 3.5. The energy level ranges between 40 to 150 keV with a cone-beam. The radiographs are attenuated by a scintillator (Caesium Iodide, CsI) and detected by an indirect flat-panel Varian PaxScan® 2520V. During illumination, the 1024 images are obtained for 360° for approximately 2 hours per scan. The rotation axis is also perpendicular to axis where the beam travels. 6 radiographs are averaged to get the results of image and the raw tomography are reconstructed by using DigiCT software. The image resolution this study applied is 9 μm per pixel which is reasonable to extract the particle size geometry and more details regarding the images will be discussed in Section 6.

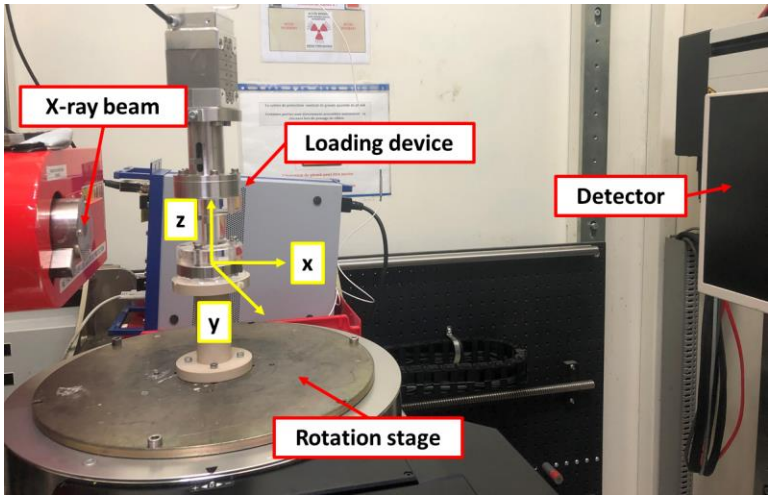

Figure 3.5. Test cell mounted on Laboratoire 3SR x-ray scanner, Grenoble, France

3.4.2 Oedometric compression tests

To quantify the particle shape effects involved in particle breakage mechanisms, in-situ oedometric compression test conducted with the miniatured compression apparatus in 13-BM-D beamline in Argonne National Laboratory as shown in Figure 3.6a.

(a) (b)

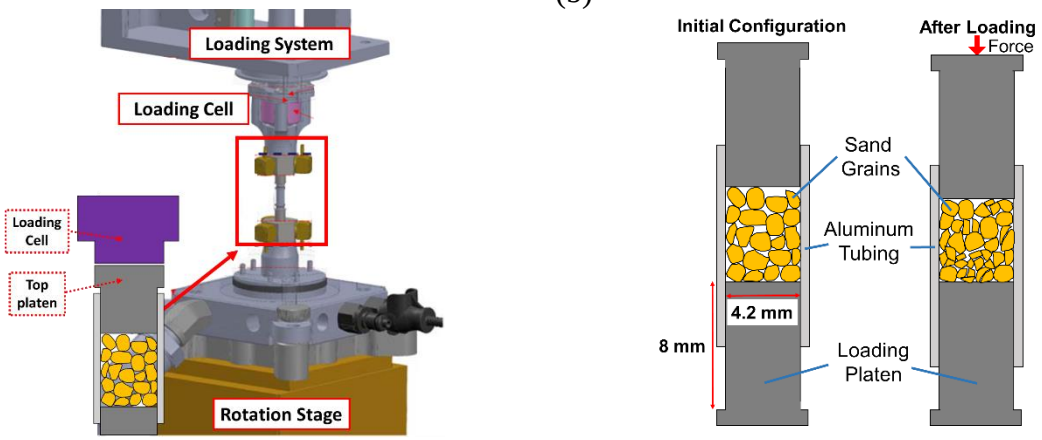

Figure 3.6. (a) General setup of oedometric compression test (b) test cell configuration of oedometric compression test before and after loading

The applied force on the specimen is given from the top platen contacting to a loading cell where the force-displacement is measured together. Figure 3.6b shows that a floating ring is applied on

the sample to minimize the frictional forces on the side of the specimen while the aluminum tubing prevents the radial deformation.

The successive scans are conducted at the selected stress levels based on the yield stress. Specifically, prior to loading, the initial condition of sample is scanned at which the applied stress is 0 MPa and next, the load is applied at a constant displacement rate of 0.05 mm/min. As shown in Figure 3.7a, the stress levels are the normalized stress ratio σ/σ_y = 0.50, 1.00, 1.33, 1.66 and 2.00 for both Q-ROK#2 sand and Ottawa sand. Note that σ is the currently applied stress and σ_y is the yield stress of each material, 15 MPa and 29 MPa, respectively. Those yield stress are determined from the preliminary test as the stress point of the maximum curvature of the compression curve following the conventional soil mechanical approach (Pestana and Whittle, 1995).

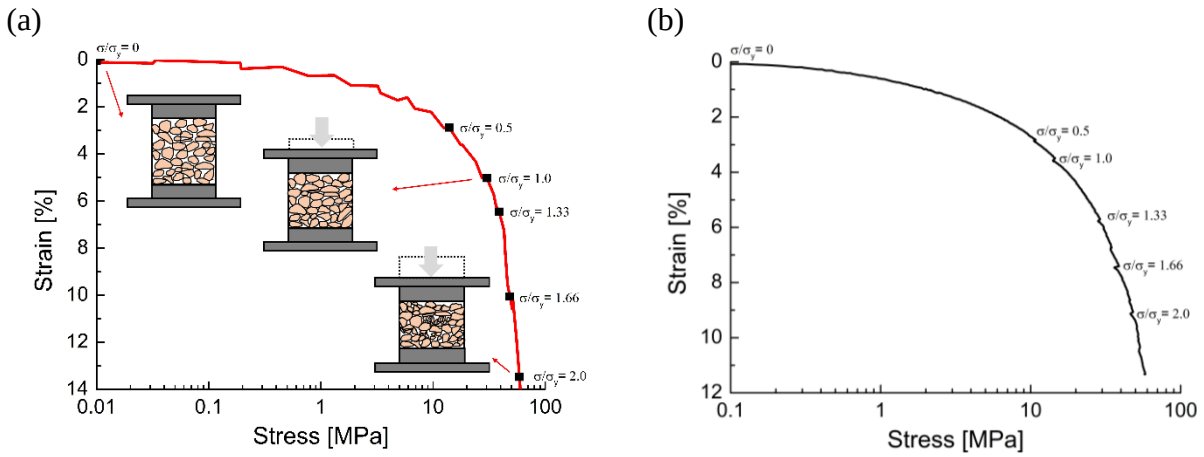

Figure 3.7. (a) SMT scans performed at selected stress states during oedometer tests (b) Stress-strain with stress relaxation at each selected scan point

Such yield stress also represents a point of the reference comminution pressure where the external stress is high enough to trigger grain crushing leading macroscopic compressibility in the assembly. The selected normalized stress ratios as scan points are sufficient to attain the level of stress where pervasive crushing occurs in both assemblies. When the applied load reaches the

designated normalized stress ratio, loading is interrupted and, after 10 minutes of specimen stabilization at fixed loading piston, SMT scans are conducted. Such loading interruption displays stress relaxation as shown in Figure 3.7b with average 4.45 % of the targeting axial stress at each scan.

3.4.3 3D X-ray Scans in conjunction with single particle tests

In this study, the purpose of diametral compression tests is to determine the failure strength of single particles by accounting for both their size and morphology. The tested single particles are scanned prior to the diametral test to their 3D geometrical properties of which the details will be discussed in Section 3.4. Figure 3.8 shows the setup of the diametral compression test where two loading pistons attached to the sand particle without any given force at the initial stage. The initial values of force and displacement are set to zero prior to loading. The bottom piston is fixed while the top piston moves without friction along the axial loading direction and transfers the load when it is attached to the top platen in the same way of Figure 3.6a. The test is conducted with constant displacement rate at 0.05 mm/min (i.e., strain-controlled test condition) and the force-displacement response is recorded until the major drop of force (Figure 3.9).

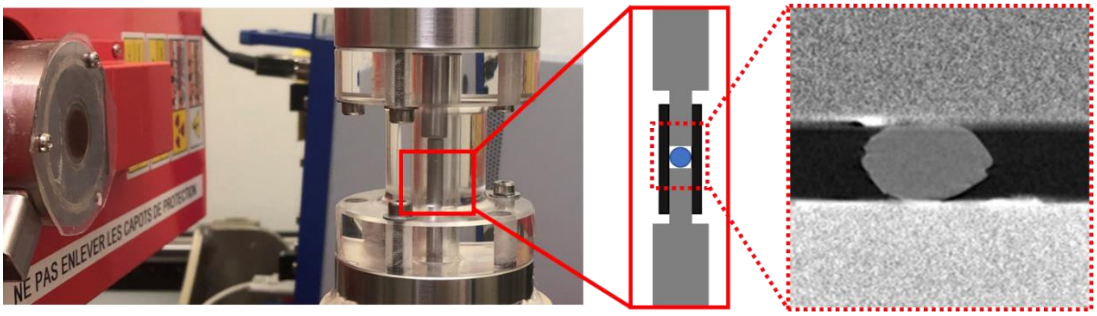

Figure 3.8. Test setup of a diametral compression test with X-ray tomography scan

100 Ottawa sand particles are selected visually to acquire various range of shape within similar particle size and consistent materials color to prevent other expected impact variables such as

materials constituent. As explained previously, due limitations in the access of the testing facilities during the conduction of this research, diametral test for 30 particles are performed in Argonne National Laboratory, USA and the rest of 70 particles are done in Laboratorie 3SR, France. While the diametral loading is consistent in both cases with strain-control (displacement rate of 0.05 mm/min), inevitable differences emerged between the results collected at the two facilities, mostly with reference to differences in the image resolution of the scanned particles. To overcome this inconvenient, adjustments of image resolution were carried out, which will be discussed in the following chapters.

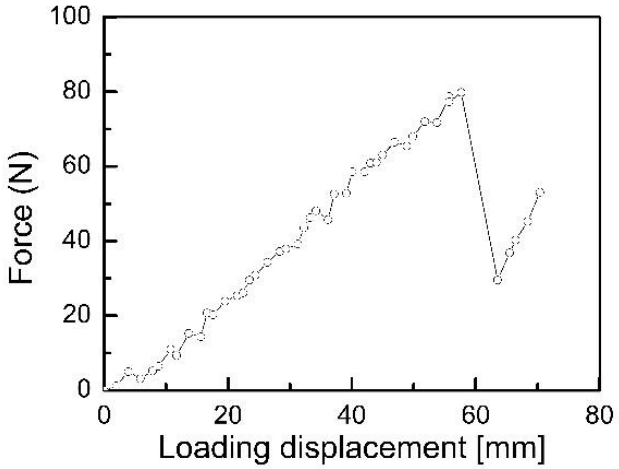

Figure 3.9. Force-displacement curve of single particle under diametral compression test

Chapter 4. COMPUTATIONAL 3D X-RAY TOMOGRAPHY ANALYSIS

4.1 Introduction

One of the primary challenges in granular mechanics is to examine how phenomena occurring at the scale of individual particles affect the bulk macroscale behavior of a granular continuum. From this standpoint, to analyze and quantify particle-scale characteristics and its mechanics, X-ray tomography has been applied to geophysics and geomechanics. As a non-destructive technique, x-ray tomography enables quantification of the sample properties such as grain morphologies and their spatial distribution. Furthermore, this technique allows the acquisition of fast time-lapse images of laboratory test through in-situ test in conjunction with scanning and obtaining the macroscopic test results simultaneously. Those time-lapse images enable to examine the evolution of particle-scale features (e.g., kinematics, grain morphologies, fabric) under continuous variation (e.g., compression, shear banding) (Andò et al., 2012, Alshibli et al., 2013, Zhao et al., 2015, Hurley et al., 2018). In the domain of crushable granular materials, such time-lapse image analysis provides opportunities to characterize the particle breakage in the assembly where each grain undergoes different breakage response (e.g., fracture patterns and failure strength) under given loading to the assembly. This study therefore challenges quantification of the evolution of particle breakage regarding 3D morphological characteristics and effects with the given benefits of 3D X-ray tomography techniques. The following section outlines the general process of 3D X-ray tomography analysis (pre- and post-processing) and proposes a new tracking algorithm specialized in sequential particle breakages and the definition of the quantified particle attributes. By quantifying the undisclosed particle-scale response, the image analysis techniques suggested here will enable us to elucidate granular mechanics with new interpreted data.

4.2 3D X-ray Tomography Imaging

Once tomography scans are performed as described in Chapter 3, the acquired raw images must be pre-processed to reconstruct 3D structures from a series of 2D X-ray projections. At Beamline 13 of the ANL-APS, this step is conducted through the IDL software (Rivers, 2012). Specifically, the dark and white fields of raw radiograph are adjusted to distinguish the solid parts from the void spaces. In addition, mismatches with the original position of the units are unavoidable due to the rotation of the scanned objects during scanning, those 2D slides are rearranged to their center which is estimated based on their grey scale in pre-processing stage. The corrected radiographs are then reconstructed in a three-dimensional image set. Afterwards, through specialized image analysis software (Avizo, FEI Company 2019), the images are post-processed to isolate the individual solid grains for subsequent microstructural quantitative analysis. First, to expedite such post-processing steps, the outer boundary of sample is excluded from the scan window (Figure 4.1a). Next, to minimize the noise while increasing contrast for the solid boundaries, the images are filtered with an anisotropic diffusion algorithm according to the lowest value between the two major peaks appearing in the greyscale histogram as shown in Figure 4.1b (Kim et al., 1987). Such procedure is consistent with similar smoothing strategies previously used for granular materials (Bernard et al., 2011; Cil et al., 2017). The filtered images are binarized to solid and void spaces on the basis of an iterative thresholding procedure based on the minimum value between bimodal grayscale intensity distribution with peaks corresponding to the solid and void phases (Figure 4.1c). Afterwards, a built-in remove-island function is used to remove the local noise remaining from the filtering stage. As this study focuses on the microscopic behavior of sand, the solid matrix needs to be segmented into individual particles. For this purpose, each grain image is separated through a watershed algorithm based on the Chamfer distance for subround grains and a

skeletonization function optimized for irregular units (Figure 4.1d) (FEI Company, 2019). Lastly, the sand particles are labeled individually by setting pixels belonging to each separated solid in 3D to have their own index (Figure 4.1f). Such labelled solids can be quantified to general geometric features at static condition from the built-in function, label analysis. The details of extraction methods will be discussed in Section 4.4.3.

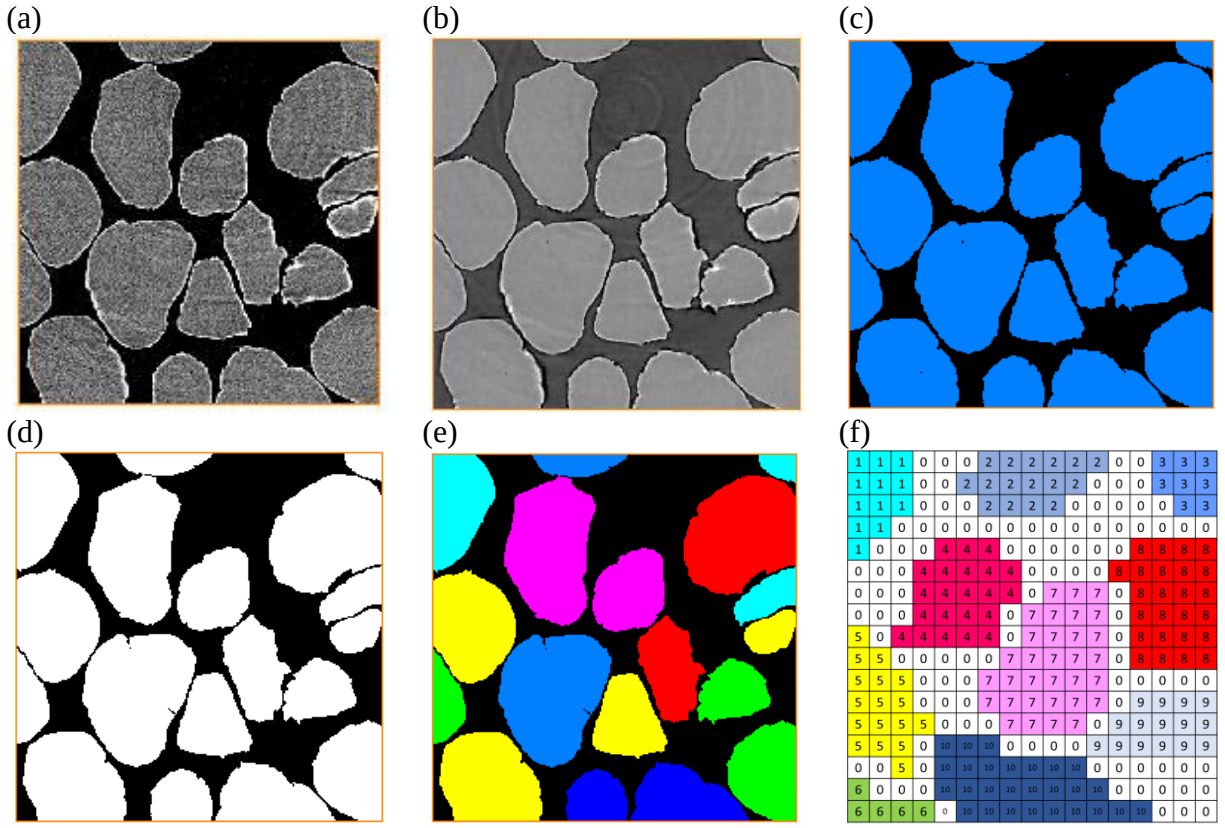

Figure 4.1. Post-processing X-ray microtomography (a) raw image (b) filtering (c) binarization (d) separation (e) labeling (f) an example of digitized labeled image

4.3 A New Tracking Algorithm for Crushable Granular Materials

Under compression, the particles move and rotate simultaneously in 3D and the number of particles from breakage alters under continuous loading. This precludes simple comparison between two sequential image sets even in the processed conditions (Figure 4.2). Therefore, tracking algorithms for crushable granular solids require special procedures to inspect the evolution of the particles, their rearrangement, and the mechanisms leading to the formation of fragments under compressive loading.

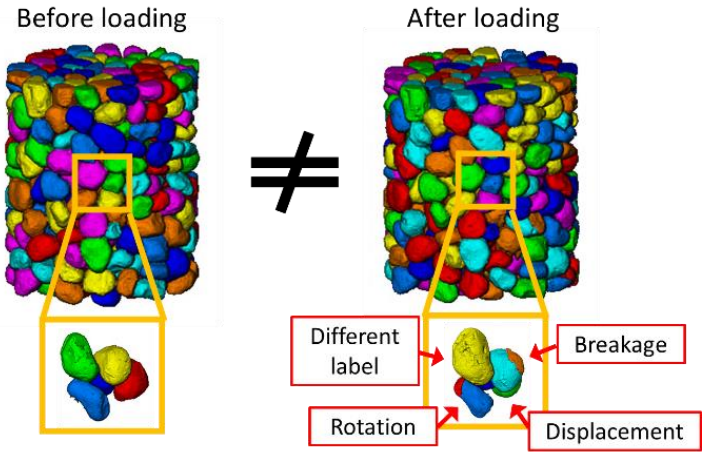

Figure 4.2. Schematic of mismatched labelling between two successive labeled image sets

4.3.1 Methodology of Tracking Algorithm

The algorithm proposed in this work follows the guidelines provided by Andò et al. (2012) for intact grains, recognizing that individual grains can be isolated based on their geometric features (e.g., particle index and geometric properties) measurable from the images. In this study, an augmented algorithm is proposed to enable the tracking of the sequential breakage events for each grain by matching the newly generated fragments with their original grains. This allows not only to track the kinematics of the particles that do not undergo crushing during a single scan (i.e.,

displacement and rotations), but also to record the history of grain breakage events from the start to the completion of an experiment.

The algorithm operates by bridging data from successive scans and it consists of two main steps (Figure 4.3): (a) pairing intact particles; (b) matching crushed fragments (child particles) to the grain from which they originated (parent particles). Part (a) applies three conditions to find an identical particle in the consecutive scans: (i) for the current stage (e.g., timestep 2), it selects all objects in a window of observation determined as a cube of 30 voxels centered at the reference particle position from the previous stage (timestep 1); (ii) it selects the candidates among the objects in timestep 2 satisfying the volumes of the reference object within a ± 3% tolerance; (iii) it verifies that the length ratios (details in '4.4.2 Quantification of particle properties') at the current stage matches those of the reference particle in the previous scan with a ± 10% tolerance. It should be noted that the tolerance values are here chosen by finding a compromise between accuracy of the results and efficiency of computational cost. As a result, these values can be adjusted depending on the testing conditions and objectives of the study. It is possible to get more than one particle satisfying the above criteria. In that case, the expected position of the reference grain from timestep 1 to timestep 2 is calculated based on the average displacement of the neighboring pairs between timestep 1 and timestep 2. Finally, the particle located close to the expected position of the reference grain at timestep 2 is conventionally declared as the paired grain.

In Part (b), the algorithm works exclusively on broken particles. Specifically, the unmatched particles in timestep 2 are automatically considered as fragments with geometrical features that have been determined by a breakage event. Such unmatched particles are referred to as *child particles* and the particles from which they stem are referred to as *parent particles*. Again, the

remained objects after Part (a) (i.e., pairing intact particles) are targeted only to link with their parent particles. The expected position of the parent particle (unmatched with any child particle at this step) can be calculated based on the average displacement of the intact particles. Then the child particle located to the closest to that expected position is assigned to the first child particle to that referred parent particle. Next, the second child particle is determined based on the closest order in distance from the first child particle. This step is repeated until the accumulated volume of child particles satisfying the acceptable tolerance range of their parent volume. As a result, child particles (minimum 2 particles) are matched to their parent particles as shown in Figure 4.3.

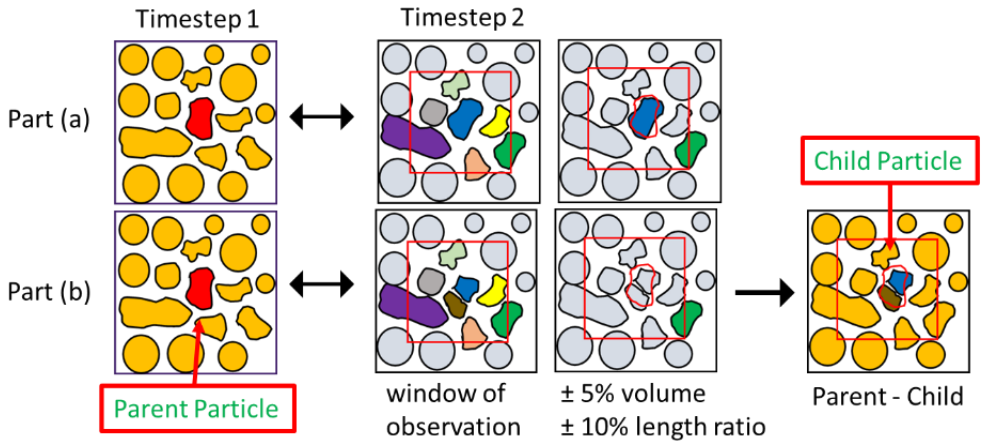

Figure 4.3. Schematic of tracking algorithm, part (a) for intact condition and part (b) for broken condition

4.3.2 Validation of Tracking Algorithm

With the selected examples of image analysis results, the proposed tracking algorithm was verified as illustrated below. Figure 4.4 shows an example relative to a 2D particulate system not susceptible to crushing. The test images consisted of arbitrarily shaped objects moving along a flat surface. The matched objects use identical index and constant color, moreover, the principal axis from the center of mass to the shortest surface and its perpendicular axis are lined to inspect the rotation direction.

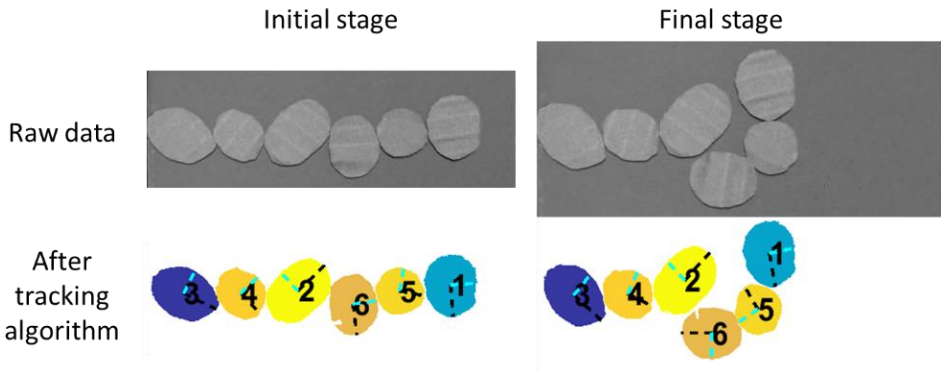

Figure 4.4. An example of performance of tracking algorithm in 2D intact solids

In 3D, independent of the occurrence of breakage events, particle assemblies can have different labeling due to the motions of grains after loading. Figure 4.5 shows the results of pairing obtained from the algorithm with reference to two consecutive image sets. The original labeled image sets display distinct colored grains in Figure 4.5a and after applying the tracking algorithm, two sets attain corresponding matches displaying identical color and index (Figure 4.5b). Such paired images and indices enable a direct comparison to calculate the kinematics of individual grains (e.g., displacement and rotation).

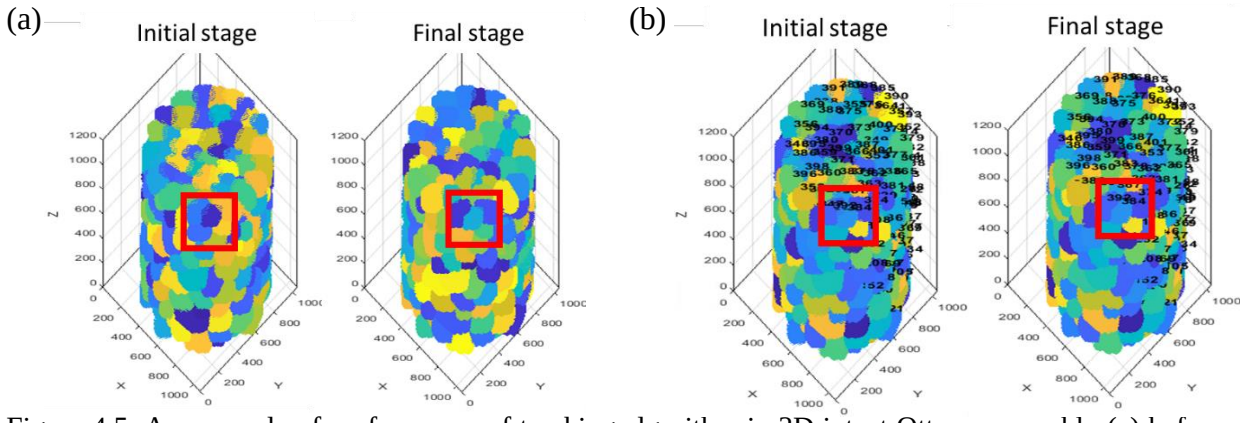

Figure 4.5. An example of performance of tracking algorithm in 3D intact Ottawa assembly (a) before and (b) after tracking algorithm

Besides identifying particles across different scans and tracking their position, the main strength of the enhanced algorithm is the ability to pinpoint the occurrence of breakage events and assess

the mechanisms leading to each individual grain rupture and the outcomes in terms of particle shape evolution. Figure 4.6 shows examples of 2D image analysis of crushable units (animal crackers) chosen to test the ability to quantify relation between particles before a breakage event (parent grains) and their corresponding fragments (child particles) in successive scans. The particle progenies associated with their parent display the index of their parent particle. Note that in Figure 4.6 only, the color is not updated to distinguish the broken condition of solids clearly.

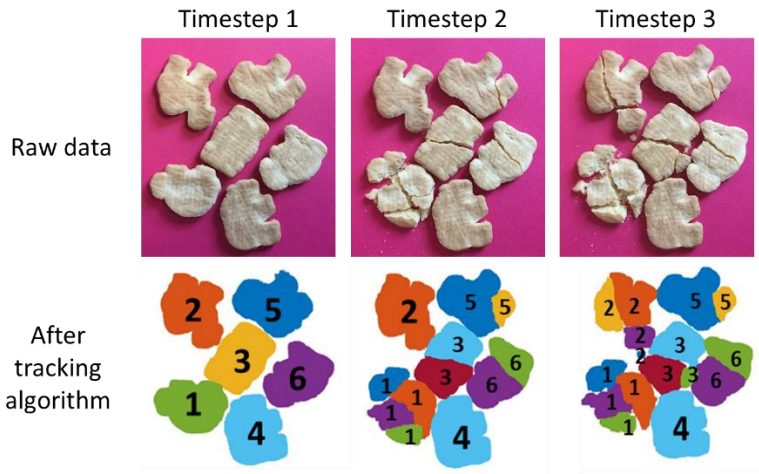

Figure 4.6. An example of performance of tracking algorithm in 2D broken solids

Figure 4.7 depicts digital images of cross-sections of an Ottawa sand specimen under oedometric testing. Given the 3D nature of these scans, some grains appearing in the raw tomography are off the cross section due to out of plane motion of some particles. As a result, Figure 4.7 involves only quasi-planar movements for illustration purposes. In case of application to 3D image, the distinct feature is having two indices on individual grains. First, black labels on each particle indicate the index number of the original particles from the initial condition. Corresponding to the updated main index, the color is also matched to the features of original particles. The second sub-number in red indicates the birth timestep at which the fragments are detected. For example, in the sub image in Figure 4.7 presents ‘3’ (circled in yellow) indicates that fragment was generated at

timestep 3 and survived at timestep 4 without new breakage event while other fragments having ‘4’ for their sub number indicate that they are newly appeared fragments at timestep 4 from particle breakage. These figures document the ability of the processing technique to match child and parent particles. In addition, the algorithm is able to record not only incremental breakage between two successive scans, but also cumulated breakage by accounting for multiple generations of fragments.

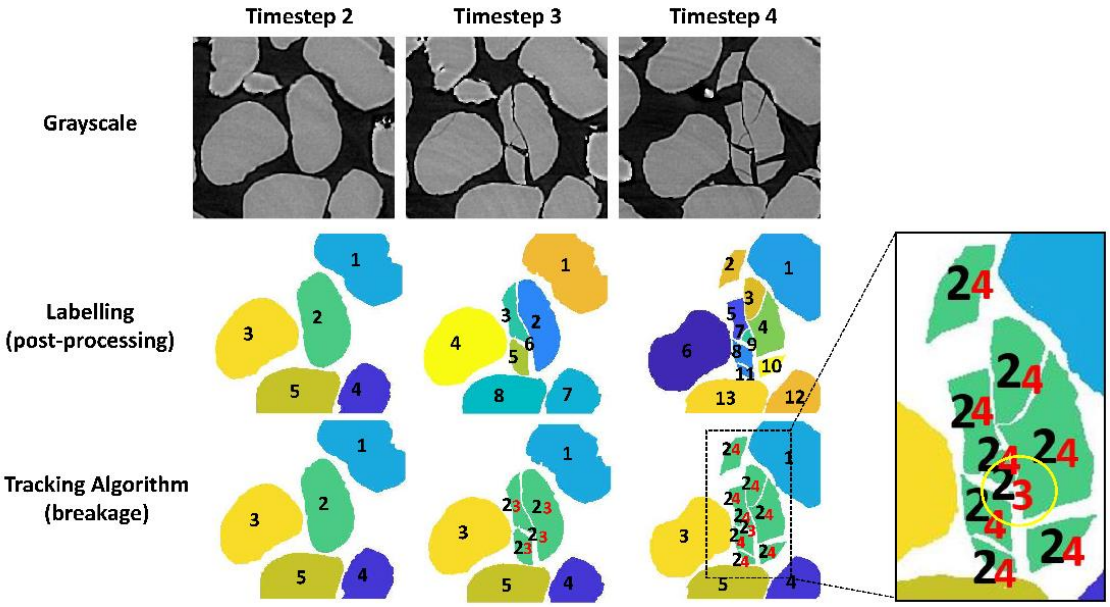

Figure 4.7. An example of breakage tracking in 3D

4.4 Properties for Data Interpretation Variables

The main objective of the tracking algorithm described previously is to quantify the kinematics and breakage events between successive scans. Such image analysis technique can be used to characterize a number of processes involving granular systems. In this thesis, emphasis is given to the interplay between breakage and the evolving morphology of the grains of crushable sands.

4.4.1 Validation of post-processed image analyses

The validation of post-processing in preliminary test is shown in Figure 4.8, reporting the GSD of the initial and final stage of the experiment with Ottawa sand. The initial GSD from image analysis is consistent with that of sieve test, whereas the final GSD of image analysis presents a slight mismatch, with a slight underestimation of finer grain fractions in case of the digital image analysis. It is triggered by the current limit in the image resolution restricting the precise segmentation of the small solids.

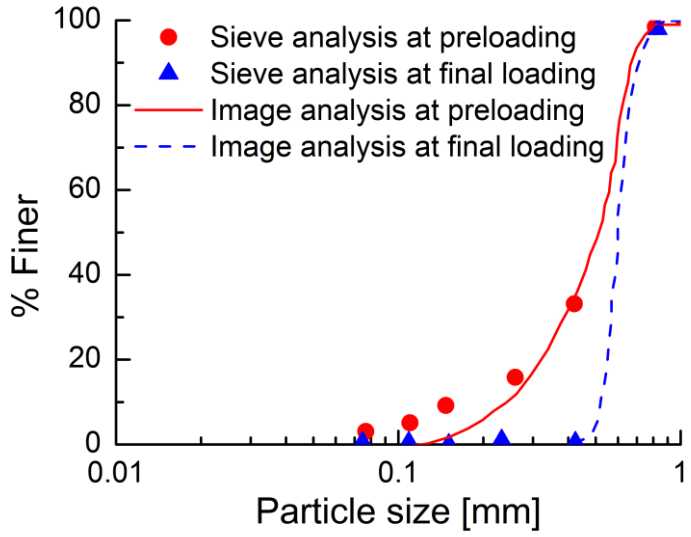

Figure 4.8. Grain size distribution (GSD) curves at preloading (σ_v = 0MPa) and final loading (σ_v = 80MPa) during the oedometric compression tests obtained through sieve analyses (symbol) and tomography image analyses (lines) techniques

Given the common prevalence of image noise on tomography scans and blurred image boundary of finest fragments upon confined comminution from the limit of image resolution, the analysis in this study filters out particles below a thresholding value $10^{-3}mm^3$, in agreement with the conventional size of fine sand (ISO, 2017). Such process guarantees sufficient accuracy for morphological analysis by (i) preventing the biased results from the significant amount of finer

child particles; (ii) ensuring an accurate characterization of the particle morphology through the exclusion of the units most susceptible to inaccuracies due to limitations in image resolution (Hill and Ng, 1996; Zhao et al., 2015). In Figure 4.9a, the frequency ratio of segmented particle volumes shows reliable distribution at the initial state ($\sigma/\sigma_y = 0$) as also verified in Figure 4.8, however at the final stage of the experiment ($\sigma/\sigma_y = 2$) the fines become exceedingly dominant. Figure 4.9b shows that volumetric thresholding impacts heavily the frequency distribution results under the confined comminution condition while initial particle distribution remains consistent with thresholding. This procedure readily presents that the mass reduction induced by filtering out, 1.52 % and 4.31 % of the total particle volume for Ottawa and QROK#2 sand, respectively (Figure 4.10).

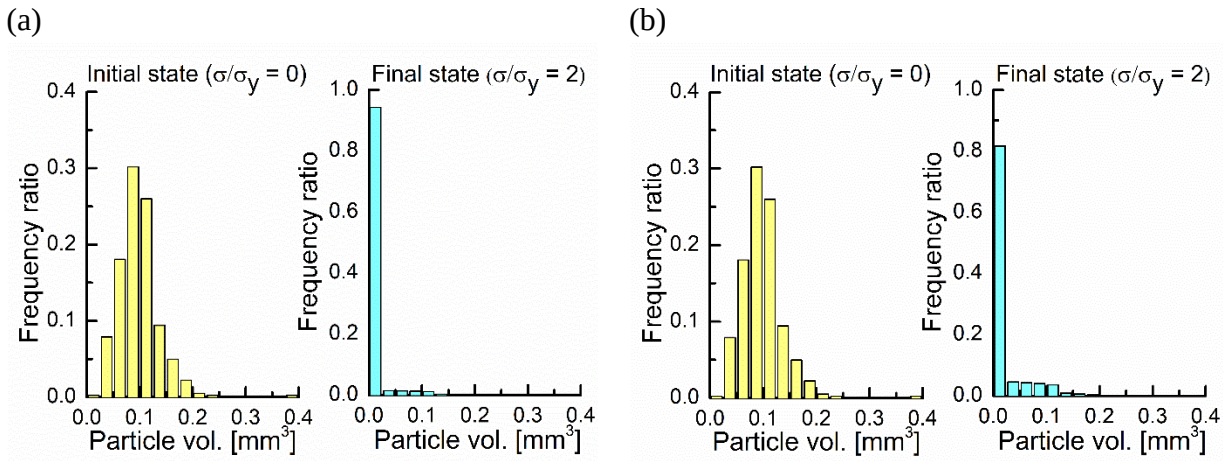

Figure 4.9. Frequency plots of particle volume of Ottawa sand for (a) all particles and (b) sample filtered from very fine broken fragments

Furthermore, mass loss occurred in image analysis increases gradually and such phenomenon appears strongly in irregular shaped solid. It is worthy to note that such mass reduction can be compromised to perform an objective analysis and this strategy is general in conducting image analysis accepted in previous research to retain the reliable analysis of image processing techniques (Karatza 2017).

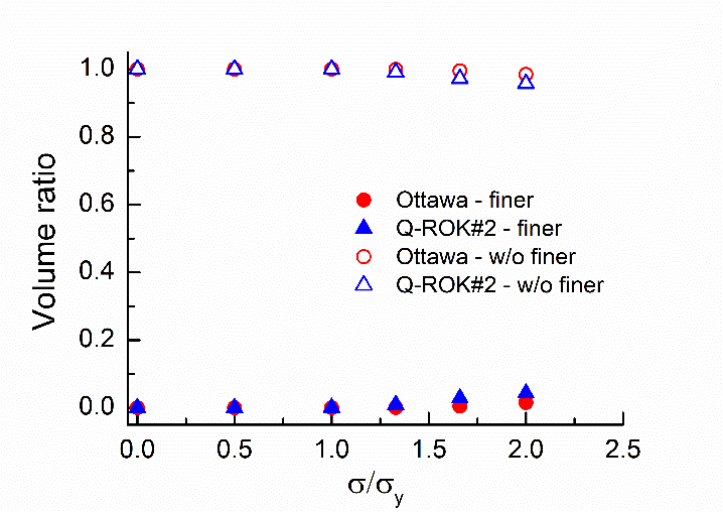

Figure 4.10. Evolution of the volume ratio of particles filtered from fine fragments and fine fragments alone

4.4.2 Quantification of particle properties

This section illustrates the image analysis procedures used to quantify the three-dimensional morphology of individual particles. Such quantification involves the following main attributes: general particle properties (e.g., volume, surface area and central points) and non-dimensional morphological indicators (e.g., roundness, sphericity, aspect ratio, flatness, and elongation index). Specifically, particle volume and surface area are set equal to the number of voxels involving to each labelled solid and its boundary voxels, respectively. In case of the particle position, each center of gravity point is retrieved based on the fixed Cartesian coordinates as a reference. Given the benefits of X-ray tomography to capture the morphological features directly, this study focuses on the evolution of the 3D particle shapes resulting from breakage and explores the corresponding shape variability through nondimensional ratios. Roundness is a local scale shape variable for 2D image expressed as a ratio of the average radius of curvature at the particle corners (marked in green) to the maximum inscribed circle (marked in red) (Figure 4.11) (Wadell., 1935; Zheng, J. & Hryciw, R. D.,2015). This activity was conducted to assure the difference in irregularities of the tested materials.

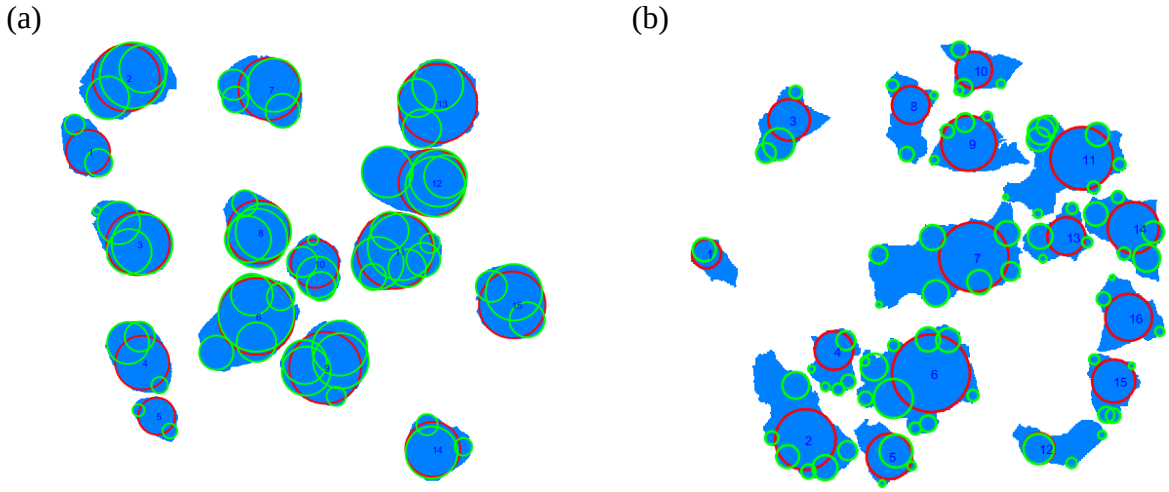

Figure 4.11. An example of roundness measurement on 2D images of (a) Ottawa (b) QROK#2

To facilitate the consideration of particle shape in general by liberating from the image resolution, the shape parameters at global form (details in Chapter 2) were employed in that such parameters are convenient to obtain (Zingg, 1935; Krumbein, 1941; Barrett, 1980). In this context, sphericity, aspect ratio (AR), flatness and elongation are calculated based on 3D measurements to assess the evolution of 3D particle morphology at global form. Sphericity is a measure of the resemblance of an object to a perfect sphere, defined with the ratio between solid volume (V) and surface area (SA) in Eq. (4.1) (Wadell, 1935). Sphericity varies from 0 (e.g., very angular) to 1 (e.g., a perfect sphere).

$$S = \frac{\sqrt[3]{36\pi V^2}}{SA} \tag{4.1}$$

Aspect ratio (AR) is an indicator to describe the elongated shape with a ratio of the minimum length (i.e., shortest length, S) to the maximum length (i.e., longest length, L) of an object in Eq. (4.2). For a spherical particle, AR is equal to 1, while more elongated and flatter particle haves AR values closer to 0. The flatness-elongation ratio, FE, is defined as an inverse number of AR.

$$\text{AR } (or\ FE^{-1}) = \frac{S}{L} \tag{4.2}$$

The elongation and the flatness describing the principal dimensions in 3D at the particle form level are calculated as follows. The elongation index measures the ratio of the intermediate length to the maximum length and the flatness index is a ratio of the shortest to the intermediate length.

$$Elongation = \frac{I}{L} \tag{4.3}$$

$$Flatness = \frac{S}{I} \tag{4.4}$$

Those conventional geometric indices for geoscience can be calculated with the three principal lengths (shortest, *S*, intermediate, *I*, and longest, *L*). Due to the absence of standard fitting methods to quantify these attributes of the particle geometry, this thesis employed different strategies to define shape factors. Therefore, three widely used fitting methods characterizing the major principal dimensions are investigated: minimum volumetric box (MVB), minimum volumetric ellipsoid (MVE), and moment of inertia ellipsoid (MIE) (Figure 4.12). MVB is a method to apply a prismatic fitting box having minimum volume, providing straightforward intuitive metrics like a common caliper measurement (Blott and Pye., 2008, Bagheri et al., 2015). MVE calculates the principal lengths as the semi-principal axis of ellipsoid circumscribing an object and minimizing the fitting volume simultaneously (Zheng, J., & Hryciw., 2017, Yury., 2021). MIE involves an ellipsoid generated from the mass moments of inertia corresponding to the original object (Katagiri et al., 2015, Ikeda, 2000), providing the principal axis lengths of the obtained ellipsoid. These fitting methods based on ellipsoidal approximations of non-spherical particles has the main benefit that they encompass spheres as a particular case (i.e., the standard reference for studies ignoring

shape effects), as well as because ellipsoids are often used in computational models (Ting., 1993, Rothenburg & Bathurst., 1991, Gong & Liu., 2017). By comparing the three selected fitting methods, MVE and MIE measure the values of *L*, *I* and *S* as the lengths of principal perpendicular axes, while MVB equates these principal lengths to the side lengths of a prismatic fitting box (Figure 4.12). Again, since in case of the Feret length, only minimum and maximum lengths can be extracted from the three-dimensional object, but no definition of intermediate length can be obtained, this study has excluded the use of Feret length measurements for particle shape quantification (Walton, 1948).

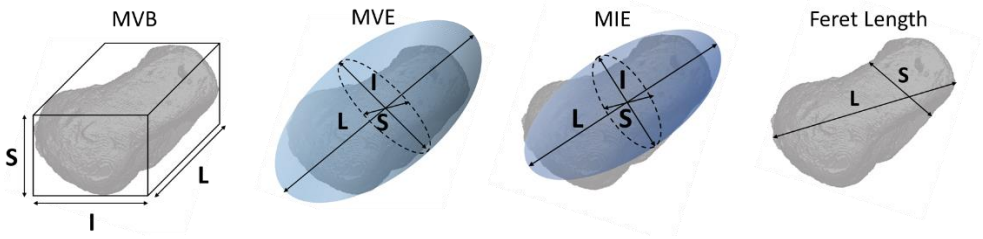

Figure 4.12. 3D illustration of the fitting methods

4.4.3 Classification of particle failure mode

The ability of the proposed algorithm to identify and characterize individual breakage events can be used to classify the different types of particle fracture mechanisms prevailing during confined compression. This study classifies particle breakage events into three modes: chipping, splitting and comminution. *Chipping* is defined as a local damage often involving the edges and corners of a particle due to the concentrating local stress. Observations indicate that such class of particle damage processes tend to result into one large particle with few smaller fragments (Wang and Coop, 2016). By contrast, *splitting* is a fracture mode resulting into energy loss through the formation of a major crack transversing the particle and leading to a small number of fragments of roughly equal size (Unland., 2007). Finally, *comminution* is here defined as a mode involving pervasive disruption of a particle into a large number of small fragments. As there is no established

classification standard for particle failure more, this study differentiates conventionally these three modes by the number and volume of child particles (Figure 4.13).

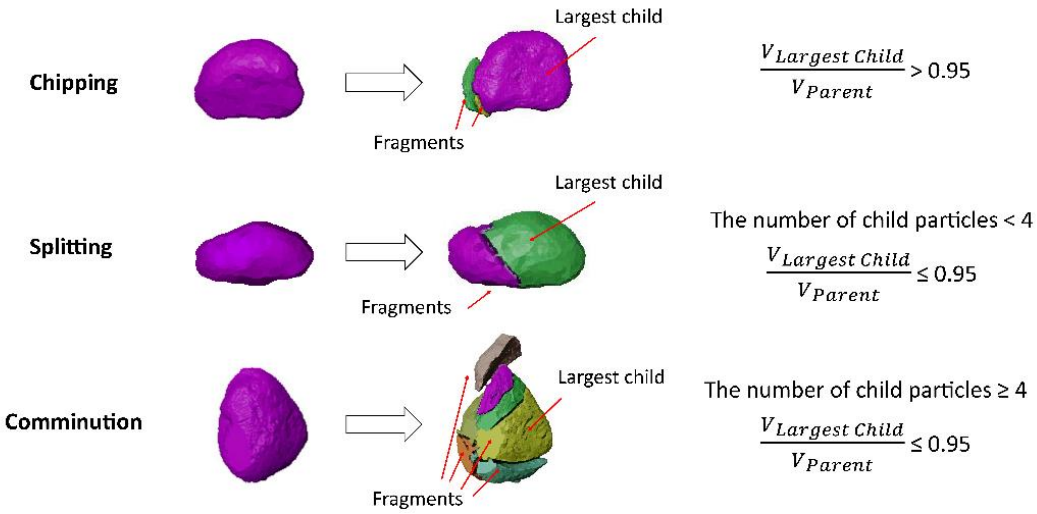

Figure 4.13. Selected mechanisms of particle breakage: chipping, splitting and comminution

As a result, when the volume of largest child particle is above 95 % of the original particle volume, an event is classified as chipping. Conversely, it is classified as a splitting even when no fragment retains a volume above 95 % of the parent particle volume, while satisfying a total number of fragments lower than 4. If such condition is not satisfied (i.e., biggest fragment smaller than 95 % of the parent particle volume), and the rupture generates more than 4 fragments, that event is labeled as comminution.

4.4.4 Classification of particle crushing mechanisms

Successive scans from the beginning to the end of the experiment allow the direct identification of the breakage mechanisms and with the size, number and location of the broken fragments extracted from the tracking algorithm, the evolution of particle breakage is examined into two ways; incremental crushing and cumulative crushing defined here. The incremental crushing indicates the failure events detected between two successive scans and the cumulative crushing tracks the

history of the failure since the original condition, when all particles are intact. Those two counting methods (i.e., incremental and cumulative) enable to comprehend the evolving breakage mechanics towards the ultimate condition of granular system under continuous loading in that previous studies have been limited in defining the crushing mechanics only between the initial and the final byproducts of crushing granular materials. Figure 4.14 shows an example of incremental and cumulated metrics of breakage graphically while the non-dimensional statistical expression will be discussed in Chapter. 5. When the particle breaks from intact condition (between timestep 1 and timestep 2), incremental and accumulated failure value are identical to 2. Under continuous loading (timestep 2 – 3), if only one fragment breaks into 4 pieces while another survives, the incremental failure at timestep 2 – 3 is 4 while cumulated breakage event is 5. At timestep 4, the remained particle broke into two (colored in grey) then incremental failure is 2 as a new incremental failure care and the accumulated failure is updated to 6 for this particle.

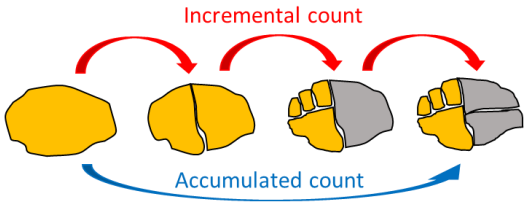

	Timestep1	Timestep2	Timestep3	Timestep4
Incremental count	0	2	4	2 (separately counted)
Accumulated count	0	2	5	6

Figure 4.14. Example of incremental and cumulated count of newly broken fragments

Chapter 5. SHAPE-DEPENDENT COMPRESSION OF CRUSHABLE GRANULAR SOILS

5.1 Introduction

A challenge concerning the mechanics of particulate materials is their response to extreme pressures. At high pressure, the micromechanics of granular soils is controlled by the strength of their particles, as well as by distributed crushing events leading to rearrangement. Particle crushing is therefore a critical factor in the monitoring and interpretation of activities such as pile driving (Yang et al., 2010) and site characterization (Arshad et al., 2014). In geophysical sciences, numerous studies have showed that grain-scale fracture controls the compaction of sediments during the early stages of burial (Antonellini et al., 1994, Chester et al., 2004), thus affecting porosity and permeability of sedimentary basins (Chuhan et al., 2003). Confined comminution is also crucial for the physics of fault gauges, where rocks undergo healing/granulation cycles during which they disintegrate into individual constituents that further fragment during slip (Marone et al., 1995, Tenthorey et al., 2003, Ben-Zion and Sammis, 2003).

In numerous circumstances, the design of earthworks depends on the evolution of the size and shape of fragile coarse aggregates, which controls the long-term performance of rockfill dams (Alonso et al., 2011) and railway ballast (Indraratna et al., 1998). Specifically, crucial properties of sands such as density, stiffness, compressibility and friction angle are all known to be affected by the particle morphology (Zhao & Wang, 2016, Anthony & Marone, 2005, Mair et al., 2002). For example, assemblies with flaky or elongated particles have been found to suffer more severe degradation and larger plastic deformation upon loading compared to sands consisting of round grains (Gur et al., 1967). Similarly, it has been widely reported that knowledge of the fraction of

irregular grains is necessary for the quantification of the small strain shear stiffness of packed assemblies (Altuhafi et al., 2016). Although importance, further progress in this area is limited by the relative scarcity of data documenting the simultaneous changes in the statistics of particle size and shape during breakage.

Recently, such line of inquiry has been strengthened by widespread access to high-resolution X-ray tomography and digital image analysis, which enable precise quantification of the particle features (Todisco et al., 2017). Such advances are especially important in the context of grain breakage, i.e., a process notoriously responsible for major geometric alterations of sand grains (Zhao et al., 2015, Karatza et al., 2018, Sohn et al., 2017). With X-ray image analysis, Zhao et al. (2015) showed that high-resolution imaging allows the identification of fracture initiation in single grains and the quantification of the patterns of fragmentation under diametric compression. The results indicated that the fragments generated by single particles tend to show constant sphericity. More recently, X-ray micro-tomography has facilitated the assessment of multi-particle interactions at the assembly scale. In the domain of grain crushing, Karatza at el. (2019) used digital image correlation to quantify how contact interactions in sands with well-rounded particles influences the initiation of grain failure. Their study revealed that during oedometric compression the onset of different types of breakage depends on the spatial heterogeneity of particle morphology and coordination.

This chapter is motivated by those results supporting the necessity of quantitative analysis for the coevolution of size and shape under continuous breakage. In this context, this study aims to further explore the link between particle geometry, individual grain fracture and distributed breakage. Specifically, the evolution of the particle morphology during comminution will be assessed by

tracking the compression response of packed granular materials and the grain fracture patterns emerging from sequential stages of compression. For this purpose, two quartz sands (subrounded Ottawa sand and subangular Q-ROK#2 sand) with different particle shape have been subjected to oedometric compression within a miniaturized testing setup. Furthermore, the correlation between origins and fragments resulting upon incremental breakage will be explored with the aspects of shape alterations. For this purpose, we will use particle fitting protocols aimed at quantifying the shape of individual particles on the basis of 3D x-ray tomography images and detected by sequential x-ray scans will be analyzed through a tracking algorithm able to follow the breakage history of each individual particle. Through such combined use of shape fitting and digital particle tracking, statistical analyses will be conducted to assess the shape of the grains before and after crushing. As a result, the goal of this study is not only to document the coevolution of particle size and shape associated with the mode of grain failure that can facilitate the assessment of local fracture processes, but also to isolate the mechanisms that contribute the shape characteristics at ultimate breakage.

5.2 Testing Materials and Procedures

To explore the particle breakage under oedometric compression test, two natural silica sands (Q-ROK#2 sand with a median diameter of 600 μm, roundness of 0.294, sphericity of 0.701 and 20/40 US Silica White Ottawa sand with a median diameter of 670 μm, roundness of 0.630, sphericity of 0.855) were prepared as described in '3.2 Testing Materials'. Under the strain control (0.05 mm/min), the vertical loading was applied on the samples having the maximum packing density (i.e., e_o = 0.60 and e_o = 0.80 for subround and subangular sands, respectively). Loading was

interrupted at selected stress levels and SMT scans were conducted after waiting 10 minutes for the stabilization of the axial load while the loading piston was kept in place. The stress levels at which the scans were conducted are given in terms of normalized stress ratios σ/σ_y = 0.50, 1.00, 1.33, 1.66 and 2.00 for both Q-ROK#2 sand and Ottawa sand, where σ is the applied stress and σ_y is the reference comminution pressure for the considered materials (Figure 5.1). The reference yield stress of Q-ROK#2 and Ottawa sands was found to be 15 MPa and 29 MPa, respectively.

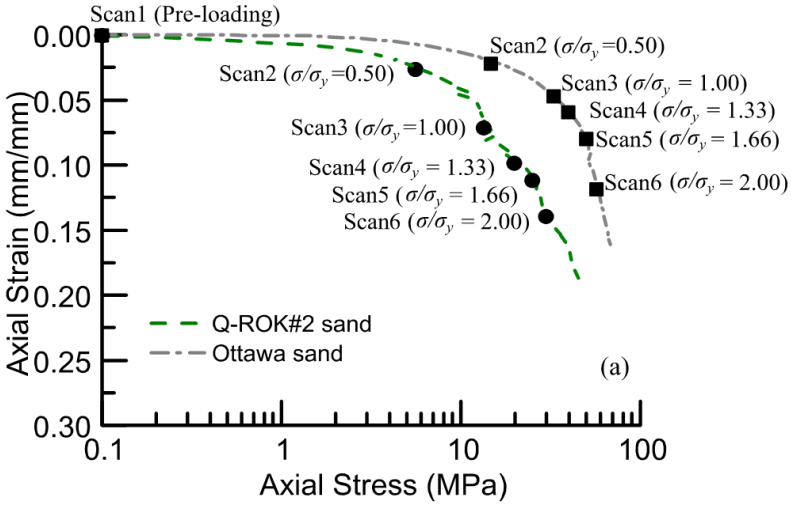

Figure 5.1. SMT scans performed at selected stress states during oedometer tests on Q-ROK#2 and Ottawa sands

5.3 Macroscopic behaviors of Experimental Results

Figure 5.1 shows the oedometric compression curves of Q-ROK#2 and Ottawa sands. As is readily apparent, Ottawa sand has a slightly stiffer elastic response (i.e., less volume change prior to yielding) and higher yield stress than Q-ROK#2 sand. Multiple factors may contribute to this effect, including differences in initial porosity (the Q-ROK #2 sample has higher void ratio than the Ottawa sand sample), and grain morphology (angular shapes can exacerbate stress concentration at the contacts, thus causing higher elastic compliance). Given the difficulty of controlling the packing density in miniaturized samples, quantifying the relative impact of these

factors is beyond the scope of this work. However, it may be noticed that both effects may be directly or indirectly caused by differences in grain shape, in that the packing process of irregular grains is known to generate looser samples once all other factors are kept constant (Cho et al., 2006).

5.4 Quantification of 3D Scanned Images

5.4.1 Shape-dependent Breakage evolution

The sequential scans obtained during experiments are proceeded to quantify the spatiotemporal response as described in '4.2 3D X-ray Tomography Imaging'. Figure 5.2 displays the evolution of the local particle breakage in Q-ROK#2 and Ottawa sands at selected stress levels. Although both sands tend to experience concentrated breakage in the proximity of the loading platen, breakage events can be found throughout the sample volumes in both sands. The images also indicate that Q-ROK#2 particles experienced more severe damage compared to Ottawa sand grains under similar stress conditions. This is in agreement with other studies which showed that specimens consisting of relatively round particles (i.e., Ottawa sand) exhibit comminution at higher pressures compared to their angular counterparts (Hagerty et al., 1993, Nakata et al., 2001, Cavarretta et al., 2017).

Figure 5.3 illustrates the total volume of solids emerging from the analysis of successive scans. The figure shows that the analysis is affected by an inevitable loss of solid volume related with the challenging identification of the finest products of crushing. However, the final computed sand volume obtained from the reduction of image noise and the segmentation of small fragments was found to cause a limited loss of solid mass, equal to 1.30 % and 3.74 % for Ottawa and Q-ROK

#2, respectively. This result is consistent with the performance of image analyses reported in previous studies (Karatza 2017) and validates the reliability of the selected image processing techniques.

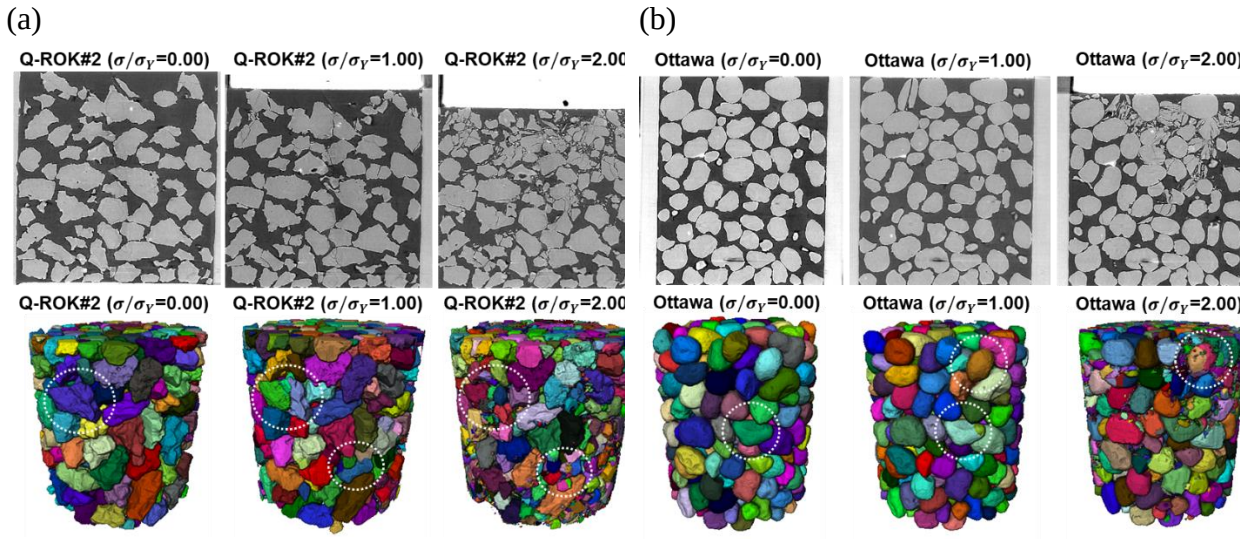

Figure 5.2. Greyscale vertical cross-sections (top row) from 3D SMT images with 3D renderings (bottom row) exhibiting shape dependency of local grain failure (i.e., initially angular particles were broken into multiple fragments at the onset of crushing): (a) Q-ROK#2 sand (b) Ottawa sand

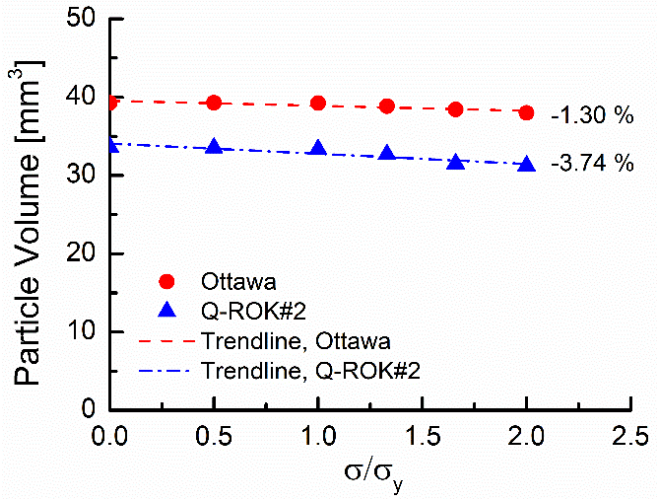

Figure 5.3. Evolution of the total particle (solid) volume in successive SMT scans

The evolution of the particle gradation of the tested sands was obtained via image analysis (Figure 5.4). The distribution was calculated based on the percentage mass finer than a given sphere-equivalent diameter. The figure illustrates the progressive shift of the GSD curves towards finer

gradations upon oedometric compression. Such process takes place by preserving the maximum grain diameter, thus reflecting the presence of cushioning effects and the gradual transition to a breakage process involving primarily smaller, less cushioned grain fractions (McDowell and Bolton, 1998).

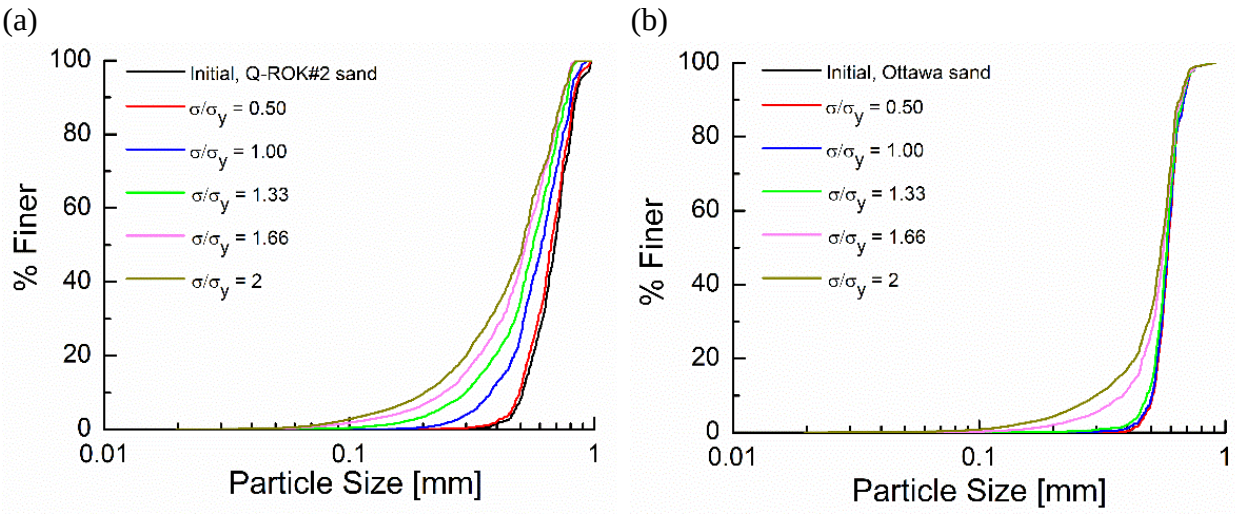

Figure 5.4. Evolution of GSD curves for (a) Q-ROK#2 and (b) Ottawa sands during oedometric compression. The data illustrate the gradual accumulation of finer particles upon loading

The degree of macroscopic comminution was quantified by using the continuum breakage index, *B*, defined in the context of Breakage Mechanics models (Einav, 2007). The breakage variable *B* measures the relative position of the current GSD ($F_{current}$) between the initial (F_o) and ultimate (F_u) GSDs, and it is computed as the ratio of the area comprised between the initial and the current GSD (B_t) and that comprised between the initial and ultimate GSD (B_p). Complete breakage occurs at $B = 1$, whereas $B = 0$ indicates an unbroken material (initial grading). For the purposes of this work, such index has been computed by using a minimum diameter of 1 μm (Kendall, 1978) and a maximum diameter consistent with the initial GSD.

The degree of macroscopic comminution was quantified by using the continuum breakage index, *B*, defined in the context of Breakage Mechanics models (Einav, 2007). The breakage variable *B* measures the relative position of the current GSD (*F*) between the initial (F_o) and ultimate (F_u) GSDs, and it is computed as the ratio of the area comprised between the initial and the current GSD (B_t) and that comprised between the initial and ultimate GSD (B_p). Complete breakage occurs at $B = 1$, whereas $B = 0$ indicates an unbroken material (initial grading). For the purposes of this work, such index has been computed by using a minimum diameter of 1 μm (Kendall, 1978) and a maximum diameter consistent with the initial GSD.

Figure 5.5a shows that the values of breakage, B, for Q-ROK#2 sand were higher than those of Ottawa sand at all stress levels. This result is consistent with Figure 5.5b, which displays a higher percentage of crushed particles in Q-ROK #2 sand. Although both materials exhibited breakage prior to yielding, pre-yielding fragmentation was more prevalent in the subangular sand (e.g., more than 12% of Q-ROK #2 particles were fragmented at $\sigma/\sigma_y = 0.5$, while in Ottawa sand a normalized stress of $\sigma/\sigma_y = 1.33$ was necessary to crush a similar percentage of particles). Despite these differences, continued compression promoted convergence of these metrics to similar values. This was largely due to a noticeably higher rate of grain size distribution evolution in Ottawa sand after the nominal yielding point (i.e., at $\sigma/\sigma_y = 1.00$). Such trend caused similar percentages of fragmented particles at the end of the experiment (i.e., $\sigma/\sigma_y = 2.00$), at which most grains within the two samples were affected by crushing.

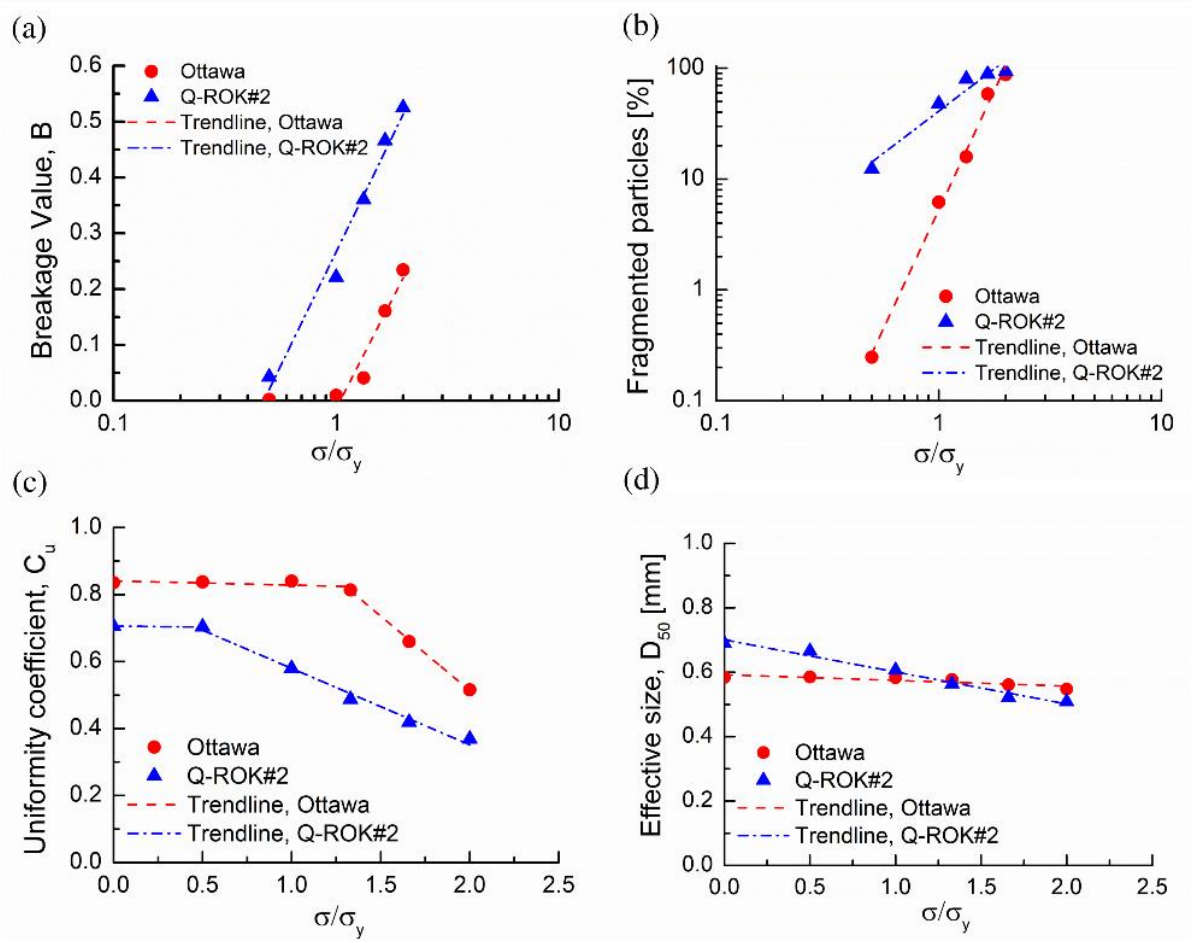

Figure 5.5. Evolution of: (a) breakage index, *B*; (b) percentage of fragmented particles; (c) uniformity coefficient, Cu; and (d) median grain size, D_{50}, for Q-ROK#2 and Ottawa sands

Similar considerations emerge from Figure 5.5c, which illustrates the influence of the initial particle size on the evolution of the coefficient of uniformity, C_u. Specifically, while subangular Q-ROK #2 sand experienced pre-yielding breakage and earlier broadening of the GSD, subrounded Ottawa sand was characterized by relatively constant values of C_u for most of the pre-yielding compression stage, followed by a sharp drop of uniformity in the post-yielding regime. Once again, despite these differences, both sands displayed similar decrease in C_u at the end of the experiment (i.e., ΔC_u=0.33 and 0.32 in Q-ROK#2 and Ottawa sand, respectively). Finally, Figure 5.5d shows that both sands undergo relatively small variations of the median particle diameter,

D_{50}. Such changes are slightly more intense for Q-ROK #2 sand, suggesting that, in a sample which is still relatively uniform (and thus with limited capacity to develop cushioning by benefiting of smaller particles), grain angularity may promote indentation and subsequent crushing in a wider range of particle fractions. By contrast, more rounded particles, such as those of Ottawa sand, better preserve the larger grain fractions by maximizing the effectiveness of cushioning right from the start of the test.

Figure 5.6 plots the evolution of the shape characteristics of the tested sand particles assessed through the collected SMT images, measured as defined in '4.4.2 Quantification of particle properties'. Both sands lose sphericity upon loading due to progressive particle breakage. Ottawa sand particles exhibited noticeable changes in morphology shortly after the yielding point. In particular, its grains displayed sharper changes in morphological characteristics than Q-ROK#2 sand particles at similar macroscopic stress, thus implying that initially subrounded particles undergo more dramatic shape alterations compared to their angular counterparts. Most notably, at the end of the test the value of sphericity for Ottawa sand approaches that measured for Q-ROK#2 sand, thus suggesting that the initial differences in grain shape tend to disappear upon continuous breakage. Furthermore, the FE ratio of both sands increases with loading, thus suggesting that the particles become flatter and more elongated. These results, here based on 3D SMT images, are consistent with earlier findings of Altuhafi and Coop (2011), who documented the alteration of particle shapes via 2D microscopy, and Zhao et al (2015), observing the morphological alteration of a single particle. Such direct visualization of the 3D microstructure therefore indicates that the ultimate morphology of intensely crushed particles in an assembly tends to reach limiting values that do not depend on the shape of the particles prior to loading, thus corroborating the possible

existence of an attractor for the average grain shape of comminuted granular media (Ueda et al., 2013).

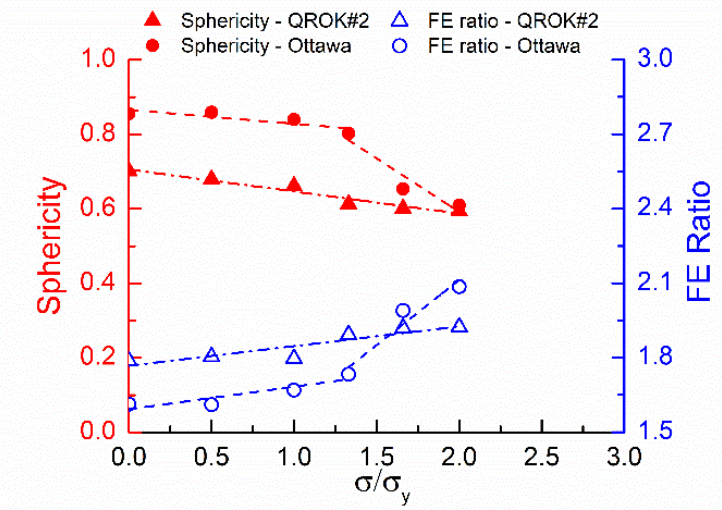

Figure 5.6. Evolution of the average 3D shape parameters (sphericity and flatness–elongation ratio) of the tested sands during oedometric compression in Q-ROK#2 and Ottawa sand

5.4.2 Statistical analysis of particle crushing mechanisms

To quantify the influence of the particle shape on local grain fracture phenomena, two simple fracture indices are computed at each loading step *j* by means of the proposed breakage tracking algorithm, as follows:

$$\bar{\alpha}_f = \left(\sum_{i=1}^{n} N_f^i\right)_j \Big/ N_{pj}\,, \bar{\beta}_f = \left(\sum_{i=1}^{n} N_{nf}^i\right)_{j+1} \Big/ \left(\sum_{i=1}^{n} N_{np}^i\right)_j \tag{5.1}$$

where *i* is the ID number of an individual particle, j is the loading step, N_f^i is the number of fragments (i.e., total number of child particles) at a given loading step *j*, and N_{pj} is the number of original particles identified as crushed (i.e., total number of parent particles) at the selected step *j*. As far as the variables used in the definition of beta, N_{nf}^i is the number of newly generated

fragments at a given loading step *j+1*, N_{np}^{i} is the number of particles (including both original and broken grains) at step *j* which will generate fragments at the subsequent step, *j+1*.

Index $\bar{\alpha}_f$ quantifies the average number of cumulated fragments produced by broken grains. As such, it can be interpreted as a configurational index tracking the fate of initial particles as they undergo comminution throughout the experiment. By contrast, index $\bar{\beta}_f$ uses information available at two successive scans to provide the average number of new fragments generated by each particle at a given loading step. As a result, it estimates the number of new fracture events due to grains that continue to crush upon loading. Although the accuracy of $\bar{\beta}_f$ in reflecting the characteristics of individual fracture events depends on the scan frequency (i.e., it is expected that to some extent successive events between scans may be cumulated), it provides quantitative insight on grain-scale fracture processes, as well as on how the mechanics of grain crushing gradually evolves with the state of the material. Given their definition, $\bar{\alpha}_f$ and $\bar{\beta}_f$ involve a summation across all crushed particles, and thus an averaging.

Hence, to illustrate the statistical variability of these indices across the entire particle populations comprised in the tested sand specimens, Figure 5.7 reports the statistical distribution of the corresponding particle-specific fracture indices $\bar{\alpha}_f$ and $\bar{\beta}_f$. The figure illustrates the evolution of the indices at two normalized stress values, namely $\sigma/\sigma_y = 1.00$ and $\sigma/\sigma_y = 2.00$. It can be noticed that at nominal yielding ($\sigma/\sigma_y = 1.00$) Q-ROK #2 is characterized by a broader distribution of $\bar{\alpha}_f$ values compared to Ottawa sand, and thus by a broader distribution of fracture mechanisms. However, in both sands the crushing events characterized by highest frequency are characterized by the creation of 2 or 3 fragments, thus implying first yielding involves mostly splitting or chipping (Figure 5.7a). At the final state (Figure 5.7b), the frequency plot of the cumulated fracture

index $\bar{\alpha}_f$ becomes considerably broader for both sands, thus indicating that the particles of both materials have experienced by then pervasive comminution, with subangular Q-ROK#2 displaying the highest average number of fragments. This trend was observed in the context of single particle crushing by Zhao et al., 2015, and is here confirmed in the frame of collective compression of packed assemblies. Figures 5.7c and 5.7d illustrate the distribution of the particle-specific incremental fracture index β_f at σ/σ_y = 1.00 and σ/σ_y = 2.00. The figure displays a narrower distribution of particle fracture events compared to the correspondent frequency plot of α_f. This is true both at near-yielding conditions (Figure 42c; where Q-ROK #2 sand particles display a broader range of incremental failure mechanisms than those of Ottawa sand) and at the end of the experiment (Figure 5.7d; where the two distribution becomes much more similar).

Such result suggests that the pervasive comminution phenomena evident from the cumulative index α_f are caused by a continuous succession of simple fracture modes involving a relatively small number of new fragments at each step (i.e., values of $\bar{\beta}_f$ between 2 and 4, consistent with a succession of splitting and chipping mechanisms), rather than by immediate chaotic fragmentation of the particles. Such similarity of the frequency plots of the fracture indices of Q-ROK#2 and Ottawa sand particles confirms once again that at high pressure the effect of the initial particle shape vanishes and consequently the dominant particle failure mechanisms tend to become identical. At this reference, it is worth noting that a complete definition of grain fracture processes cannot be purely geometric but may also need the determination of the contact forces that led to it, the location of fracture initiation and the mode of fracture growth. Although determining these quantities is beyond the scope of this work, knowledge of the sequence and frequency of the grain

breakage mechanisms tracked here on a purely geometric basis can be a starting point for further analyses relying on hybrid computational-experimental methods (Andrade et al., 2011).

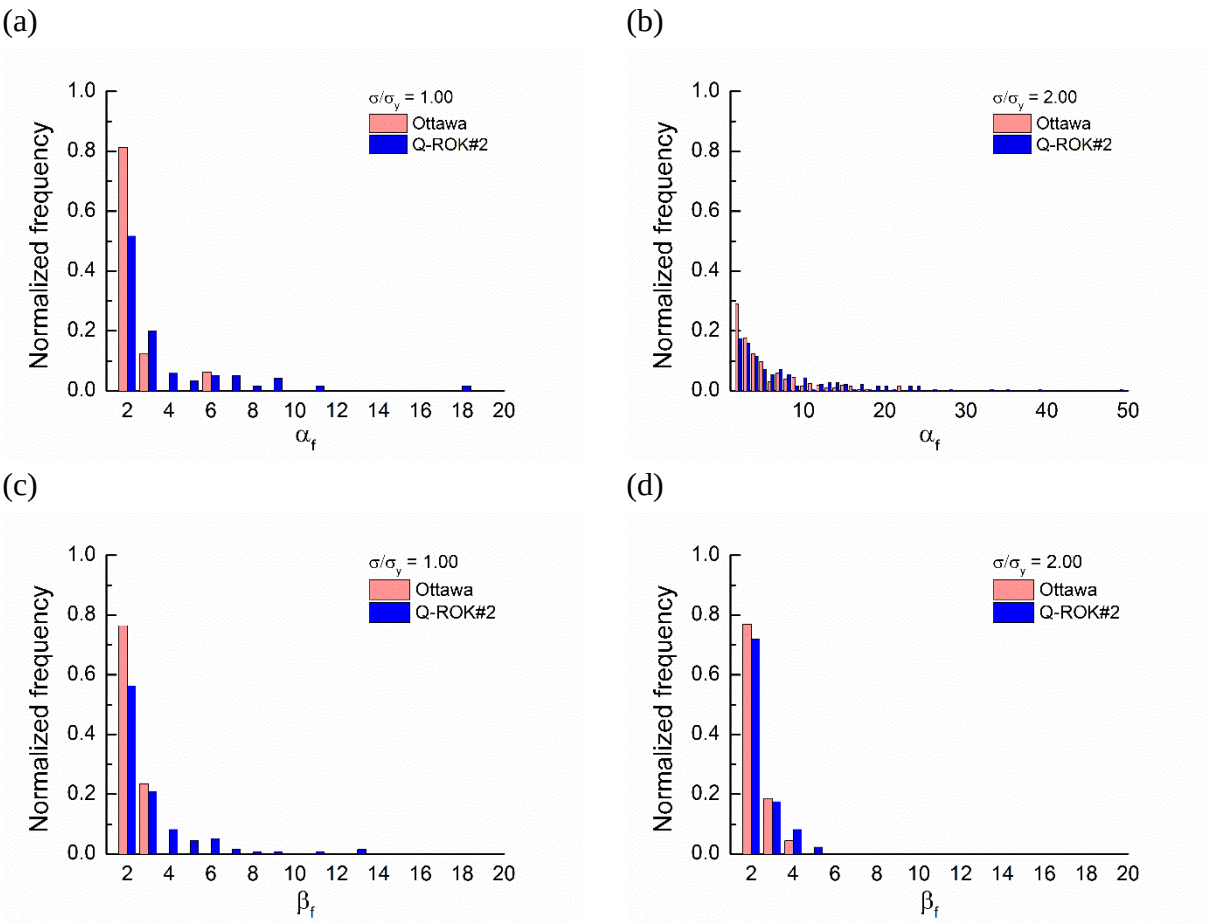

Figure 5.7. Normalized frequency plots of the fracture mode indices for individual particles: α_f at (a) σ/σ_y= 1·00 and (b) σ/σ_y= 2·00, β_f at (c) σ/σ_y= 1·00 and (d) σ/σ_y =2·00. The figure also displays the corresponding averaged values, $\bar{\boldsymbol{\alpha}}_{\boldsymbol{f}}$ and $\bar{\boldsymbol{\beta}}_{\boldsymbol{f}}$, relative to each sand and each stress state

5.4.3 Classification of particle crushing mechanisms

Knowledge of size, number and location of the broken fragments extracted from the tracking algorithm allowed the direct identification of the breakage mechanisms at successive stages of loading. Such step was conducted by using the breakage categories sketched in Figure 4.13 in Chapter 4 as a reference, and it is illustrated in Figure 5.8 for both cumulated (Figure 5.8a, 5.8b) and incremental crushing (Figure 5.8c, 5.8d). Cumulated analyses show a steadily increasing

fraction of heavily comminuted particles among the population of crushed grains (corresponding by the end of the experiment to 49 % and 30% of the total number of particles in Q-ROK#2 and Ottawa sand, respectively). This trend is accompanied by a steady decrease of the contribution of splitting events of previously intact particles (decaying from 61 % to 22 % in Q-ROK#2 sand and from 100 % to 18 % in Ottawa sand). By contrast, the analysis of incremental breakage mechanisms between two successive scans indicates that splitting and chipping processes are the most frequent and account in both sands for a similar fraction of the overall number of particle ruptures (Figure 5.8c, 5.8d). Such results therefore show that, regardless of the initial morphology of the particles, pervasive comminution in sand is mainly a product of successive stages of splitting and chipping.

Nevertheless, the initial morphology was found to play a non-negligible role on the initial stages of compression. For example, a higher proportion of comminution and chipping was found in Q-ROK#2 in the pre-yielding and near-yield regime, while the first breakage mechanisms of Ottawa sand particles were found to be dominated by splitting. These findings are consistent with earlier results by Sohn et al. (2017), who predicted on the basis of a multi-scale continuum breakage theory (Zhang et al., 2016) that subrounded particle assemblies achieve macroscopic yielding through splitting, while subangular particles are more likely to undergo contact failure. However, the results also point out the remarkable richness of post-yielding processes, during which multiple concurrent fracture modes may appear across a compressed granular sample, thus requiring modeling approaches able to account for the feedbacks between shape, coordination, and fracture strength of the constituting particles.

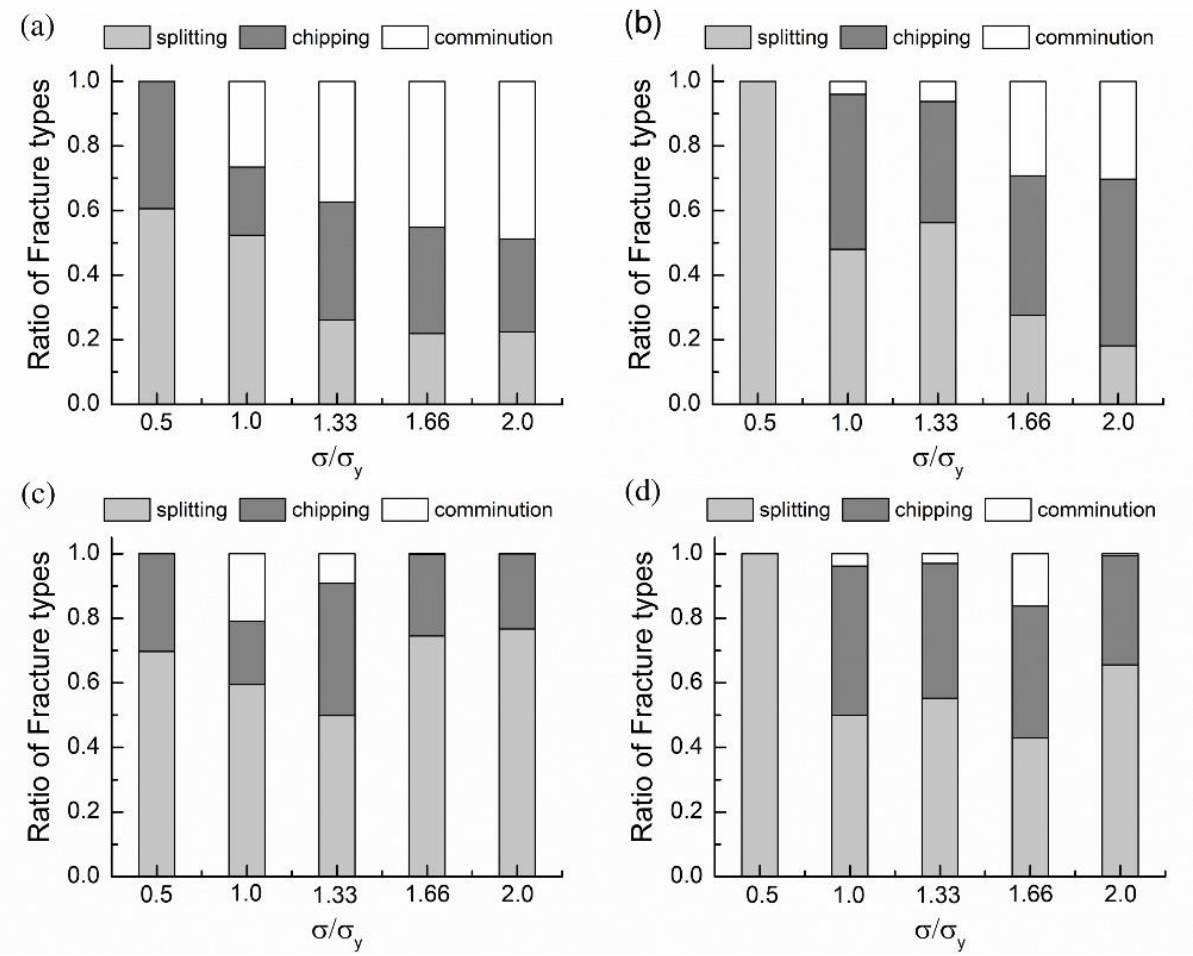

Figure 5.8. Evolution of cumulated fracture mechanisms of (a) Q-ROK#2 and (b) Ottawa sand; incremental fracture mechanisms of (c) Q-ROK#2 and (d) Ottawa sand

The data in Figure 5.9 can be further analyzed by normalizing the frequency of each class of incremental failure event. The goal of this step is to identify the relation between the type of crushing mechanisms and the size of the parent particle from which a given event emerged. Since incremental comminution events are extremely sparse, such analysis is here conducted only for splitting and chipping (Figure 5.9). At σ/σ_y = 1.00 (Figure 5.9a, 5.9c) failure events are rather uniformly distributed across the affected particle sizes for both failure mechanisms. At higher stresses, however (i.e. σ/σ_y = 2.00; Figure 5.9b, 5.9d), incremental splitting concentrates on the finest fractions (i.e., particles with equivalent size smaller than 0.075 mm), which display the

highest values of relative frequency (85 % in Q-ROK#2 and 51 % in Ottawa). This result is consistent with the indications of the frequency plot of β_f (Figure 5.9d), for which the peaks also correspond to a low number of newly generated fragments (i.e., 76 % and 65 % for Q-ROK#2 and Ottawa, respectively). It also indicates the prevalence of cushioning at higher compressive stress, i.e., when the presence of surrounding smaller particles is likely to hinder the rupture of larger grains. Most notably, it is apparent that cushioning affects more intensely splitting rather than chipping events (Figure 5.9d). In fact, while in case of splitting clear frequency peaks are present both for Q-ROK #2 and Ottawa sands (Figure 5.9b), in case of chipping the frequency peaks for events affecting the finest grain fractions are either weaker (Q-ROK #2) or missing (Ottawa).

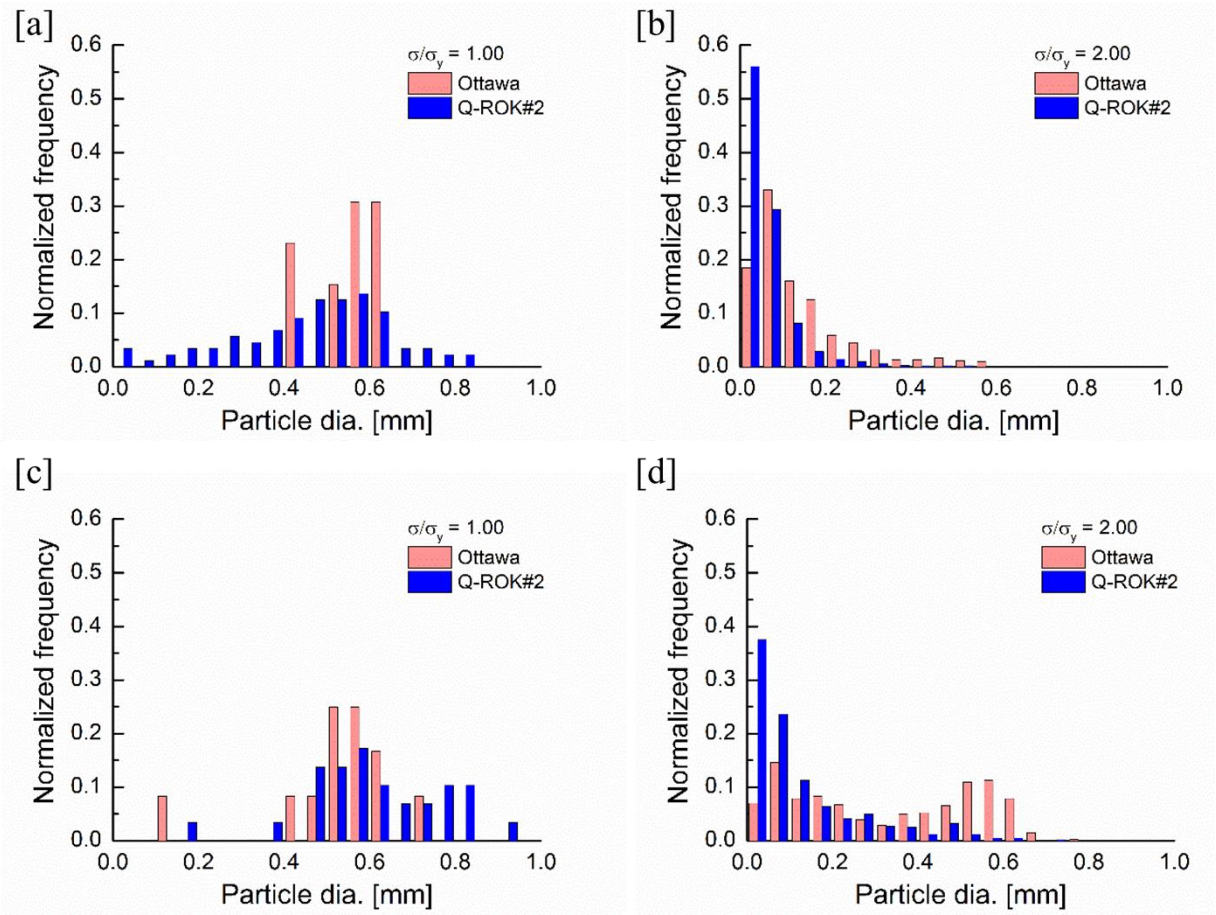

Figure 5.9. Normalised frequency plot of incremental failure mechanisms plotted as a function of the diameter of the parent particle: splitting at (a) σ/σ_y= 1·00 and (b) σ/σ_y = 2·00; chipping at (c) σ/σ_y= 1·00 and (d) σ/σ_y= 2·00

5.4.4 Fitting Method Comparison

As described in '4.4.2 Quantification of particle properties', the three-dimensional form of grains can be characterized by their three principal dimensions (shortest, S, intermediate, I, and longest, L). Three fitting methods are used: minimum volumetric box (MVB), minimum volumetric ellipsoid (MVE) and moment of inertia ellipsoid (MIE) (Figure. 5.10). Figure 5.10 provides a 2D illustration of the features of the three selected fitting methods. Systematic use of these concepts in 3D will be further discussed later. The evolution and distribution of the principal lengths of the particles during confined comminution was examined. To ensure accurate computations, only particles with size above a volume threshold of 10^{-3} mm^3 were considered in the following analyses. This thresholding standard is consistent with the conventional definition of fines prescribed by ISO guidelines (ISO, 2017).

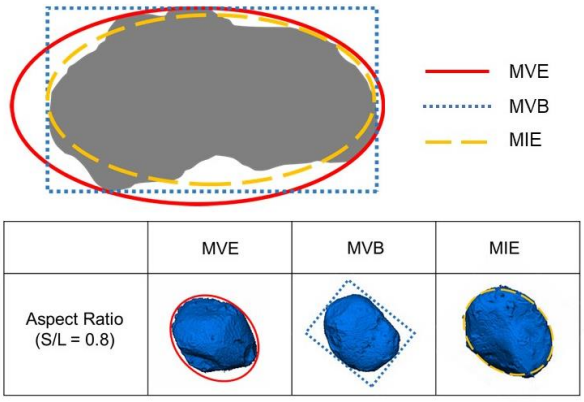

Figure 5.10. 2D schematic of fitting methods used to determine the shape of individual sand grains (MVB = minimum volumetric box, MVE = minimum volumetric ellipsoid, MIE = moment of inertia ellipsoid)

Figure 5.11 shows the evolution of the average principal lengths and equivalent diameter during comminution, quantified with three fitting methods. Each fitting method results in similar trends by involving a noticeable increase in the rate of length reduction at a normalized stress of 1.33 (38.57 MPa). This implies that shape undergoes dramatic alterations at stress levels higher than

(a)

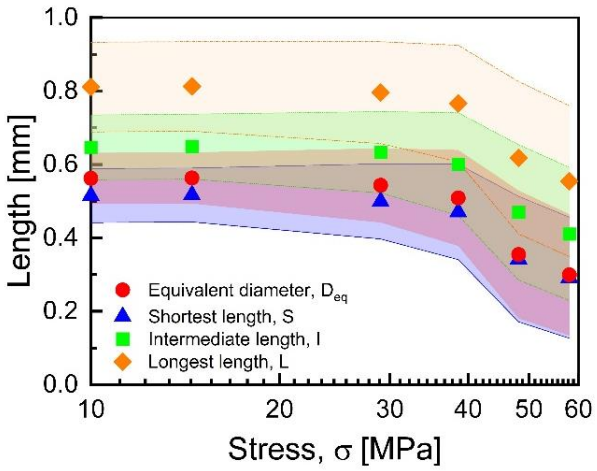

(b)

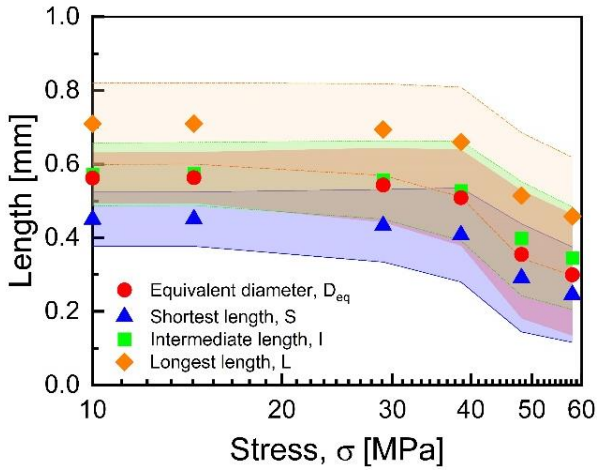

(c)

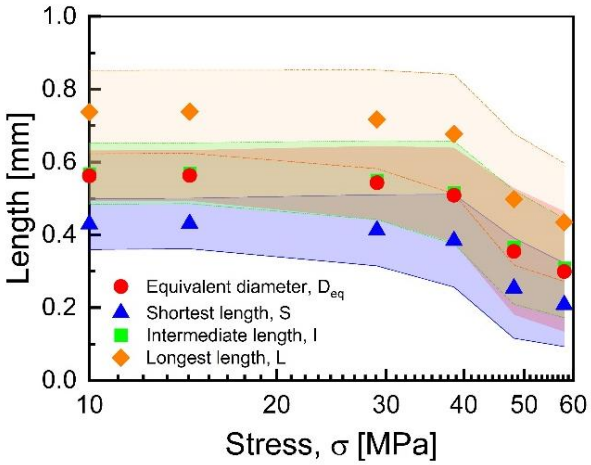

Figure 5.11. Evolution of the average equivalent diameter and principal lengths (*S, I, L*) (a) MVE (b) MVB and (c) MIE. Symbols indicate the average value of the variable of interest. Shaded areas with the same color of a symbol in the plot represent the 90% confidence interval for the variable of interest.

the conventional yielding point. In other words, the standard macroscopic criteria for defining yielding are in general not predictive of the most intense stage of particle shape alteration. However, the relation between the principal lengths and the average equivalent diameter differed between fitting methods. Specifically, while the shortest length, S, resulting from MVE fitting provided a close approximation of D_{eq}, for both MVB and MIE fitting the intermediate length, *I*, was found to be closer to the computed, evolving, values of D_{eq}. Such results are consistent with prior results by (Ganju et al., 2021), who suggested that the shortest length correlates with the grain diameter achieved from ellipsoid fitting, as well as by (Fonseca et al., 2012), who showed that the sieve size widely used in standard soil classification can be replaced by the intermediate length derived from the calculation of the principal axis length (i.e., a method very close to box fitting procedures based on Euclidean distance determined on a Cartesian coordinate system).

Figure 5.12a plots the initial principal length distribution of the entire particle population prior to loading. Even though the shortest length exhibits a narrower distribution compared to longest and intermediate lengths, all three principal lengths are characterized by symmetric distributions. In terms of evolution, all the principal lengths displayed similar trends. Hence, for the sake of brevity, hereafter only measurements pertaining the shortest length will be discussed in detail, with the relative conclusions being applicable also to longest and intermediate dimensions. Upon comminution, the evolving distribution of the shortest length exhibits growing skewness towards small values (Figure 5.12b). Up to the timestep 4 at normalized stress 1.33, the prevalence of fine particles increases gradually and eventually becomes pervasive after the transition point, observed in Figure 5.11. Increase in the frequency of fine particles is accompanied by a corresponding decrease in the frequency of the largest values of the population (which are initially dominant at the start of the process). This leads to the emergence of bimodality, with a transition between the

(a)

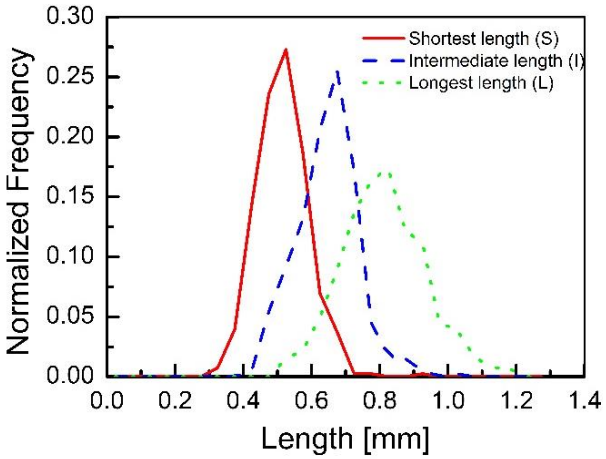

(b)

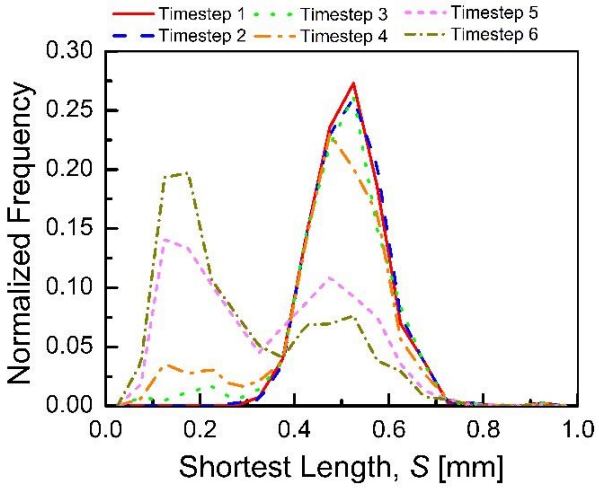

(c)

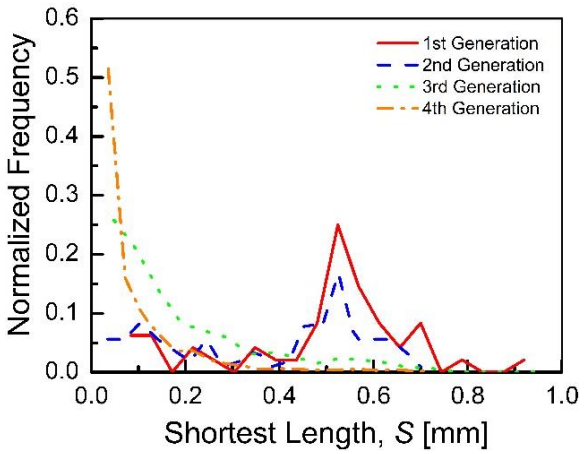

Figure 5.12. Evolution of length distribution computed based on the MVE fitting procedure expressed as normalized frequency of (a) the initial principal lengths (b) the shortest length for entire scan sets and (c) the shortest length according to fragment-generation

two relative peaks of the normalized frequency between 0.15 mm and 0.5 mm. Limitations in the allowable axial stress do not allow to further explore if such bimodal trends persist upon further comminution, which would have required application of higher compressive stress and a corresponding increase of the image resolution able to resolve a larger fraction of crushed particles.

Figure 5.12c displays the varying distribution of the shortest length based on the breakage history of the particles within the assembly. For this purpose, the breakage history is here conveyed by introducing the notion of generation. Such term is used to indicate the order of discrete grain fracture events that lead to the emergence of an individual fragment. Specifically, first-generation fragments result from the breakage of a particle that until that moment had suffered no fracture (i.e., it was intact until that event). First-generation fragments experiencing further breakage may then produce new fragments, which being a product of two successive events will be assigned to the second generation. By generalizing this logic, fragments emerging from particles which suffered N distinct breakage events will be assigned to the Nth generation. The result in Figure 5.12c shows that the largest values of S characterizing the initial particle population are preserved only up to the second generation of crushing history, after which they are no longer characterized by noticeable statistical representations in fragment populations belonging to later generations. This trend explains the progressive shift of the particle size distribution towards finer values in Figure 5.4b and suggests that the emergence of bimodality in Figure 5.12b was primarily triggered by the accumulation of breakage events.

All nondimensional ratios between principal lengths vary from 0 (i.e., distorted) to 1 (e.g., spheroidal). In this study, it is explored whether the selected fitting method influences the determination of these indices at the initial stage (normalized stress = 0; Figure 5.13). Interestingly,

MVE and MVB which involve the largest differences in terms of absolute values of principal lengths (i.e., 0.811 mm and 0.710 mm for the longest length, 0.515 mm and 0.450 mm for the shortest length, respectively) provide nearly identical non-dimensional indices. Specifically, for these fitting methods the ARs are 0.644, while the computed FI and EI display differences as low as 0.860 % and 1.294 %, respectively. By contrast, the MIE fitting method, whose principal lengths are close to those obtained via MVB (Figure 5.11b, 5.11c), results in a lower AR, 0.583. Despite such differences, the variations obtained in terms of nondimensional ratios tend to be in all cases smaller than those resulting in terms of principal lengths (e.g., fixing MVE as a reference, MVB and MIE involved an average mismatch of 0.143 % and 6.513 % in terms of shape indices, respectively, in both cases much smaller than the corresponding average mismatch in terms of principle length, which corresponded to 12.206 % for MVB and 12.611 % for MIB). These results suggest that use of nondimensional shape index represents the most robust approach to minimize the impact of the fitting method in the assessment of initial and evolving particle shape.

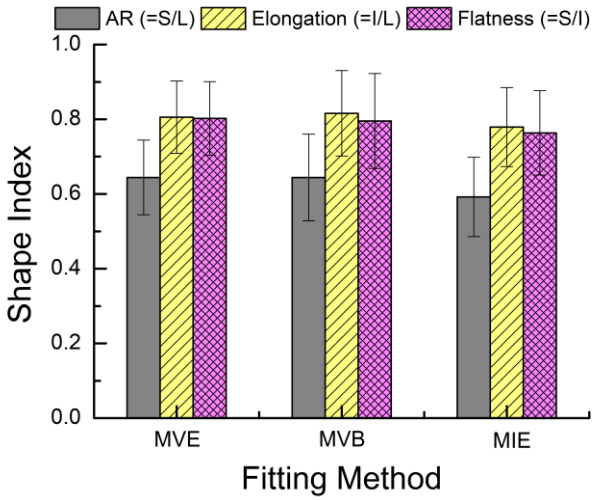

Figure 5.13. Average shape indices (AR, Elongation, Flatness) provided by different fitting methods

5.4.5. Evolution of the particle morphology

Figure 5.14 exhibits the evolution of the AR distribution in terms of mass percentage of particles with AR lower than a given set value, varying from 0 % (most flat) to 100 % (most spherical). The initial AR is distributed from 0.348 to 0.917. During breakage, this range expended by covering the interval from 0.120 to 0.925. Compared to the evolving particle gradation in Figure 5.4b, the evolution trends of AR tend to involve more broadly the entire range of AR values, without showing obvious concentration in particular ranges of particle shape. Despite the particle size bimodality shown in Figure 5.12b, the shape distribution does not display evidence of bimodal shape populations. This result suggests that the new fragments emerging from successive breakage events do not generate shape characteristics radically different from those of the initial set of particles, but rather expand the initial range of existing shape through moderate changes in the shape indices of the new particles within the population.

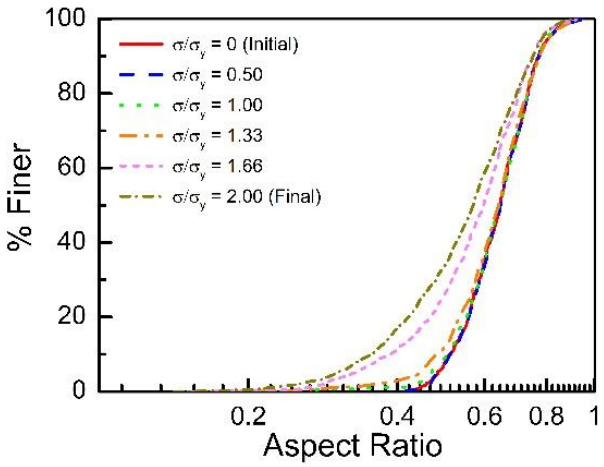

Figure 5.14. Evolution of aspect ratio during oedometer test

The average shape indices have been displayed in the Zingg diagram (Figure 5.15), one of the most widely used graphical formats for 3D shape analysis. The Zingg diagram classifies the

particle shape into four categories based on elongation and flatness: spheroid, disk, blade, and rod (Figure 5.15) (Zingg, 1935). FI and EI are interpreted as x-axis and y-axis for entire scans and the aspect ratio is expressed as a line on the plot only for initial and final timestep. The results are consistent with the analysis in Fig. 6 in that MVE and MVB again show their quantitative similarity regardless increasing fragments and the gap between MIE and MVE at final stage decreases in comparison with the initial difference (Figure 5.15).

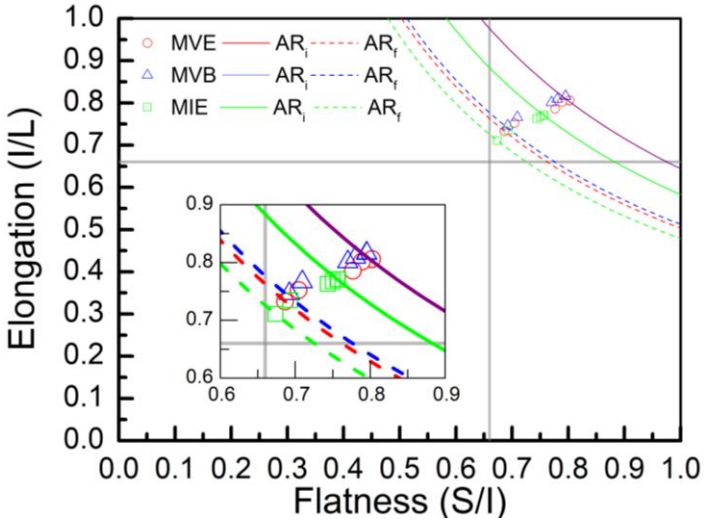

Figure 5.15. Evolution of shape parameters on Zingg diagram

5.4.6 Shape heritability

To explain the microscopic origin of the observed statistical trends of particle shape evolution, this section examines the correlation between shape indices of child and parent particles undergoing breakage. For all the child particles detected at any given scan the shape features are compared with those of their parent particles.

Figure 5.16a shows the normalized frequency for AR of child particles, each of these groups is characterized by a predefined range of AR of the corresponding parent particles. From the results, it is apparent that the AR values associated with maximum probability are close, and in some cases

even coinciding with the AR of the parent particles. Specifically, for parent particles with AR between 0.4 and 0.5, the generated fragments with AR between 0.4 – 0.5 constituted approximately 31 % of the total set of new fragments generated by those particles as they broke. This result explains the moderate trends of evolving particle shape statistics reported in Figure 5.14 (i.e., lack of bimodality upon breakage). In addition, it suggests that the fracture patterns responsible for size reduction vary with the shape of the parent particles in a way that tends to preserve the original shape prior to breakage, a process which is here defined shape heritability. To further stress the tendency to shape heritability upon successive breakage, the most frequent value of AR of a child particle (i.e., the AR associated with peak probability in Figure 5.16a) is correlated to the AR of their parent particles in each incremental breakage from timestep 3 to timestep 6 for all fitting methods. Such analysis, illustrated in Figure 5.16b, indicates remarkable correlation for all scans (R^2=0.988), thus confirming strong traits of shape heritability in the sequential breakage events. The figure also provides visuals of individual particle fractures leading to shape heritability. The examples clearly show that, although heritability can manifest in both elongated and spheroidal parent grains, the fracture patterns leading to it vary dramatically.

Further inspection of Figure 5.16a also indicates that heritability manifests with different intensity depending on the shape of the parent particles. Such differences can be quantified through the ratio between mean and mode of the aspect ratio frequency plots ($\overline{AR}/AR_p$). Coincidence between these values indicates near-symmetry of the frequency plots, i.e., an indicator of strong heritability, in that the mean AR of the parent particle population would nearly coincide with that of the child particle population. This trend is illustrated in Figure 5.16c, where $\overline{AR}/AR_p$ derived from the child particle frequency plots is shown to decrease dramatically with the AR of the corresponding

particles. In other words, heritability tends to be stronger for more elongated particles and weakens when the shape of the particles prior to breakage events is more spherical.

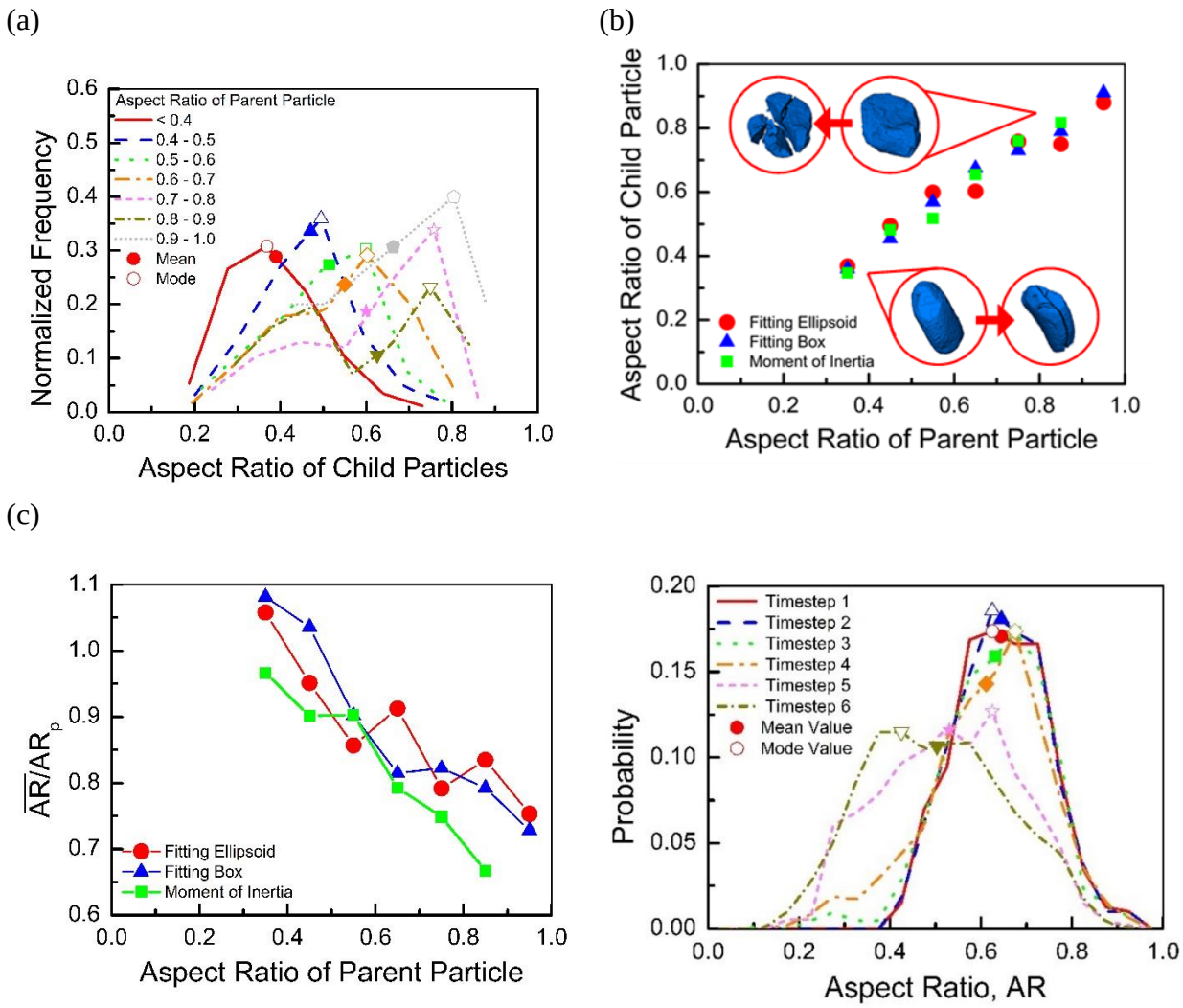

Figure 5.16. (a) Distribution of AR of child particle and AR of parent particle in incremental breakage during oedometer test. Correlation of (b) the mode and (c) the mean between AR of child and AR of parent particle in incremental breakage (d) Evolution of AR with the mode and the mean for the entire particles in Zingg diagram

Despite evidence of shape heritability upon breakage, the measurements indicate non-negligible alteration of the average shape of the particles within the specimen (Figure 5.13). This effect can be attributed to the lack of symmetry of the evolving particle shape population, and it is thus associated with the skewness of the AR frequency plots (Figure 5.16d). Specifically, in most cases

the frequency plots of AR are negatively skewed, implying tails of the distribution located on the left side of their peak. Such features imply that the average shape evolves towards lower values of AR compared to the initial conditions (i.e., it approaches an ultimate state with more elongated particles). Figure 5.16d illustrates this drift of the shape index distribution for the entire particle population. It is apparent that the gap between the mode and the mean of the entire AR distribution grows upon continuous compression.

5.5 Concluding Remarks

The effect of the grain shape on the compression of crushable granular soils was assessed at particle and assembly scale via sequentially imaged oedometric compression experiments. High-resolution X-ray tomography images for two sands (subrounded Ottawa sand and subangular Q-ROK#2 sand) consisting of particles with different initial shape were acquired in-situ during confined compression. To determine the role of the initial particle shape on the compression behavior, the processed images were analyzed statistically, and the emerging patterns of particle fracture were classified on the basis of simple breakage categories (i.e., splitting, chipping and comminution) through the methods described in Chapter 4.

The main findings of the study are summarized as follows:

1. Although the morphology of subrounded particles changed more severely compared to subangular grains, both sets of particles reached a similar shape at the end of the tests, displaying lower sphericity and higher elongation compared to their initial conditions. This

result suggests that continuous compression can mitigate morphological differences, especially when the stress is sufficient to induce pervasive breakage

2. Subrounded particles were found to develop more efficient cushioning than subangular particles by hindering the damage of larger grains even in the early stages of compression. This result reflects a tendency of subangular grains to exacerbate local contact indentation and damage and was corroborated by statistical analyses which pointed out that angularity (either initial or induced by fragmentation) broadens the range of particle sizes affected by damage mechanisms.
3. A statistical analysis of particle fracture events displayed that, although the average number of fragments produced by each particle steadily increases, incremental events detected by successive scans indicate the emergence of an average number of new particles between 2 and 4. This result did not depend on the shape of the particles affected by the crushing events. In addition, a classification of the failure mechanisms into splitting, chipping and comminution showed that pervasive comminution (i.e., the crushing of a grain into a multitude of fragments) emerges from a sequence of successive chipping and splitting events.
4. The emergence of cushioning was verified by inspecting the dependence of the failure mechanisms on the size of the parent particles. In particular, it was found that in both sands splitting dominates the incremental compression response at high stress, as well as that such splitting events concentrate into the finest grain fractions, thus shielding larger grains from failure.

Furthermore, to characterize the evolving distribution of particle shape, three fitting protocols (MVE, MVB and MIE) are proposed and used in conjunction with a tracking algorithm recording

the breakage history of individual particles to Ottawa sand. This strategy enabled the detection of incremental breakage events, as well as the quantification of correlations between the morphological properties before (parent particles) and after breakage (child particles). The key findings of the shape evolution in incremental breakage can be summarized as follows:

5. Even though the selected fitting strategies for the principal lengths exhibited quantitative differences in the absolute value of those lengths, all methods led to consistent trends of nondimensional indicators, which can thus be regarded as robust metrics to assess particle shape evolution.
6. Sharp changes in principal particle dimensions were detected at compressive stress levels higher than the nominal yielding pressure, indicating that conventional macroscopic protocols to define yielding do not fully capture the dynamics of particle-scale inelasticity.
7. The acquisition of digital images at selected stress levels pointed out the emergence of bimodal fragments size distribution, signaling co-existence of multiple particle population (e.g., intact grains and crushed fragments). Such bimodal trends, however, were not identified with respect to the particle shape populations (here quantified in terms of their aspect ratio, AR), for which a continuous transition towards a more elongated average shapes were found.
8. Further inspection of successive changes in particle shape upon fracture pointed out that such moderate changes in shape were linked to a strong correlation between the shape of parent and child particles, a phenomenon here defined shape heritability. Heritability was found to be stronger in finer, elongated particles and to become more prevalent at higher breakage.

9. Inspection of individual breakage events indicated that the fracture patterns responsible for size reduction vary with the shape of the parent particles. However, the measurements pointed out shape distribution curves skewed towards low aspect ratio values. This trend, attributed to the prevalence of small fragments at high pressure, was found to cause steady loss of particle regularity and convergence towards more elongated particle shapes (i.e., morphological ratios departing from unity).

By providing a 3D identification of the concurrent evolution of particle sorting, grain shape and fracture mechanisms, these results shed light on the feedbacks between the continuum-scale response and the particle-scale processes involved in the compression of sand. On one hand, these findings provide explicit validation of earlier predictions based on multiscale models. On the other one, they provide new data to enhance the methods currently used to explain and/or predict the mechanics of penetration in granular deposits and the compaction of crushable aggregates. In a more general context, they can assist the characterization and simulation of processes in which the co-evolution of grain sorting, size and shape impacts the mechanical behavior of sandy soils subjected to extreme pressures.

Chapter 6. SHAPE-DEPENDENT COMPRESSION OF CRUSHABLE SINGLE PARTICLES

6.1 Introduction

Particle morphology significantly affects the deformation properties of sand. This is confirmed by extensive evidence, especially focused on bulk properties such as density, flowability, compressibility, and frictional strength (e.g., Antonellini et al., 1994; Radjai et al., 1999; Goldenberg and Goldhirsch, 2005; Mair et al., 2002; Anthony and Marone, 2005). In the context of high-pressure compaction, the particle shape is known to influence the yielding point, *i.e.*, the transition between elastic and inelastic regimes (McDowell & Bolton, 1998; Coop et al., 2004; Shin & Santamarina, 2013; Brzesowsky et al., 2014). For example, spherical grains tend to yield sharply, while angular particles display a smoother response (Nakata et al., 2001). Such coupling between particle shape and compression behavior is linked to the role of the grain morphology on the resistance of particles (Cavarretta et al., 2017), including the possibility for crushing to emerge gradually during a macroscopic compression test (Pestana and Whittle, 1995; Das & Bajpai, 2018). These observations are now facilitated by non-destructive full-field techniques, such as 3D x-ray tomography. For granular assemblies these methods enable fracture processes, fragment geometry, and inter-particle interactions to be resolved (Zhao et al., 2015; Alikarami et al., 2015; Karatza et al., 2018; Zhao et al., 2020) and recently allowed quantification of the prevalence of breakage events in irregular grains compared to spherical-shaped grains (Karatza et al. 2019; Viggiani et al. 2019; Seo et al., 2020).

Despite such evidence, the explicit incorporation of the evolving shape of grains into predictive models has been lagging. Notable exceptions are discrete element model formulations enabling

arbitrary particle shapes (Harmon et al., 2020) and continuum frameworks listing shape descriptors among their state variables (Buscarnera and Einav, 2021). Both require nonetheless an accurate depiction of the crushability of non-spherical brittle grains. In this context, the dependence of the strength of the particles on their morphology finds its origin at microscopic scales. Tang et al. (2001) observed that round grains can sustain 21% higher load compared to irregular particles, in that they are less susceptible to microcrack initiation. Brzesowsky et al. (2011) used Hertzian contact mechanics to derive a strength criterion for non-spherical grains by accounting for the size of pre-existing flaws and the surface curvature. While their study did not encompass explicit descriptors of particle shape, it suggested that the consideration of asperities led to a superior match against measurements compared to Weibull weakest link models with pre-existing flaws scaling solely with the particle volume. Along similar lines, Zhang et al. (2016) used multiple contact deformation and fracture models to derive energy limits at the failure of single particles. In addition to offering scaling relations between particle strength and size, they enabled a straightforward link to energy-based continuum breakage models, thus informing the mechanics of whole assemblies and explaining measurements of bulk crushability obtained for granular materials made by particles with different shape (Sohn et al., 2017). However, lack of explicit shape descriptors into the energy criteria prevented a general quantification of how changes in morphology modulate the particle strength, thus restricting the ability to diagnose shape effects only for cases in which radical changes in morphology (*e.g.*, comparisons between assemblies made either by very round or very angular particles) modify entirely both individual and collective fracture mechanisms.

This chapter aims to extend the aforementioned frameworks of interpretation and determine the effect of particle shape on their crushing resistance by mechanical models accounting for deviations from a spherical geometry. The models are designed to enable straightforward

computation of both the forces end the elastic strain energy at particle fracture, following the approach of Zhang et al. (2016). We adopt various contact deformation and particle failure laws relying on a 3D ellipsoidal fitting of non-spherical particles, eventually incorporating the three principal lengths and their corresponding nondimensional ratios in the models. In conjunction with these analytical developments, we conducted particle compression experiments on 100 particles. We used x-ray topography to characterize the geometry of the particles and assess the relative performance of the proposed models in accounting for the effect of the geometry on the changes in strength.

6.2 Shape-dependent Particle Strength Fracture Models

In this study, shape is defined as a component of the more general notion of morphology aimed at addressing the coarsest-scale irregularities responsible for distinguishing a natural grain from a sphere (Barrett, 1980). In fact, while other morphological attributes exist at lower length scales (e.g., asperities controlling the particle roundness or even the surface texture of grains responsible for their roughness), here we focus on deviations from the geometry of a sphere caused by properties with characteristic dimensions having the same order of the particle diameter (i.e., elongation, flatness). This study evaluates three model scenarios to assess shape effects on the fracture strength of single particles with embedded microscopic flaws: (i) centre crack, (ii) contact crack, and (iii) weakest link model (sketched in Figure 6.1). For all models, the primary input data enabling deviations from the corresponding spherical models are three principal lengths calculated through a minimum-volume fitting ellipsoid circumscribing the particle giving the representative shape (i.e., ellipsoid) from non-spherical groups through one of the simplest ways to quantify the

principal lengths. Centre and contact crack models are deterministic criteria based on precise configurations of the applied load and potential crack nucleation sites. The centre crack model assumes that the applied force generates tensile stress oriented perpendicularly to the loading axis, thus resulting into mode I fracture at the center of the particle (Frost et al., 1999). By contrast, the contact crack model assumes that the largest tensile stress leading to fracture occurs at edge cracks proximal to the contact point where the compressive force is applied (Tuitz et al., 2012). For the analyses discussed here, the determination of such tensile stress levels is largely based on the strategy proposed by Zhang et al (2016) for spherical grains, with modifications accounting for geometric changes either of the cross-section subjected to crack nucleation or of the contact geometry. For the weakest link model, the generally adopted Weibull statistics is modified to account for the non-spherical geometry of the particles. In addition to enable convergence to standard models (e.g., Zhang et al. (2016)) if the three principal lengths coincide, such variables facilitate the use of widely used datasets and classifications of particle morphology (Zingg, 1935; Krumbein, 1941; Barrett, 1980).

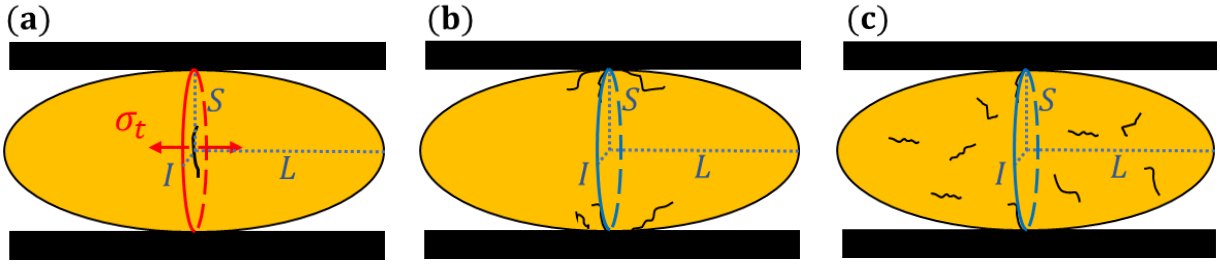

Figure 6.1. Graphical descriptions of the three fracture models proposed: (a) centre crack (b) contact crack (c) weakest link model (Weibull's statistics)

Conventionally, the characteristic strength at the particle scale, σ_{pc}, can be expressed as:

$$\sigma_{pc} = \frac{F_f}{D_p^2} \tag{6.1}$$

where F_f is the force at failure, usually measured through uniaxial compression tests on single particles and D_p is the particle diameter. For an ellipse it can be computed from principal lengths as:

$$D_p = (2S \cdot 2I \cdot 2L)^{1/3} \tag{6.2}$$

where *S*, *I* and *L* are the smallest, intermediate, and longest principal particle dimensions, respectively.

While the theoretical models in this study can consider three principal lengths, as it will be shown hereafter simpler versions of the proposed criteria can be obtained for the specific cases of a prolate (i.e., $S = I < L$) or an oblate (i.e., $S < I = L$) ellipsoids. The principal lengths can be used to compute non-dimensional shape indicators, such as the aspect ratio, AR, as:

$$\mathrm{AR} = \frac{S}{L} \tag{6.3}$$

This ratio describes the particle shape independently of the particle size. In the following we present the three proposed failure models as a function of this ratio.

6.2.1 Centre Crack Model

In centre crack models the largest tensile stress is assumed to develop along the median axis of the particle and to initiate failure through the growth of thin pre-existing flaws (Hiramatsu and Oka, 1966). The pre-existing crack propagates when the stress intensity factor K_I equals the fracture toughness for mode I, K_{IC} (Kassir and Sih., 1966). K_I can be readily computed under the assumption that the crack size is proportional to the particle radius as a function of a constant of proportionality, α:

$$K_I = \frac{2}{\sqrt{\pi}}\sigma_t\sqrt{\alpha R} \tag{6.4}$$

Where σ_t is the tensile stress at the crack tip. The fracture toughness for mode I can instead be expressed as a function of the critical energy release rate, G_{IC}, elastic modulus, E and Poisson ratio, ν as follows:

$$K_{IC} = \sqrt{\frac{G_{IC}E}{1-\nu^2}} \tag{6.5}$$

From Eq. (6.4) and (6.5) follows that the tensile stress initiating crack growth for an ellipsoidal elastic-brittle particle can be computed as:

$$\sigma_{tc} = a'\sqrt{\frac{G_{IC}E}{1-\nu^2}}S^{-\frac{1}{6}}I^{-\frac{1}{6}}L^{-\frac{1}{6}} \quad with \quad a' = \frac{\sqrt{\pi}}{\sqrt{2\alpha}} \tag{6.6}$$

The largest tensile stress given by estimated in accordance with earlier propositions by Hiramatsu and Oka (1966), as follows:

$$\sigma_t = \frac{2.8F}{\pi(2S)^2} \tag{6.7}$$

where *2S* is the distance between the points of load application, here assumed to coincide with the shortest principal length of the grain. This strategy is supported by the previous findings that non-spherical particles are positioned parallel to the shortest length to the loading direction under diametric compression test (Moss, 1972; Tuitz et al, 2012).

By substituting Eq. (6.6) into (6.7), the force at failure corresponding to centre crack fracture is:

$$F = \frac{4\pi}{2.8}a'\sqrt{\frac{G_{IC}E}{1-\nu^2}}S^{\frac{11}{6}}I^{-\frac{1}{6}}L^{-\frac{1}{6}} \tag{6.8}$$

In Eq. (6.8) the particle shape is reflected through three distinct values of principal length.

For a more general case, Eq. (6.8) can also be expressed as a function of two independent non-dimensional ratios, commonly referred to as elongation index (EI=*I*/*L*) and flatness index (FI=*S*/*I*) widely used for particle shape classification (Zingg, 1935):

$$\sigma = \frac{\sqrt{2}\pi}{2.8} a' \sqrt{\frac{G_{IC}E}{1-\nu^2}} \mathrm{EI}^{\frac{2}{3}} \mathrm{FI}^{\frac{4}{3}} {D_p}^{-\frac{1}{2}} \tag{6.9}$$

It can be readily shown that the expression above encompasses the case of prolate (FI=1; AR=EI) and oblate (EI=1; AR=FI) ellipsoids.

If a prolate geometry is assumed, the particle failure strength obtained from a centre crack model can be expressed as follows:

$$\sigma = \frac{\sqrt{2}\pi}{2.8} a' \sqrt{\frac{G_{IC}E}{1-\nu^2}} \mathrm{AR}^{\frac{2}{3}} {D_p}^{-\frac{1}{2}} \tag{6.10}$$

Where the effect of the particle size (through D_p) and shape (through AR) is clearly isolated.

6.2.2 Contact Crack Model

The contact crack model assumes that fracture initiates at pre-existing flaws located on the surface of a particle. In this class of models, fracture originates from near-contact tensile stress that can be quantified through the Hertzian contact theory (Brzesowsky et al., 2011). Prior studies by Antoine et al. (2006) enable the quantification of the force-displacement relationship between two elliptical solids establishing a Hertzian contact interaction, as follows:

$$F = \left[\frac{2^3}{3} \frac{E^*}{(\delta^*)^{3/2}(\rho_x + \rho_y)^{1/2}}\right] \delta^{3/2} \tag{6.11}$$

where $E*$ is an equivalent elastic stiffness defined as $E/(1-\nu^2)$, ρ_x and ρ_y are two contact curvatures, and δ^* is a dimensionless contact deformation defined as:

$$\delta^* = \frac{2\mathcal{F}(\kappa)}{\pi}\left(\frac{\pi}{2\kappa^2\mathcal{E}(\kappa)}\right)^{1/3} \tag{6.12}$$

In this study, we calculate the particle strength based on the contact between an elastic ellipsoid and a rigid plate (Antoine et al., 2006). To infer the value of tensile stresses along the contact periphery, the contact curvatures, ρ_x and ρ_y ($\rho_x \leq \rho_y$) are approximated by $1/r_x$ and $1/r_y$ where r is the radius of curvature (Antoine et al., 2006). r_x and r_y are then calculated as L^2/S and I^2/S according to (Regen 1996). $\mathcal{F}(\kappa)$ and $\mathcal{E}(\kappa)$ in Eq. (6.12) are complete elliptic integrals of the first and second kinds, which can be approximated by asymptotic expressions depending on the ellipticity parameter $\kappa = a/b$ (≥ 1), where a and b are determined with semiaxes of elliptical area of contact. Based on the definition of ellipticity of the contact area, κ can be expressed as $(L/I)^{4/3}$ (Greenwood, 1985; Dyson, 1965; Brewe and Hamrock, 1977). For a Hertzian contact model, such approximated elliptical integrals exhibit an error of 0.003 – 0.0005 % from the exact solution, which can be considered acceptable for the current application (Antoine et al., 2006; Tanaka, 2001; Bryant and Keer, 1982).

The tensile stress at the surface contact can be expressed in accordance with earlier results by Timoshenko & Goodier (1951), as follows:

$$\sigma_t = \frac{1-2\nu}{2}\frac{F}{\pi a_c^2} = \frac{1-2\nu}{2}\frac{F^{1/3}}{\pi R}\left(\frac{2^3}{3}\right)^{\frac{2}{3}}\left(\frac{E}{1-\nu^2}\right)^{\frac{2}{3}}\delta^{*-1}\left(\rho_x+\rho_y\right)^{-\frac{1}{3}} \tag{6.13}$$

According to Goddard (1990), the contact radius a_c proportionally increases following displacement δ (i.e., $a_c = \sqrt{R\delta}$).

The critical tensile stress at the onset of Hertzian fracture can be expressed as in Zhang et al. (2016):

$$\sigma_{tc} = b'\sqrt{\frac{G_{IC}E}{1-\nu^2}}{D_p}^{-\frac{1}{2}} \; with \; b' = \frac{1}{1.12}\left(\frac{\pi\alpha}{2}\right)^{-1/2} \tag{6.14}$$

where *b'* is a corrective geometric coefficient.

The contact crack propagates when the tensile stress around a Hertzian contact reaches the critical stress in Eq. (6.14), with the corresponding failure load given by:

$$F = \frac{9}{2^9}\left(\frac{2\pi b'}{1-2\nu}\right)^3\left(\frac{1-\nu^2}{E}\right)^{\frac{1}{2}} G_{IC}^{\frac{3}{2}}\delta^{*3}\left(\rho_x+\rho_y\right){D_p}^{\frac{3}{2}} \tag{6.15}$$

In addition, by equating Eq. (6.15) with Eq. (6.1) with EI and FI,

$$\sigma = \frac{9}{64}\left(\frac{2\pi b'}{1-2\nu}\right)^3\left(\frac{1-\nu^2}{E}\right)^{\frac{1}{2}} G_{IC}^{\frac{3}{2}}\pi^{-2}\left(\frac{\mathcal{F}^3\left(\mathrm{EI}^{-\frac{4}{3}}\right)}{\mathcal{E}\left(\mathrm{EI}^{-\frac{4}{3}}\right)}\right)\left(\mathrm{EI}+\frac{1}{\mathrm{EI}}\right)\mathrm{EI}^{\frac{10}{3}}\mathrm{FI}^{\frac{4}{3}}{D_p}^{-\frac{3}{2}} \tag{6.16}$$

In the case of a prolate geometry, Eq. (6.16) becomes:

$$\sigma = \frac{9}{64}\left(\frac{2\pi b'}{1-2\nu}\right)^3\left(\frac{1-\nu^2}{E}\right)^{\frac{1}{2}} G_{IC}^{\frac{3}{2}}\pi^{-2}\left(\frac{\mathcal{F}^3\left(AR^{-\frac{4}{3}}\right)}{\mathcal{E}\left(AR^{-\frac{4}{3}}\right)}\right)\left(\mathrm{AR}+\frac{1}{\mathrm{AR}}\right)\mathrm{AR}^{\frac{10}{3}}{D_p}^{-\frac{3}{2}} \tag{6.17}$$

which shows explicitly the effect of size and shape through D_p and AR, respectively.

6.2.3 Weakest Link Model

The Weibull's weakest link model (Weibull 1951; Brzesowsky et al., 2011; Nakata et al., 1999) has been commonly used to quantify the statistical variability of particle strength and the influence of the particle volume, V_p, on its characteristic stress, $\sigma_{pc,0}$, as:

$$\sigma_{pc} = \sigma_{pc,0}\left(\frac{V_p}{V_{p0}}\right)^{-\frac{1}{w}} = \sigma_{pc,0}\left(\frac{SIL}{S_0 I_0 L_0}\right)^{-\frac{1}{w}} \tag{6.18}$$

where *w* is the Weibull modulus. This can also be expressed through dimensional volume ratios and the principal shortest length *S* with the principal length ratios as:

$$\sigma_{pc} = \sigma_{pc,0}\left(\frac{S}{S_0}\right)^{-\frac{3}{w}}\left(\frac{\mathrm{FI}}{\mathrm{FI}_0}\right)^{\frac{2}{w}}\left(\frac{\mathrm{EI}}{\mathrm{EI}_0}\right)^{\frac{1}{w}} \tag{6.19}$$

Where the '0' subscript indicates the reference value of each variable. There is no independent effect of the particle shape on the strength statistics underlying Eq. (6.19). *S* remains as a dimensional quantity in the model as it was found to be the most influential in the compression of non-spherical grains (Hiramatsu and Oka, 1966; Moss, 1972; Tuitz et al, 2012).

Eq. (6.19) can be generalized to be a power law function of the type:

$$D_p = D_0\left(\frac{S}{S_0}\right)^{w\prime} \tag{6.20}$$

where *w'* is a power law coefficient determined from data-driven fashion by recognizing that certain correlations exist between principal lengths and volume-equivalent diameter.

The size and shape effects can be isolated in Weibull's statistical prediction of particle strength in Eq. (6.19) as:

$$\sigma_{pc} = \sigma_{pc,0}\left(\frac{D}{D_0}\right)^{-\frac{3w\prime}{w}}\left(\frac{\mathrm{FI}}{\mathrm{FI}_0}\right)^{\frac{2}{w}}\left(\frac{\mathrm{EI}}{\mathrm{EI}_0}\right)^{\frac{1}{w}} \tag{6.21}$$

For the specific case of Ottawa sand grains, this correlation is depicted in Figure 6.2.

Here exponential *w'* is found to be 1.017 with a coefficient of determination of 0.836 for Ottawa sand particles.

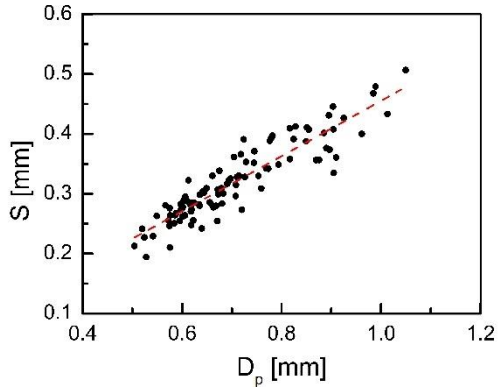

Figure 6.2. Relationship between principal length S and equivalent particle diameter D_p for the Ottawa sand used for the uniaxial compression test

It should be noted that, while this result applies to prolate geometry, similar results can be obtained if an analogous power laws relate Eq. (6.21) with the w' of Ottawa sand.

$$\sigma_{pc} = \sigma_{pc,0}\left(\frac{D}{D_0}\right)^{-\frac{3.051}{w}}\left(\frac{AR}{AR_0}\right)^{\frac{1}{w}} \tag{6.22}$$

6.3 Single Particle Compression Test (Materials and Procedures)

To verify the predictability of the models with experimental data, we performed a series of single grain compression tests on US silica Ottawa (quartz sand) with a median diameter of 0.707 mm. 100 single particles were manually selected to range across multiple aspect ratios and size, while avoiding major protrusions and maintaining consistent color features (a common indicator of the dominant mineral constituents). Previous studies of particle shape effect involve comparisons between different types of sand (Zhao et al., 2015; Sohn et al., 2017). Here the selection of particles of the same material provides more controlled conditions to isolate the role of individual factors.

To characterize the particle geometries a series of x-ray tomographies were acquired. Due to access restrictions, the particles were scanned at two different facilities. Specifically, 36 particles were

scanned at the 13 BM-D beamline at the Advanced Photon Source of the Argonne National Laboratory in Lemont, IL, USA (setup sketched in Fig. 54a) and 64 particles were tested at Laboratoire 3SR in Grenoble, France (Fig. 54b).

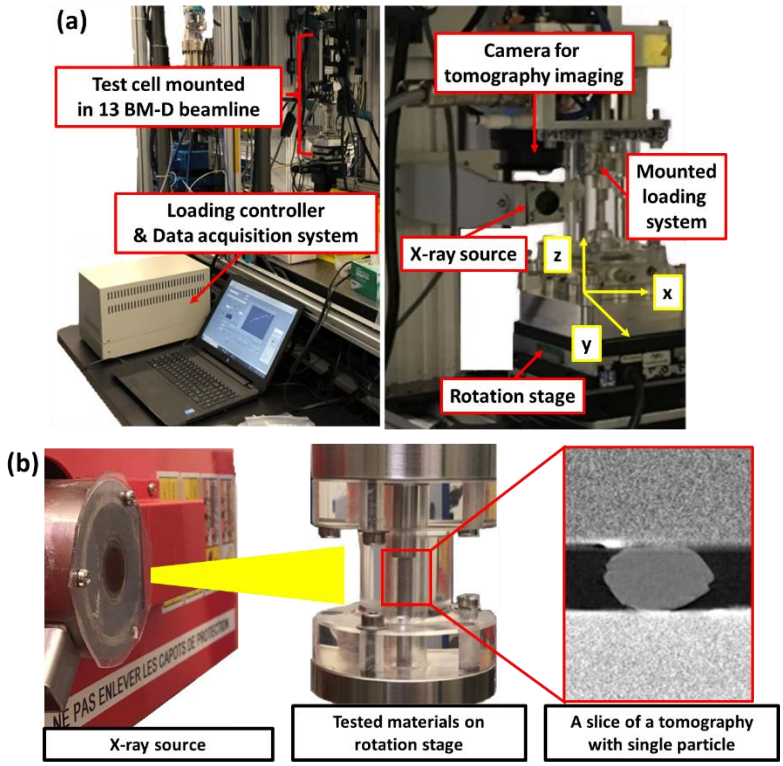

Figure 6.3. Setup used for single particle uniaxial compression tests at (a) GSECARS 13-BM-D, APS, Argonne National Laboratory, USA and (b) Laboratoire 3SR, Grenoble, France

The 13 BM-D facility is a synchrotron X-ray microtomography, (SMT) which offers a high intensity X-ray beam with energies ranging from 4.5 to 80keV. The scans in this study were conducted with a pink beam, which allows for fast scanning (exposure 0.008s) by adopting a relatively broad energy bandwidth centered around 40 keV, chosen to fall in the ideal range for solid and pore phase contrast (between 25 to 40 keV) (Rivers, 2016). 1800 projections were acquired around a 180° rotation at a pixel size of 3.14 μm. The X-ray tomograph at Laboratoire 3SR is instead a laboratory-scale scanner with a cone-beam (Viggiani et al., 2015). A

polychromatic beam with average energy around 40 keV was used in this study. 1024 images were acquired over 360°, each the result of the average of 6 radiographs. The pixel size is in this case 9 μm.

After matching the image resolutions to 9 μm per pixel, the grains were segmented (isolated) though filtering and thresholding (Seo et al., 2020). The binarized images were fitted with a circumscribing minimum ellipsoid yielding. Its shortest (*S*), intermediate (*I*) and longest (*L*) lengths, as illustrated in Figure 6.4a, 6.4b show the correlation between *I* and the median value of *S* and *L* (i.e., *(S+L)/*2). The median is slightly smaller than *I*, indicating that *I* is closer to *S* than *L*. Based on this observation, the following derivations assume prolate particles ($S = I < L$) to take advantage of the simplifications of the proposed analytical models.

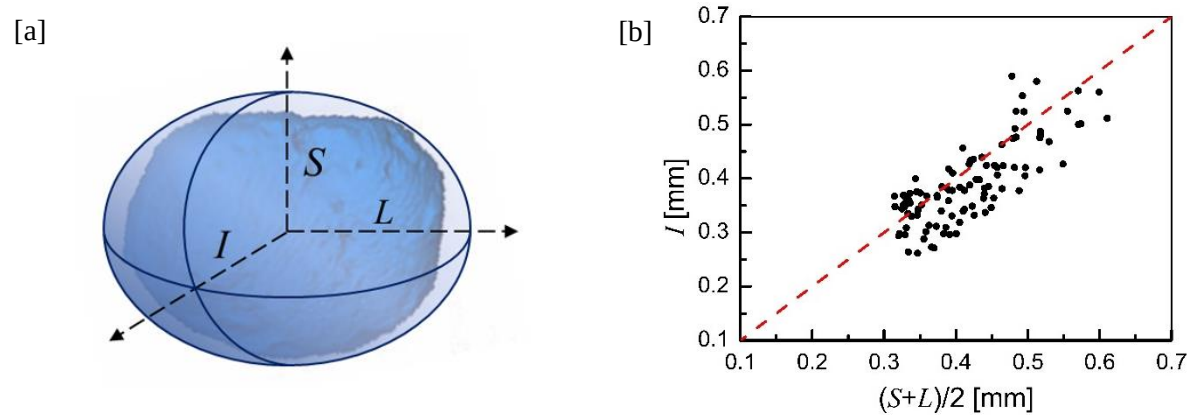

Figure 6.4. (a) Schematic of the minimum volumetric ellipsoid for the principal lengths of the single particle (b) Ratio between the intermediate length and the average of the minimum and maximum ones, justifying the assumption of prolate ellipsoids adopted below

6.4 Results and Data analysis

6.4.1 Theoretical model predictions

The trends of predicted particle strength resulting from the three models are reported in Figure 6.5 for varying size and shape characteristics and for the sets of model constants in Table 1. Figure 6.5a, 6.5c, 6.5e display increasing particle strength with aspect ratio (markers) under constant

equivalent diameter (lines with same color and style). All models predict that more elongated grains break at lower stress than round sand under point load compression. Such dependence of the particle strength on the aspect ratio is consistent with that reported in experimental studies (Tuitz et al., 2012; Karataza et al. 2019). In log scale, the trend lines display a constant slope of 2/3 and 1/4 for centre crack and Weibull's models, respectively, while for the contact crack model the slope of the predicted trend curve increases with AR, displaying an average value of 1.13 between AR=0.3 and 0.8. The resulting ranges of particle strength depend on the specific model. For example, between AR=0.3 and 0.8, the contact crack model provides the sharpest increase in particle strength with a reduction of elongation (i.e., step-like variations in AR of 0.1).

The strength was found to vary between 20% and 29% for every 10% variation in aspect ratio. By contrast, the Weibull model displays the weakest shape effects, with strength variations for equal increments in AR fluctuating between about 3% and 7%. The centre crack model shows intermediate trends, with a strength variation for each increment of AR by 0.1 from about 9% and 21%. Those degrees of strength variation in particle strength depend on particle size: smaller grains are more susceptible to particle shape variation in the predicted strength. Figure 6.5b, 6.5d, 6.5f show the particle size effect predicted by the three models. It is apparent that the particle strength decreases with an increase of the nominal particle diameter, D_p, thus being in agreement with existing evidence. Also in this case, the contact crack model shows the highest susceptibility to changes in particle geometry (predicted strength varying up to more than 28% for an increase in D_p of 0.1mm), while the centre crack model provides the most moderate levels of size sensitivity (up to about 10% strength for a similar size variation) and the Weibull's model displays intermediate trends.

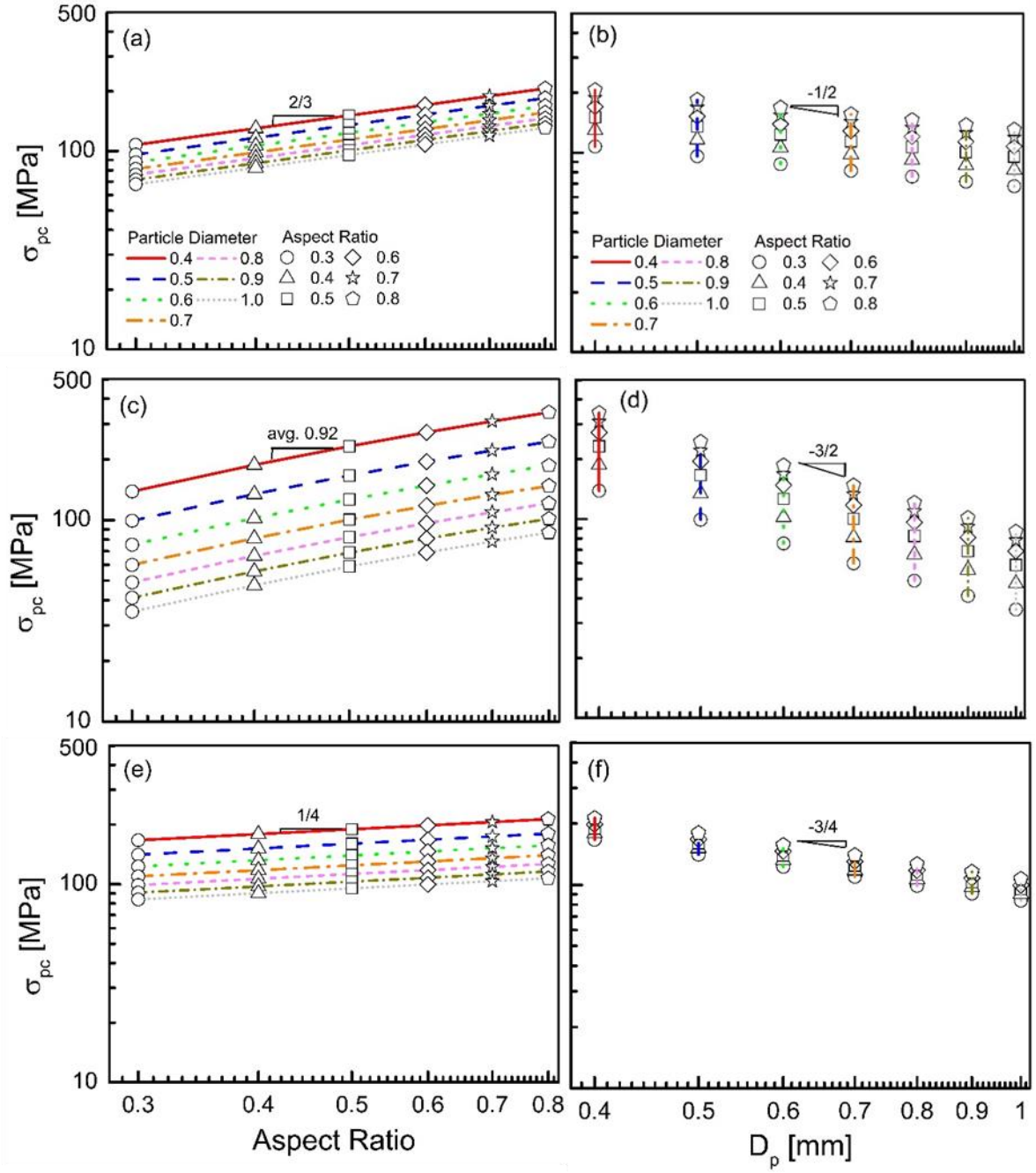

Figure 6.5. Effect of aspect ratio (a,e,c) and equivalent particle diameter (b,d,f) for the three proposed models: centre model (top), contact mode (mid) and Weibull's statistic (bottom)

To facilitate the comparisons between the shape and size effects predicted by each model, the functional relations providing the value of stress at failure, $\sigma = f(\mathrm{AR}, D_p)$, were normalized by the strength of particles characterized by reference values of the two variables. This enables the

derivation of simple power law expressions for most of the reference models, with the intensity of the size and shape effects quantified by the power law exponent, as follows:

$$\text{Centre crack model: } \frac{\sigma_{\mathrm{AR}}}{\sigma_{\mathrm{AR0}}} = \left(\frac{\mathrm{AR}}{\mathrm{AR}_0}\right)^{\frac{2}{3}} \tag{6.23}$$

$$\text{Contact crack model: } \frac{\sigma_{\mathrm{AR}}}{\sigma_{\mathrm{AR0}}} = \frac{f(\mathrm{AR})}{f(\mathrm{AR}_0)} = \left(\frac{\mathcal{F}\left(\mathrm{AR}^{-\frac{4}{3}}\right)}{\mathcal{F}\left(\mathrm{AR}_0{}^{-\frac{4}{3}}\right)}\right)^{3} \left(\frac{\mathcal{E}\left(\mathrm{AR}^{-\frac{4}{3}}\right)}{\mathcal{E}\left(\mathrm{AR}_0{}^{-\frac{4}{3}}\right)}\right)^{-1} \left(\frac{\mathrm{AR}+\frac{1}{\mathrm{AR}}}{\mathrm{AR}_0+\frac{1}{\mathrm{AR}_0}}\right)\left(\frac{\mathrm{AR}}{\mathrm{AR}_0}\right)^{\frac{10}{3}} \tag{6.24}$$

$$\text{Weakest link model: } \frac{\sigma_{\mathrm{AR}}}{\sigma_{\mathrm{AR0}}} = \left(\frac{\mathrm{AR}}{\mathrm{AR}_0}\right)^{\frac{1}{w}} \tag{6.25}$$

where *w* is equal to 4, the details of determining parameters will be discussed in Table. 1.

These relationships are plotted in Figure 6.6. Figure. 6.6a shows that the contact crack model is the most sensitive to the aspect ratio, while the weakest link model is the least sensitive. The high sensitivity of the contact crack model derives from a high effect of the aspect ratio on the contact geometry in the vicinity of the point of loading (Tang et al., 2001), and thus on the maximum tensile stress at the surface (Eq. (6.13)). In the centre crack model, intermediate trends of particle shape sensitivity are predicted, the particle elongation reduces the shortest principal length and thus the maximum tensile stress (Eq. (6.7)). Figure 6.6b reports the normalized particle strength predicted by the three models as a function of D_p. Also in this case, the contact crack model is the most susceptible to changes in geometry, while the centre crack model is the least susceptible to size and the weakest link model provides intermediate trends. This result is consistent with previous findings by Zhang et al. (2016) and it is here shown to be independent of the particle elongation, here embedded in the aspect ratio, AR.

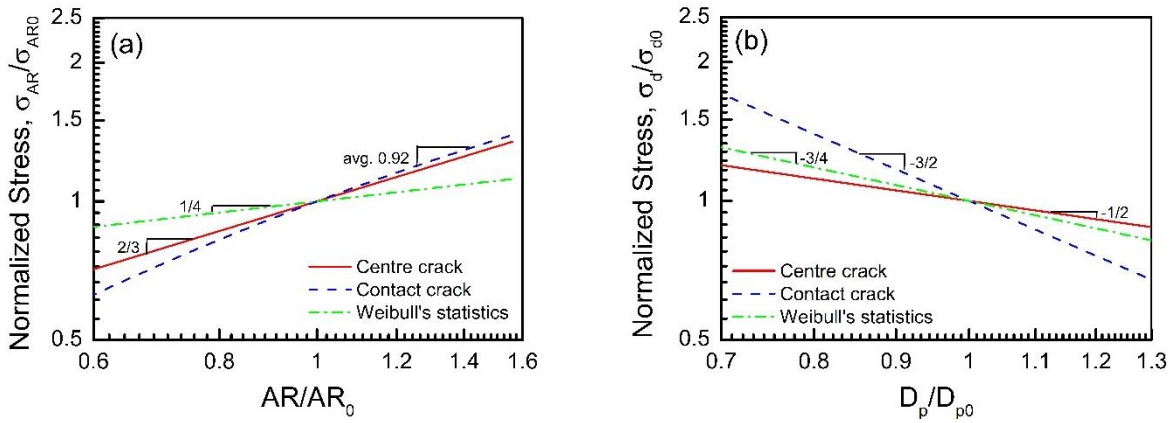

Figure 6.6. (a) Normalized shape-dependent stress excluding particle size (AR_0 = 0.64) (b) Normalized size-dependent stress excluding particle aspect ratio (D_p = 0.65)

In this study, the key benefit of the proposed models is applicability of two critical factors (i.e., shape and size) in single format. As an example of three-dimensional plot of this comprehensive model, Figure 6.7 displays the centre crack model with the colormap highlighting the particle strength.

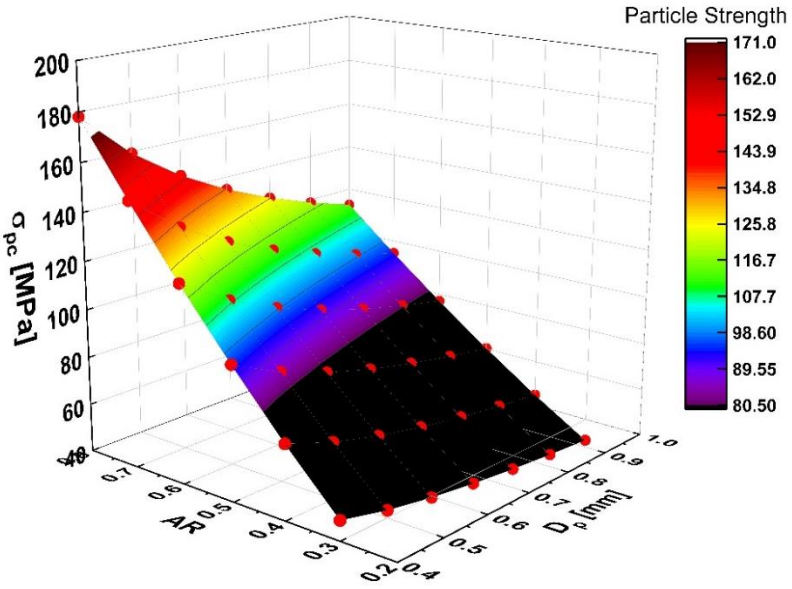

Figure 6.7. Three-dimensional plot showing the trends in particle strength predicted by the centre crack model as a function of size and shape

6.4.2 Experimental Data Interpretations

Figure 6.8a shows the correlation of AR and diameter of 100 tested particle ranging in both AR and D_p to explore the effects of both factors. The shape of the tested particles was assessed by dividing them into two populations, depending on whether individual grains were larger or smaller than the modal value of D_p ($D_{p,mode}$ = 0.640 mm). Note that $D_{p,mode}$ is here used only to distribute the data evenly into each batch, while the value of D_p used in the following analyses is the average value for the tested particles. Fig. 8b shows a normalized frequency curve in terms of AR for each population, from which it follows that the average AR considering all particles is AR_{avg}=0.64 with small differences between the groups (i.e., AR_{avg}=0.625 for smaller particles and AR_{avg}=0.642 for larger particles, respectively). The histograms in Figure 6.8b also show similar aspect ratio distributions for the two groups (i.e., small and large D_p), thus supporting the appropriateness of analyzing the four selected subgroups of AR in each group of D_p. The average characteristic properties of the four AR batches will be the reference points to analyze the tendency of shape and size effect in the following sections.

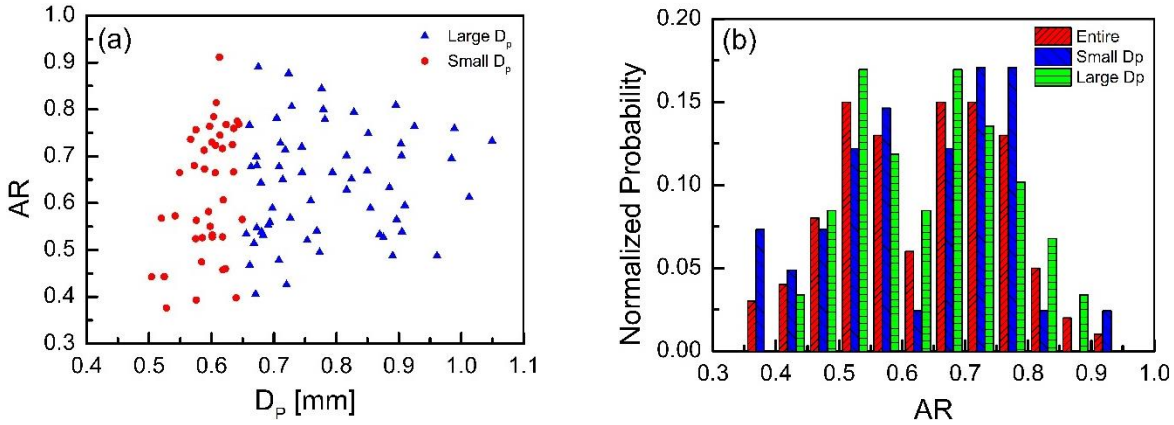

Figure 6.8. (b) Distribution of the tested particle properties on the plot of AR to D_p highlighting two equally sized subclasses around the modal value (b) probability distribution of the aspect ratios for all grains as well as for the two grain size populations individually

Diametrical compression tests were conducted to allow a direct comparison between maximum load and particle shape. The initial (i.e., prior to apply the loading) scans were performed in groups comprising multiple particles to reduce the overall scanning time. The particles were compressed at a constant displacement rate of 0.05 mm/min until a major drop in axial force, as exemplified in the force-displacement plot in Figure 6.9a. The sudden stress drop corresponds to the brittle failure of the particle and was used to determine the strength of each tested particle (pink shaded curves in Figure 6.9a). The peak stresses vary both in terms of failure point because of the scatter of AR and D_p in the tested particle, and because of the inherent statistical variability in particle strength. As observed before, smaller particles were observed to fail at lower loads than large particle of spherical shape. Regarding shape, Figure 6.9b shows an example of shape effect in force-displacement. Under similar equivalent diameter, it was found that the more elongated particles (AR = 0.398) breaks early than relatively spherical particles (AR = 0.775). The next sections study the effect of the geometry on the failure strength and interpret such effect through the proposed fracture models for non-spherical particles.

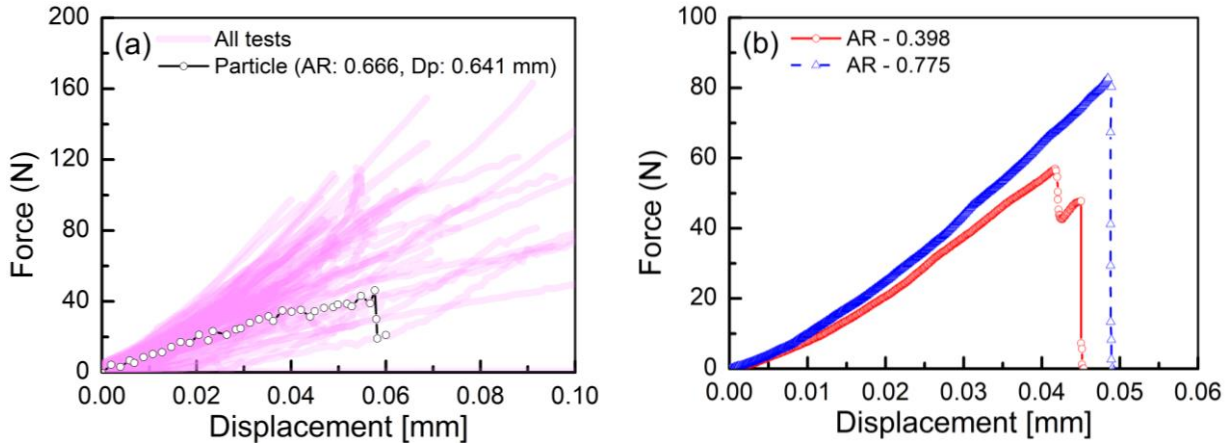

Figure 6.9. (a) Single-particle compression test results of all tested particles with a representative force-displacement showing major drop (AR: 0.666, D_p: 0.635 mm) (b) Force-displacement response for elliptical (AR: 0.398, D_p: 0.639 mm) and spherical (AR: 0.775, D_p: 0.641 mm) particles having similar diameter

6.4.3 Verification of Theoretical models

To assess the performance of the proposed analytical models, each of them was independently calibrated using the presented experimental dataset, as summarized in Table 1. The Young's modulus E, the Poisson ratio ν and the critical energy release rate for mode I fracture were calibrated based on existing datasets (Zhang et al. 1990, Nakata et al., 2001, McDowell, 2002). The reference particle diameter D_{p0}, aspect ratio, AR_0, and particle strength $\sigma_{pc,0}$ were based on the data discussed in the previous section. The geometric indexes *a'* and *b'* in the deterministic models were defined to match the strength of particles with average size and shape, in accordance with the strategy previously used by Zhang et al. (2016). Finally, the Weibull's modulus w was also selected to fit the measured strength values and is consistent with the reported range from previous studies (Nakata et al., 2001, Yashima et al., 1987).

Table 1. Calibrated parameters based on particle strength datasets

Material properties	
$E: GPa$	95.6
ν	0.077
G_{IC}: J/m^2	0.95
Geometric parameters	
a'	10
b'	3.34
Materials properties	
$\bar{\sigma}_{pc,0}: MPa$	140
$D_{p0}: mm$	0.65
AR_0	0.64
Weibull statistic	
w	4

To compare the performance of the different models, their ability to capture size effects was initially assessed independently from the particle shape. This procedure also allowed determination of multiple model constants used in the following stages of model verification. To

isolate the performance of the three models in capturing particle size effects, the particle shape was suppressed by referring to a spherical geometry (*i.e.,* AR was set to 1 in all models). Figure 6.10 presents measurements of particle strength for the size batches defined previously. The variability of the measurements is depicted via 95 % confidence intervals, with possible factors for such strength variations related to flaws and shape irregularity at the contact points. The analysis indicates that the centre crack model shows the best performance, with the weakest link theory also providing a reasonable match. Furthermore, the model prediction results coincide with the size-dependent crack models by Zhang et al (2016), thus confirming that the grain fracture models can be used to augment existing size-dependent particle strength criteria as a function of shape descriptors. This confirms that the grain fracture models proposed in this study can replace the previous version of single particle failure strength models which considers particle size while the fitting variables belonging to each model were adjusted differently.

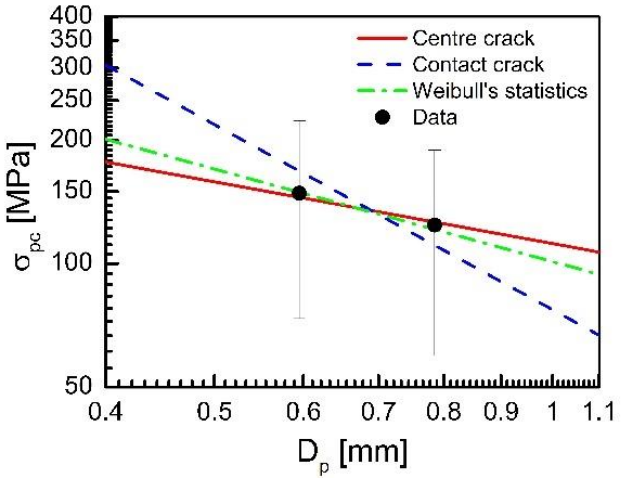

Figure 6.10. Size-dependency predicted by the three models. The error bars represent the 95% confidence interval of the characteristic particle strength

Figure 6.11a reports the measured strength of single particles as a function of the aspect ratio and the corresponding prediction of the three models. The experimental data is classified into the four AR batches (i.e., $AR_1 < 0.51$, $0.51 \leq AR_2 < 0.64$, $0.64 \leq AR_3 < 0.77$, $0.77 \leq AR_4 < 1.0$) from two

diameter groups respectively. Note that AR batches were determined to reasonably distribute the number of data in each batch. Overall, experimental data shows that the nominal strength of particles displays significant shape dependence, 53.68 % of particle strength increased within the range of increasing AR at the average D_p. Based on the three particle strength models with the parameters in Table 1, it was possible to predict such variations in strength related to AR effects. The resulting increasing strength in AR presents 58.74 % for the centre crack mode, 82.37 % for the contact crack mode, and 18.92 % for the weakest link model at the average D_p. This comparison shows that centre crack model can predict the shape dependence of failure strength. Despite well prediction of contact crack model for large D_p (plotted in triangle in Figure 6.11a), the centre crack model still performs well there while also having a more accurate prediction for small D_p (marked in circle in Figure 6.11a).

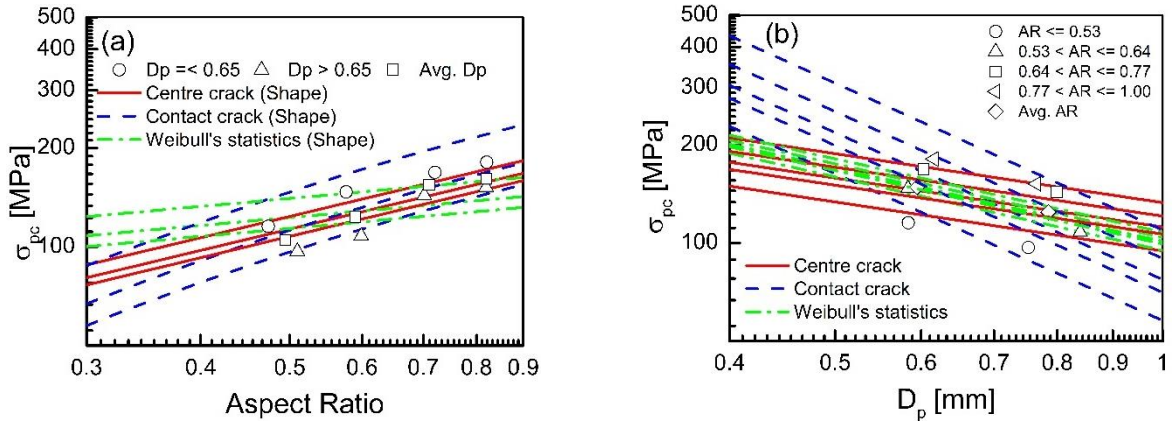

Figure 6.11. Predicted variation of failure stress as a function of particle (a) aspect ratio and (b) size

Figure 6.11b plots the results in terms of D_p for the four classes of AR. At the average AR (marked in rhombus), all groups predict a decrease in strength at larger diameters with the average 16.29 % of decreasing strength. The model predicts strength variations of 13.40 % for the centre crack, 35.05 % for the contact crack and 19.41 % for the Weibull's crack model. Once again, the centre

crack model delivers the most proper prediction to have both shape and size dependency. It is worth noting that strength fluctuations induced by shape variations are larger than those that can be attributed to changes in size, which indicates that in the tested group of particles the shape is the most significant geometric parameter controlling the strength variability.

Figure 6.12 plots the error, ε_p, to display a straightforward graphical comparison of the predictive performance. ε_p was calculated based on Eq. (6.26) where σ_{test} is the average strength belonging to each batch of tested materials and σ_{model} is the strength predicted with each model with the average AR and D_p from measured values of each batch. As shown in Figure 6.12, the centre crack model exhibits the best performance by having the minimum error overall (lined in red) in the prediction of single particle strength. Specifically, for small D_p groups in Figure 6.12a, the error embedded into the results obtained from centre crack model decreases with AR, becoming maximal at AR values close to 0. While this study did not attempt a visual observation of the developing fracture patterns, these findings suggest that centre crack may become prevalent in grains with highly spherical geometry.

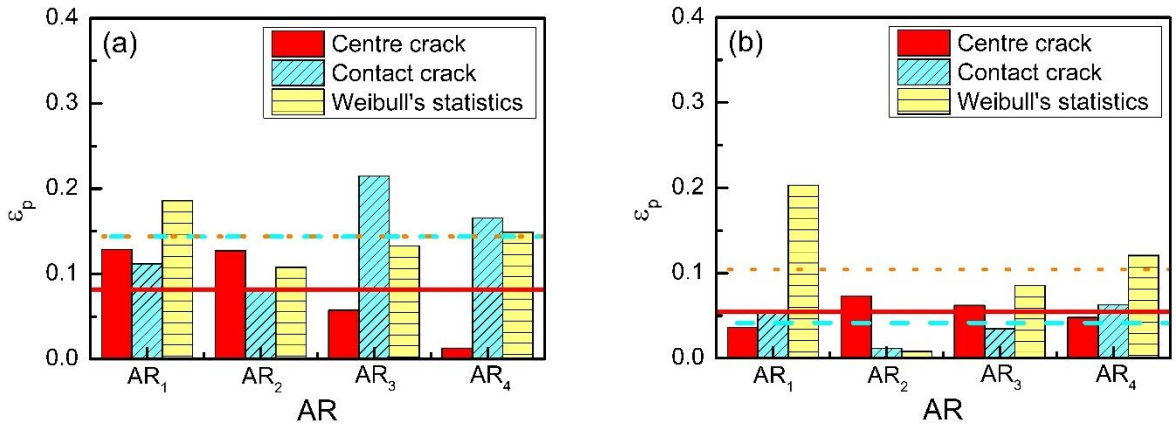

Figure 6.12. Prediction error ε_p of the models as a function of AR groups for (a) small D_p and (b) large D_p.

$$\varepsilon_p = \left|\frac{\sigma_{test} - \sigma_{model}}{\sigma_{test}}\right| \tag{6.26}$$

Figure 6.13 plots the normalized strength based on the strategy described with reference to Figure 6.6. This enables us to isolate size and shape effects regardless the particle grouping into small ($D_p \leq 0.65$, circle marker) and large diameters ($D_p > 0.65$, triangle marker). To eliminate the size effect on the experimental data in Figure. 6.13a, each strength measurement (or computation) was divided with the average particle strength of the D_p group (i.e., σ_{AR0} from data in D_p group). In case of shape effects, the normalized value for the experimental data was σ_{d0} from each AR group (Figure 6.13b). This visualization further highlights the ability of each of the proposed models to capture the data trend, pointing out how the centre crack model returns the most accurate overall predictions, the contact crack model is largely inaccurate, especially with reference to the quantification of size effects, and the weakest link model provides an intermediate, yet largely acceptable, performance both in terms of shape and size effects.

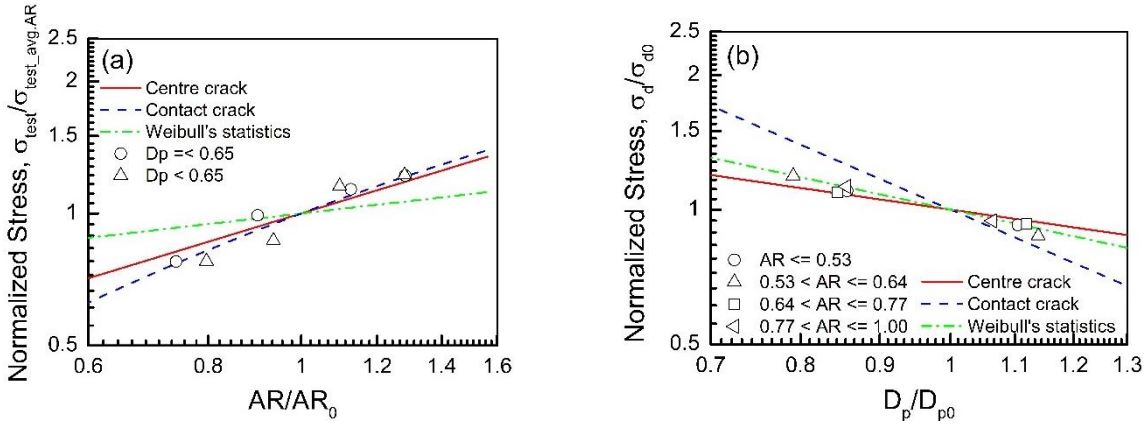

Figure 6.13. Normalized stress to (a) ratio of AR (b) diameter ratio

6.5 Concluding Remarks

This study proposes three single particle failure models accounting for both size and shape effects. Closed forms were derived as analytical expressions, were derived with reference to two deterministic modes of tensile fracture (centre crack growth, and contact fracture at edge cracks) and a statistical weakest link model based on the widely adopted Weibull distribution. Each failure model is enriched with 3D particle geometric features based on the ellipsoidal fitting and independently accounts for particle shape and size effects. The proposed derivations were tested by conducting diametrical compression experiments on individual grains of Ottawa sand. To enable high-resolution shape quantification, each grain was previously characterized through 3D x-ray tomography scans.

1. The experimental study was conducted for varying grain geometries and the aspect ratio of the tested grains was quantified through ellipsoidal approximation fitting. Experimentally, it was found that elongated grains are weaker than spherical particles of equal size and that their strength depends more on their shape than their size.
2. All proposed models display consistent behaviors to the experimental analysis of increasing strength with aspect ratio (i.e., elongated particles tend to have higher resistance) and decreasing strength with size (i.e., larger grains break at lower compression).
3. While all the models display varying performance depending on the combination of particle size and shape, a centre crack law for non-spherical grains is found to provide the best overall performance. Specifically, the centre crack model returned qualitatively similar but quantitatively more accurate trends and the overall best performance. Notably, given its fully deterministic nature and use of a minimal number of parameters, each with clear physical

meaning, the centre crack model can be regarded as the approach with the most economical calibration process and highest potential to inform the underlying particle failure mechanisms.

4. By contrast, the contact crack model was found to be the most sensitive to both size and shape, as well as the least accurate in capturing the size effect of the tested sand particles. However, at the same time, shape dependence was well predicted for large particles. This discrepancy may be attributed to local shape irregularities (e.g., asperities) that may cause stress concentration at contacts, here not fully captured by the proposed models, and which would warrant a finer-scale characterization of the contact curvatures.

These results offer an experimental and analytical foundation for upscaling laws to rationalize the effect of shape on the bulk crushability of granular materials.

Chapter 7. LS-DEM MODELING OF SHAPE-DEPENDENT SOIL CRUSHING

7.1 Introduction

Experimental data combined with sequential scans are critical in providing quantitative input for the characterization of mechanical processes. However, access to this data is limited in by the image resolution, thus leading to inevitable approximation of the characterized response metrics (e.g., deformation, particle rotation, breakage). To complement experimental data, this chapter performs computational analyses focusing on the determination of contact forces, i.e., variables of interest for mechanical analyses but not accessible through pure visual observation. In fact, DEM techniques nowadays enable the conduction of virtual experiments, which can fill the gap of physical quantities that not yet accessible via standard characterization protocols. However, due to the complex geometry of real grains, many studies are often restricted by the use of overly simplified shape models (e.g., sphere, ellipsoid, polygon, or block) (Ting et al., 1993; Ng., 2009; Liu and Zhao, 2020; Xia et al., 2022). This thesis argues that an accurate representation of the shape of the grains is essential to resolve the microscopic forces responsible for particle fracture.

For the above-mentioned reasons, this chapter discusses numerical analyses conducted by means of the so-called level-set DEM approach (LS-DEM). As described in Chapter 2, LS-DEM uses particle avatars reflecting the actual morphological features of particles, generated with level-set values. In specific, the level-set values reflect the morphological features by setting the surface points with zero level isosurface of a level set function set to negative values inside the particle (thus, marking the solid phase) and positive values outside the particle (thus, marking the void space (see Figure 2.8 in Chapter 2). In this study, breakage will be implemented by splitting a

particle into two at a single time step (in Chapter 2), with the goal to replicate and complement the experimental observations discussed in Chapter 5. This task will offer the possibility to quantify processes (e.g., force chain evolution) which were unavailable from traditional x-ray adsorption maps.

In this chapter, the first step will be the validation of LS-DEM with experimental measurements collected for Ottawa sand. The goal is to match both the macroscopic deformation response and the evolution of particle breakage (e.g., changes in GSD and shape parameters). The second step will be a comparative study examining the influence of different particle shape approximations on the predictive capabilities of the selected computational approach. Specifically, different particle models (e.g., spheres, ellipsoids, exact replicas) will be used to replicate the dataset, with the goal to identify the optimal level of particle geometry representation able to capture the key trends, while reducing the computational cost. Finally, the calibrated LS-DEM framework will be used to explore the evolution of the particle shape at ultimate conditions, by extending the loading process at pressure levels higher than those applicable through the testing setup used in Chapter 5. This step will be meant to infer the possible emergence of ultimate attractors for the shape of heavily crushed granular systems.

7.2 Validation of LS-DEM against breakage measurements

This part aims to validate the LS-DEM splitting technique for crushable grains with assembly- and individual particle-scale measurements. Then the model will compute contact forces linked to such breakage mechanisms, typically not accessible from conventional 3D X-ray scans. First, LS-DEM based on exact replica of the tested particles will be used to simulate oedometric compression. In

this stage, LS-DEM will be optimized based on the deformation response measured at the assembly-scale, as well as through measurements of evolving grain size distribution obtained from digital image analysis. This validated LS-DEM will then provide the evolving contact forces for comminution under uniaxial compression.

7.2.1 Oedometric compression simulation

After generating particle avatars with the level sets from 3D X-ray image as explained in Chapter 2, the virtual specimen was prepared by setting particle positions and orientations compatible with the measurements. Although the X-ray images possess a resolution of 4.28 μm/vox, to prevent potential memory issues in the simulations, the level-set resolution was reduced to 8.6 μm/vox. To alleviate instability due to the initial overlap between particles, the avatars were slightly shrunk to prevent contact at the initial stage.

Table 2: Summary of parameters in LS-DEM

Parameter	Value
k_n (MN/m)	1.5
k_s/k_n	0.9
μ	0.4
ρ (g/cm^3)	2.65
σ_{c0} (MPa)	10,000
d_0 (mm)	0.6
m	3.3
P_f	U[0,1]
Level Set Resolution $(\mu m/vox)$	8.6

Table 2 shows the parameters used for the analyses. Friction, μ and density, ρ were set based on typical values of reported for Ottawa sand (Ghoraiby et al., 2020). In terms of particle properties, the failure strength, σ_{c0} and its corresponding diameter, d_0 were set based on measurements from single-particle breakage experiments on Ottawa sand grains conducted by Nakata et al. (2001), while the value of Weibull's modulus, m was chosen in agreement with data reported for similar quartz sands (Zhang et al., 2016). In this modeling, only stiffness was calibrated based on the constitutive response of experimental results.

Figure 7.1a shows both the measured and the simulation deformation response corresponding to oedometric compression, with the model providing a satisfactory match. At selected axial strain levels (0 %, 3 %, 5 %, 6.4 %, 9.8 % and 13 %), the tested specimen was scanned to quantify the degree of particle breakage and its effect on the system. Such strain levels were chosen with the goal to cover both pre- and post- yielding regime (5 % strain corresponds to the compression yielding of Ottawa sand). The comparison between measured and computed GSD is shown at these selected strain levels, resulting in a satisfactory match between model and data (Figure 7.1a).

Figure 7.1b plots the evolution of Grain Size Distribution (GSD) quantified at each of the strain levels marked in Figure 65a. The GSD was calculated based on the percentage mass smaller than the equivalent diameter of spherical grain to have the constant volume of original particle. The initial two GSDs located in pre-yielding regime show constant curve due to few particle breakages. From 5 % strain, the GSD starts evolving clearly. The computed GSDs match reasonably the measured grading evolution, indicating that LS-DEM can capture the particle-scale response induced by breakage despite the assumption of planar fracture surface between the two highest contact forces. Due to the accuracy limits of digital images, the final GSD reported in this thesis

was determined at 13 % axial strain, which may not correspond to the idealized ultimate GSD at full comminution.

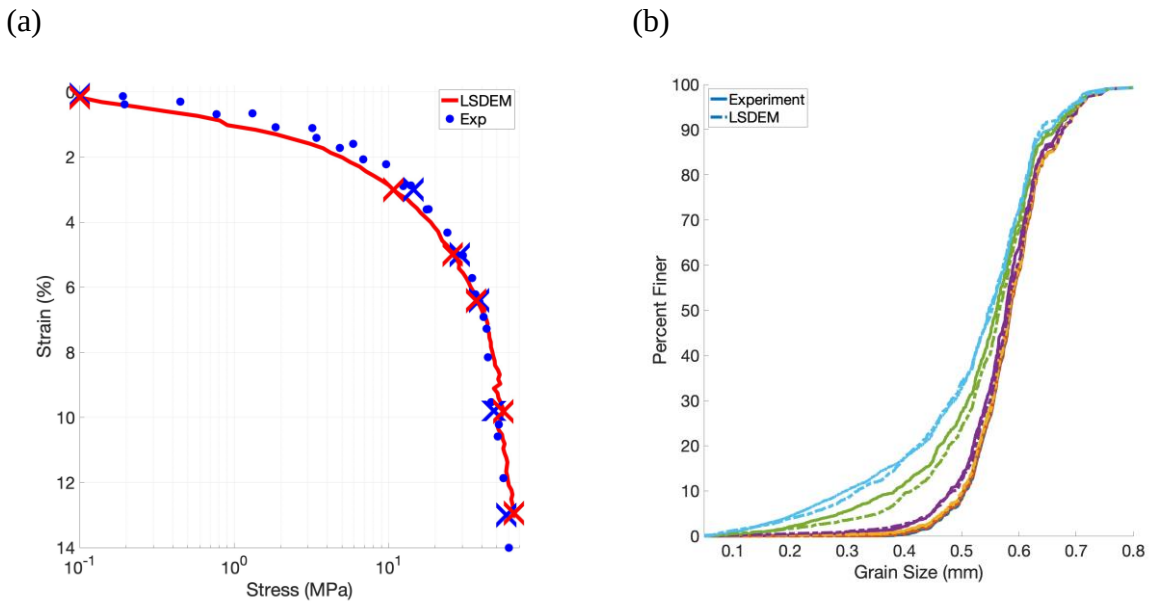

Figure 7.1. Comparison of between measurements and simulations in terms of (a) stress-strain curve and (b) evolution of the grain size distribution at selected strains (marked points in (a))

Figure 7.1b shows that the GSD evolves toward finer particles in both LS-DEM and experiment as broken particles tend to experience breakage again, as shown in Figure 7.2. At 13 % axial strain, a significant increase in the number of fragments predicted to result from more than 5 successive breakage events (colored in magenta) is shown. While breakage concentrated near the loading area due to boundary effects (Karatza 2017, Karatza et al., 2019), there was no clear pattern in the distribution of breakage occurrence in computational models. While this may be a result of missing factors in the DEM analyses (e.g., lack of consideration of friction at loading platens and container walls), the results here obtained through LS-DEM can be regarded as satisfactory and reflective of the overall mechanics of compression in the tested sand.

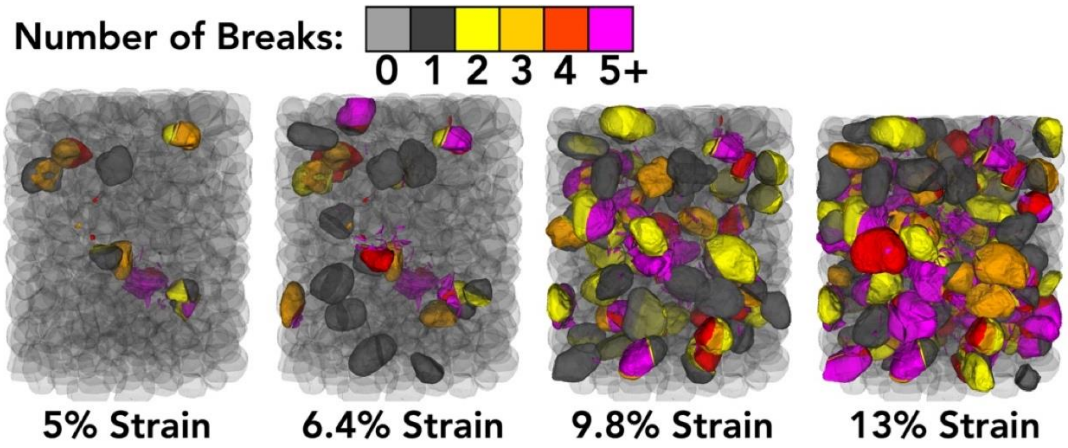

Figure 7.2. LS-DEM results reporting the number of successive breakage events suffered by each particle in the assembly. Colored particles represent broken grains which suffered a varying number of breakage events. Opaque shading indicates intact particles

7.2.2 Shape evolution simulation

As previously mentioned, LS-DEM enables the use of particle avatars in computational analyses, thus ensuring that all the simulated particles initially possess the same morphology of the tested sand grains. However, the possibility to preserve satisfactory agreement between measured and computed particle shape after the onset of breakage depends primarily on the accuracy at which local rupture mechanisms are simulated. Verification of such a capability can be therefore regarded as a crucial step to corroborate the reliability of the selected simulation protocol. In this respect, the distribution of individual particle shapes has been investigated by comparing data and simulations at multiple stages of the reference experiment. Hence, three shape metrics (i.e., sphericity, flatness, and elongation) often used in the literature were calculated (Blott & Pye, 2008; Ghoraiby et al., 2020). Specifically, sphericity, *S*, describes the similarity of an object to a sphere by measuring the ratio of the surface area of the sphere having the equivalent volume of the grain to its actual surface area from 0 (i.e., angular) to 1 (i.e., sphere) (Eq. (7.1)).

$$S = \frac{\sqrt[3]{36\pi V^2}}{SA} \tag{7.1}$$

Figure 7.3 shows frequency plots for the sphericity of the particles within the specimen. Intact particles were found to have a very narrow distribution of sphericity, with values concentrating between 0.90 to 0.95 (Figure 7.3a). After breakage, during which finer fragments are produced, a larger fraction of irregular grains begins to appear (values of sphericity between 0.45 and 0.80) and is readily apparent from Figure 7.3b. Along with this trend, under continuous uniaxial compression, the lower range of sphericity values continues to become dominant, indicating that the generated fragments tend to be irregular in shape. Furthermore, at the final stage, the dominant

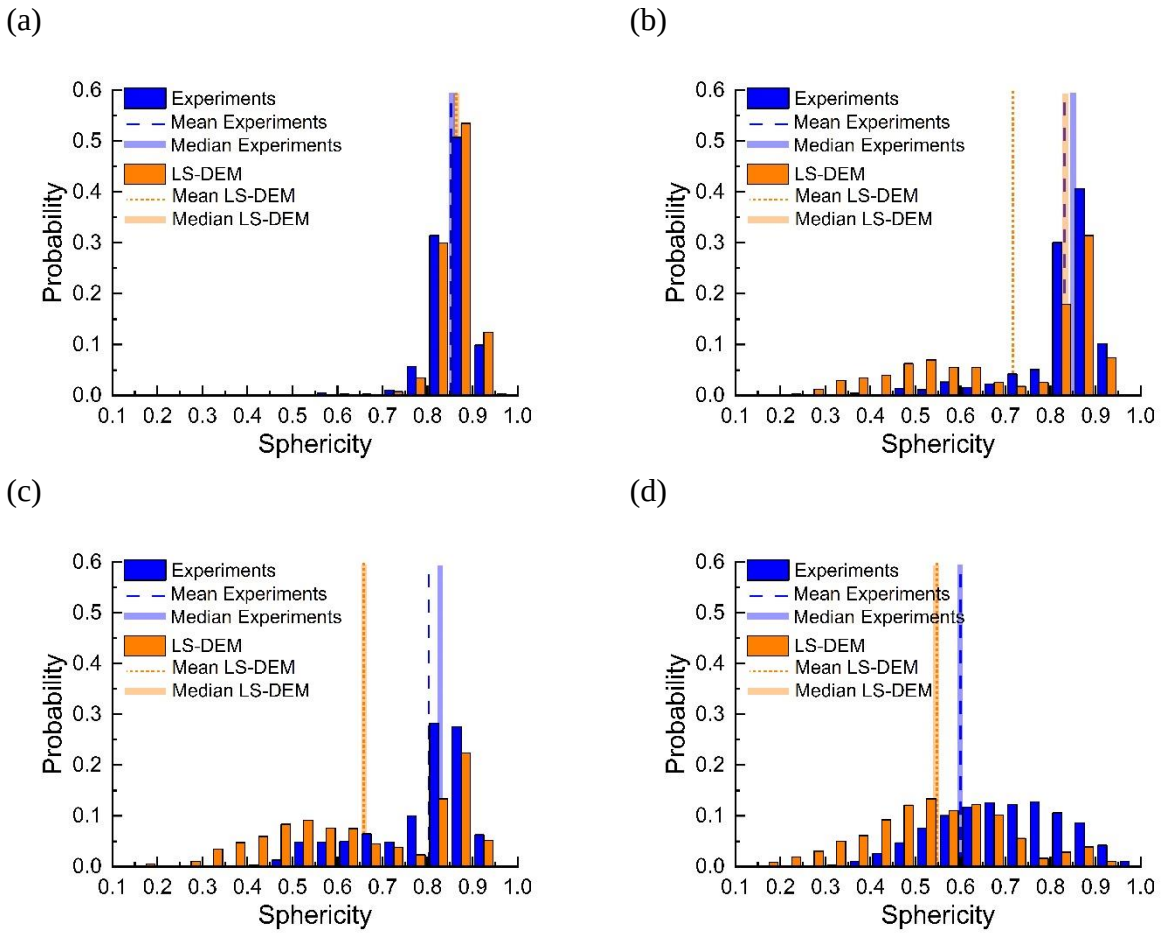

Figure 7.3. Sphericity distribution of the entire particle population at strain levels (a) 0 % (b) 5% (c) 6.4% (d) 13%. Blue indicates data, orange simulations

group of sphericities moved to lower range by having wider distribution of sphericity. Despite the presence of quantitative mismatches, likely resulting from the use of flat fractures representative of simple splitting events, the main trends were captured qualitatively by LS-DEM.

A similar strategy was also used for other shape metrics, namely the Flatness, i.e., a non-dimensional index providing a measure of how flat the object is (i.e., closeness to oblate) and expressed as the ratio of shortest length (S) to intermediate length (I) (Eq. (7.2)), and the Elongation quantifies the form of an object elongated along the pole (e.g., rod and prolate) through the ratio between intermediate length (I) over the longest length (L) (Eq. (7.3)) (Blot and Pye., 2008).

$$Flatness = S/I \tag{7.2}$$

$$Elongation = I/L \tag{7.3}$$

In this study, the principal lengths were obtained by fitting individual particles to a circumscribing ellipsoid set to have minimum volume. The average values of flatness and elongation calculated for individual particles are plotted for both data and simulations in Figure 7.4. In agreement with previous studies, these shape metrics move towards to lower range, indicating gradual convergence of more irregular shapes, with reduction of flatness from 0.80 to 0.61 in both approaches. Specifically, by comparing data and simulations, LS-DEM results have average errors of 1.08 % and 0.87 % from the measured flatness and elongation, respectively. This result indicates that the virtual test run through LS-DEM can reasonably simulate not only the macroscopic deformation response, but also evolution of particle-scale characteristics (i.e., size and shape of the crushed particles).

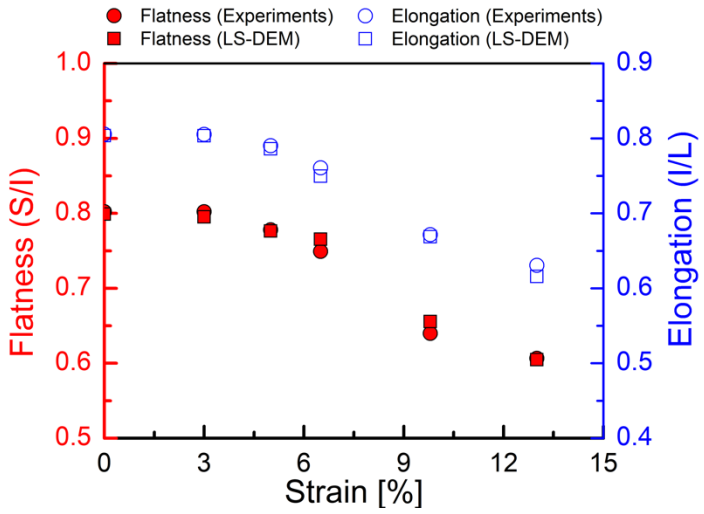

Figure 7.4. Evolution of average Flatness and Elongation for experimental results and LS-DEM data

7.2.3 Contact forces

As an outcome of LS-DEM analyses, the simulations discussed above provide the contact forces shown schematically in Figure 7.5, with reference to the scans reported in Figure 7.5a. Black lines present inter-particle contact forces with thickness proportional to the magnitude. As the stress in the specimen increases from left to right, there is a clear increase in higher magnitude contact forces. This is despite an increase in the total number of contacts from the increase in particle number indicating the effect of spreading out the stress over a larger number of contacts does not limit the increase in contact force with increasing compression.

Higher forces do not tend to exist in regions with high levels of breakage which we can observe by noticing a lack of thick black lines in the regions of particles that have experienced 5+ breaks. Another observation of the model is that if a particle is to break many times, it does so rapidly because one break is not often enough to alleviate the stress in the region. In the experiment it was shown that both “comminution” events where one particle breaks into many particles exist as well as “splitting” events where one particle breaks into only two particles. Despite the model only

allowing splitting events, there are many times where there are multiple subsequent splitting events that culminate to what could be described as a comminution event. After these comminution events the forces in that region significantly decrease and cause a cushioning effect on the surrounding particles. So, while most forces in the specimen increase with increasing stress, when particles experience many breakages the forces in that local region seem to decrease.

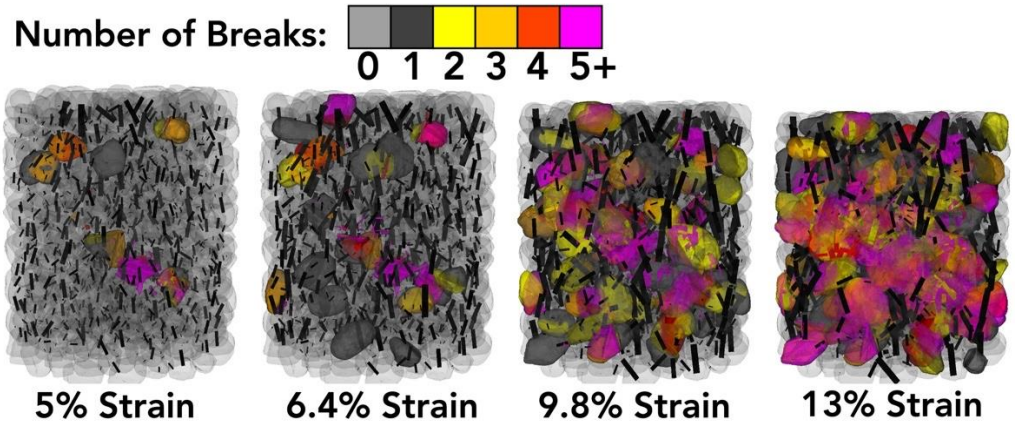

Figure 7.5. Same as Figure 7.2 but with interparticle contact forces added and opacity reduced for all particles to better visualize the contact forces. The thickness of the black lines is proportional to the force magnitude

In Figure 7.6a-d, the histogram of particle strength shows the evolution of the resistance of both unbroken and broken particle at selected strain levels corresponding to the scans. While unbroken particles that are generally larger do have lower average strength, there are many broken particles that have the same strength or are weaker meaning that large unbroken particles are not necessarily the weakest. In addition, large particles tend to have higher coordination and such condition allows them to benefit from cushioning effects without increasing the maximum principal stress. Figure 7.6e shows the variation in particle strength over successive scans for the broken particle group. The figure clearly shows that new breakage events tend to occur in units possessing the lowest range of particle strength.

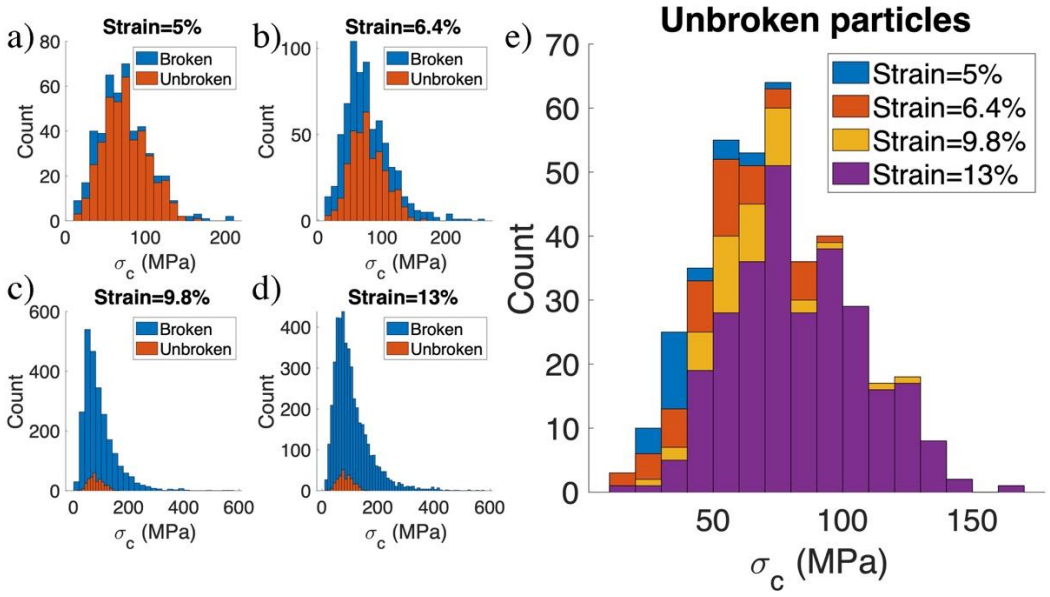

Figure 7.6. (a)-(d) Histograms of breakage stress for both broken and unbroken particles at strain 5%, 6.4%, 9.8% and 13% respectively. (e) Histograms of only unbroken particles for multiple strain levels indicating that breakage largely involves the weakest particles in the assembly

There is strong correlation between contact force and their volume in Figure 7.7a. It is worth pointing out that the volume in this figure is an average value of two contacting particles. To understand the proportion of the particles regarding their volume and strength, Figure 7.7b shows that the small particles (<50 % of the average particle volume) tend to carry low-magnitude contact force (<3 – 4 N) and rarely appear in the stress larger than 10 N. In large force range (> 15 N), the particles having twice volume than the average are shown. The directional distribution of contact forces in the granular system has been explored through a polar plot (Figure 7.7c) with reference to the final scan. By using the same strategy in Figure 7.7e, four groups of average paired-particle volume were classified in the polar plot. Bins near 90 or 270 degrees are the sum total of force magnitude in the vertical z direction, while bins near 0 or 180 degrees are the sum total of force magnitude in the radial, r, direction. Large amounts of force were seen in the vertical direction, and significantly less so in the radial direction. It was observed that the larger particles experience disproportionally more vertical force than radial force. The smaller particles on the other hand,

while still experiencing more force in the vertical direction, have a larger relative contribution to the total force in the radial direction than the vertical direction. The small particles then serve as lateral support so that the larger particles can maintain enough confinement to keep the stronger force chains from buckling. The smaller particles still hold significant force near the vertical direction as well however and must be the forces that are providing the bulk of the cushioning the larger particles experience.

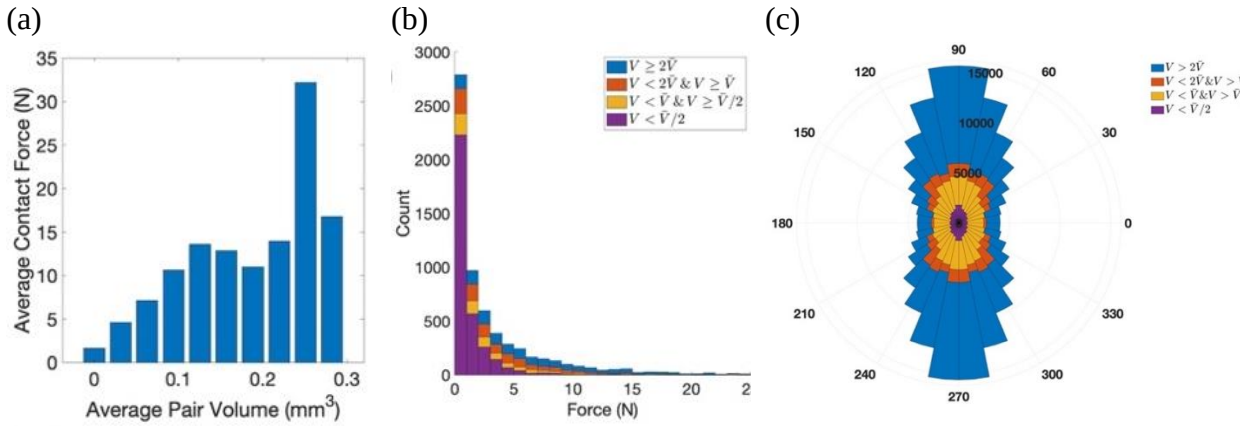

Figure 7.7. (a) Average contact force as a function of the particle volume fraction (b) Histogram of contact force magnitudes by particle volume (c) Polar plot of total force magnitude in each direction. Vertical forces on the plot indicate forces in the z-direction and horizontal indicate forces in the r-direction

7.3 3D Virtual Assessment of Shape Dependency in Crushable Soils

In this section, LS-DEM is used to perform virtual oedometric tests exploring one of the challenges that DEM modelers face today, i.e., how to accurately account for the complex morphological features of sand particles. As discussed in the previous section, LS-DEM can solve such problems by applying particles from 3D images, however few DEM programs support the function to generate particle domains with complicated morphologies exported from 3D images. Most notably, even when such images are available, it is not clear if a one-to-one replica of all the geometric attributes is strictly necessary, or if approximated, but computationally less expensive

simplifications of the real geometry provide a viable alternative. In this context, many DEM studies have assessed their results by comparing the features of specimens such as density and the peak shear strength to initial conditions at particle-scale and the deformation response at the assembly-scale due to the complication of considering individual particle attributes. In this section, to increase the accessibility of considering shape in general DEM simulations, the compression response of virtual sand specimens characterized by different particle morphology are explored, spanning from simple spherical approximations preserving only the volume of the original particles, to ellipsoidal approximations preserving also the aspect ratio and the principal axes orientation, to finally exact replica possessing the same fine-scale geometric attributes of their physical counterparts.

7.3.1 Generation of virtual sand samples

Figure 7.8 shows the generated particle avatars (i.e., sand, ellipsoid, and sphere) extracted from the same set of digital images relative to the initial condition of the tested specimen in Figure 7.1b. The sand avatars (Figure 7.8a, 7.8d) replicate the 3D surface features extracted from 3D tomography with the level set strategy discussed in Chapter 4. As a simpler representation of example grains, an ellipsoidal avatar was created by considering length ratios (flatness and elongation) reflecting the form of the example particles and by preserving their original volume (Figure 7.8b, 7.8e). By ignoring the shape but accounting only for the particle size, spheres can also be created with diameter guaranteeing an equivalent volume (Figure 7.8c, 7.8f).

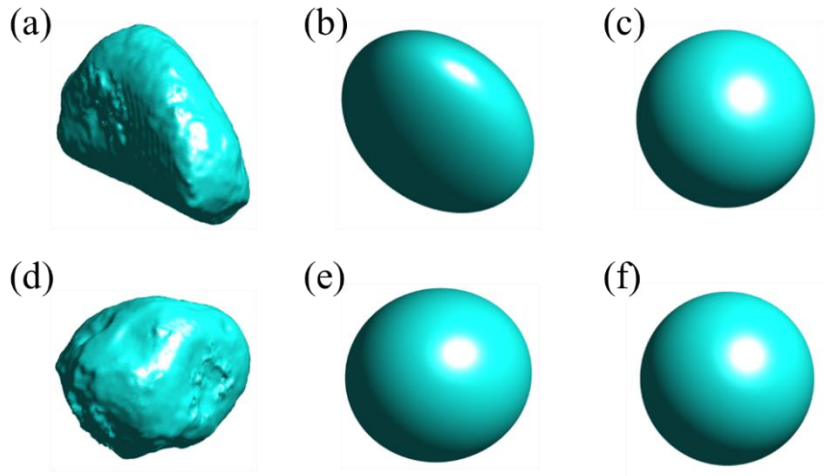

Figure 7.8. Particle avatar: Exact replicas (a,d), ellipsoid with aspect ratio of sand (b,e) and sphere with equivalent volumetric diameter (c,f)

The sample for computational analyses was prepared by mimicking the preparation procedure used in the experiments, i.e., by performing dry pluviation virtually. Specifically, dry pluviation is a method to pour dry grains into the specimen and was simulated by placing the particle avatars randomly into an empty virtual cylindrical container by preventing their overlap and having them to fall by gravity until satisfying a target void ratio (i.e., in this case 0.60). The specimens prepared with the three different particle sets illustrated in Figure 7.9 have identical GSD and initial void ratio, all based on measurements obtained from their physical counterpart.

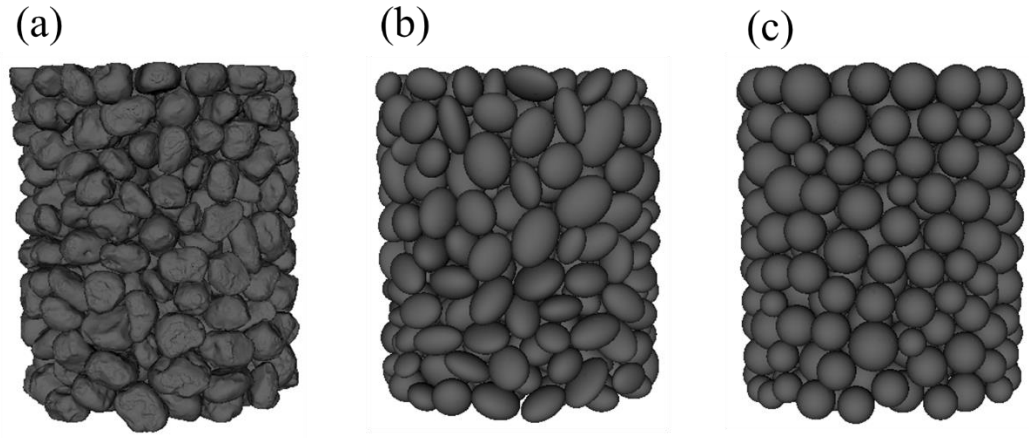

Figure 7.9. Sample preparation through X-ray image extraction and dry pluviation in LS-DEM with (a) exact replicas, (b) ellipsoids and (c) spheres

7.3.2 Oedometric compression simulation

Figure 7.10 plots the simulation results. The stress-strain behavior is represented through solid lines, while breakage initiation is signaled by markers. The simulations are based on the set of constant model parameters in Table 2, which was calibrated based on the sand avatar. It was found that the specimen made by ellipsoidal particles led to a satisfactory simulation of the compression response both in the elastic regime and the post-yielding regime (i.e., once breakage starts), during which breakage was found to cause an increase in macroscopic compressibility. By contrast, use of spherical particles was found to cause poor match of the constitutive response by showing higher compliance prior to yielding and lower post-yielding compressibility. Attempts of improving the match with experiments by adjusting the contact parameters were not deemed successful, in that they led to a systematic mismatch, especially in the pre-yield region, which suggests that the loss of simulation accuracy is an outcome of the excessive approximation of the initial particle shape. Such results correspond to the finding with experiments done by Wiacek et al. (2012) that varying the particle shape to oblong results in increasing stiffness of the specimen. It is considered that the changes of particle shape to greater aspect ratio increase the coordination, adding the rotational degrees of freedom in the system (Donev et al. 2004), and the particles with high aspect ratios in the system therefore rotates less (Ng, 2009). It may produce the stiffer response shown in Figure 7.10 with reference to the pre-yielding regime. Interestingly, all particles converged to a similar range of stress in the later stages of the post-yielding regime, indicating that the effect of the initial shape vanishes upon continuous breakage. These results indicate that the effective stiffness of the computational model to the granular system can vary significantly even in the presence of similar initial conditions (i.e., same initial GSD, porosity, and particle attributes). It follows that considering only the particle size distribution without explicit consideration of the shape

characteristics does not guarantee an accurate representation of the strain energy storage processes during compression, thus negatively impacting the overall simulation of the compression response.

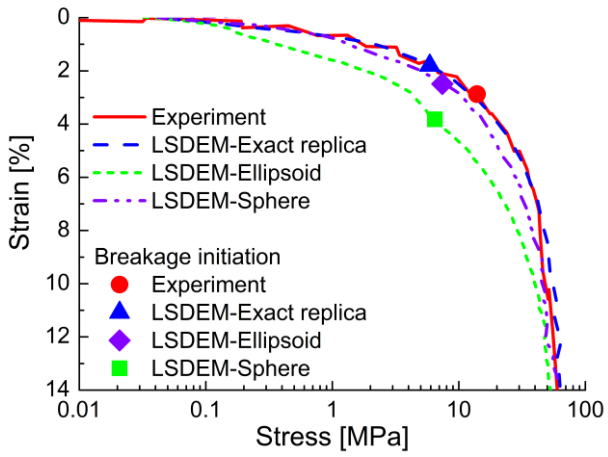

Figure 7.10. Compression behavior of Ottawa sand simulated through different geometric particle models (i.e., exact replicas, ellipsoids, spheres)

Regardless of the morphological features, initiation of particle breakage was computed in all cases to occur at about 7-8 MPa, thus slightly earlier than the first detection of breakage in the scans (13 MPa). It is worth pointing out that such a delayed initiation in the experiment may be an outcome of the scanning interval, in that it is likely that first breakage had occurred slightly earlier. The incremental breakage ratio was calculated as the ratio of newly generated fragments to the total number of particles in previous stage, the number of breakage event between two successive scans (Figure 7.11). As experimental analysis counts chipping, splitting and comminution as breakage, the breakage ratio is much higher than computational model simulating breakage through splitting. While the individual particle strength is constant, the assembly made by ellipsoids was found to have higher breakage ratio compared to the assembly made of spheres. This is a possible outcome of higher particle irregularity due to the aspect ratio, but reduced number of contact points due to the smooth surface of the ellipsoid, thus causing higher likelihood of force concentration in

general. By contrast, the assembly made of spherical grains displays the slowest breakage growth, thus reflecting the lower likelihood of stress concentration points in highly regular particles. Interestingly, Figure 7.11 shows that the assembly consisting of exact replicas of Ottawa sand grains displays an intermediate response between that of assemblies made by spheres and ellipsoids, indicating that particle irregularities do not significantly increase the likelihood of particle splitting. This mismatch with the measurements may therefore reflect the lack of chipping mechanisms in the computational models and indicates the possible need of further developing the breakage schemes in LS-DEM.

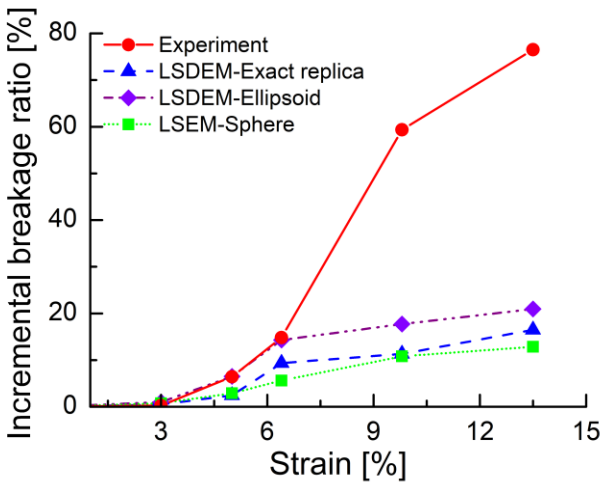

Figure 7.11. Breakage ratio: Comparison between Ottawa sand and simulation results through different geometric particle models (i.e., exact replicas, ellipsoids, spheres) at strain points

By comparing the computed trends of GSD evolution, the particle sizes were quantified in terms of equivalent diameter of a sphere having same volume of the original particle at each point (0 %, 3 %, 5 %, 6.4 %, 9.8 % and 13.5 %) in Figure 7.12a, 7.12c, 7.12e. The assemblies made by sand avatars display the best match up to the start of the post-yielding regime (6.4 % of strain rate) and a satisfactory trend overall. The assemblies made of ellipsoids showed the best performance in replicating the evolution of GSD after yielding (9.8 % and 13.5 % of strain rate).

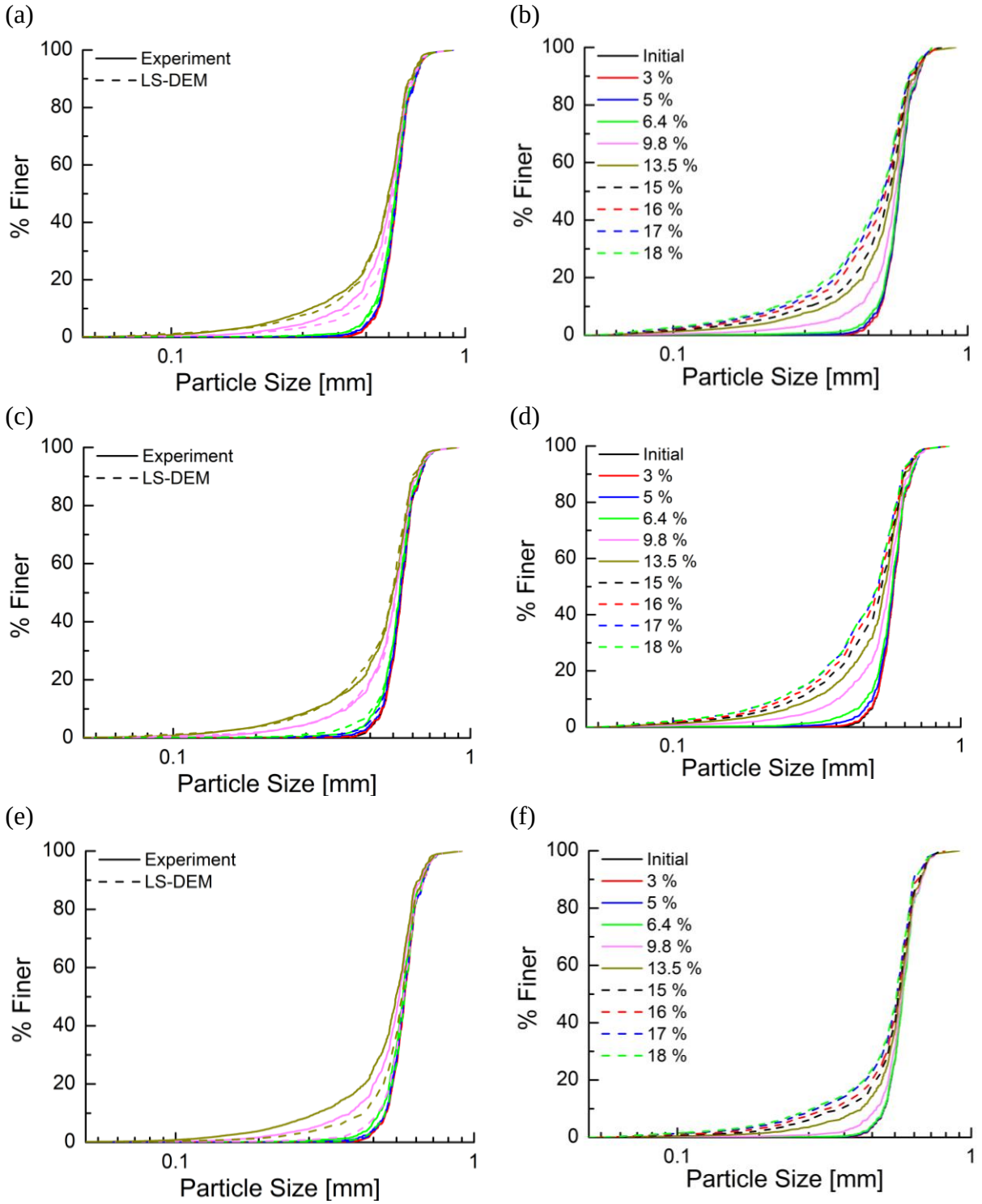

Figure 7.12. Evolution of the grain size distribution: Comparison between (a) assembly made of exact replicas (c) assembly made by ellipsoids and (e) assembly made by spheres, and evolution to ultimate grain size distribution (b) assembly made of exact replicas (d) assembly made by ellipsoids and (f) assembly made by spheres

On the other hand, the assembly made of spheres displayed the least satisfactory performance, especially in the post-yielding regime. This indicates that spheres models are overly approximated to simulate the high-pressure compression of granular materials. The GSD evolution was also simulated beyond the stress range examined in the experimental observation, i.e., beyond axial strain 13.5 % (Figure 7.12b, 7.12d and 7.12f). It was found that the rate of evolution reduces as the strain increases, indicating that the system approaches an ultimate GSD upon continuous breakage. This is well captured in Figure 7.12d, the large number of ellipsoids in the assembly experiencing early breakage as discussed in Figure 7.11 and such assembly may not undergo further changes in GSD between 17 % and 18 % of strain rates.

7.3.3 Shape evolution simulation

Figure 7.13 compares the average elongation and flatness of particles on the Zingg diagram by overlaying measurements and computational results. The length ratios were quantified with the principal lengths extracted from a fitting ellipsoid strategy. Since exact replicas and ellipsoidal avatars were generated based on digital images, the initial shape parameters are identical to 0.802 and 0.805 for elongation and flatness, respectively. By contrast, spherical models are bound to start from the top right corner (i.e., elongation=flatness=1 at the start of the simulation). In return, fragments from both virtual specimens based on either exact replicas or ellipsoidal models show similar tendency in shape factor evolution, with a good overall match of the experimental measurements. Specifically, the overall flatness and elongation in LS-DEM with exact replicas had average error of 1.782 % and 1.160 %, while simulated specimens based on ellipsoids resulted into 1.934 % and 1.376 % average error. In summary, the incorporation of actual 3D morphological features of the tested grains not only improves the performance in simulating shape evolution, but

it also enables an accurate representation of the macroscopic compression response and the collective shift in grading during breakage.

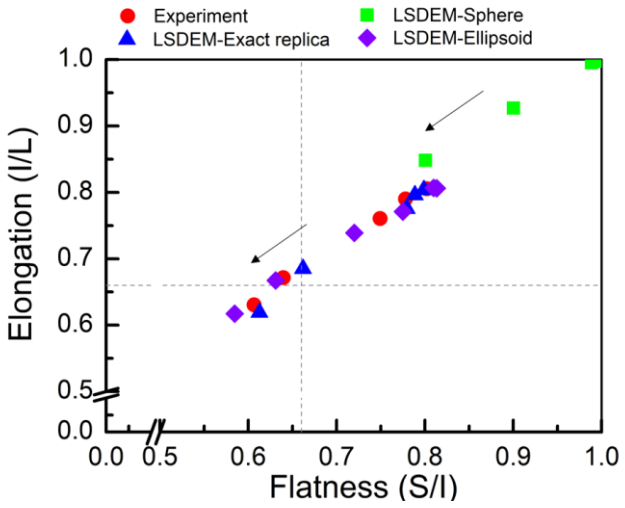

Figure 7.13. Zingg diagram: Comparison between experimental data and simulation results through different geometric particle models (i.e., exact replicas, ellipsoids, spheres)

Figure 7.14 reports in the Zingg plane the evolution of the shape indices relative to higher values of axial strain (i.e., ≥ 15 % of strain in Figure 7.14b, 7.14d, 7.14f). As discussed in Figure 7.12, the granular system may approach an ultimate state in terms of GSD. It is thus interesting to explore whether a similar ultimate condition exists in terms of particle shape. The numerical results indicate that the shape ratios tend to converge towards a narrow range (approximately, 0.55 of flatness and elongation). This result corroborates the idea of gradual approach of ultimate shape attractors recently discussed by Domokos et al. (2019) and incorporated in constitutive analyses by Buscarnera and Einav (2021). However, these values are lower than reported values of shape indices found in heavily crushed systems such as planetary impact sites and laboratory experiments (with 0.716 and 0.739 for average flatness and elongation), which indicates that further experimental and modeling studies are needed to define in greater detail the shape of particles at extreme levels of fragmentation.

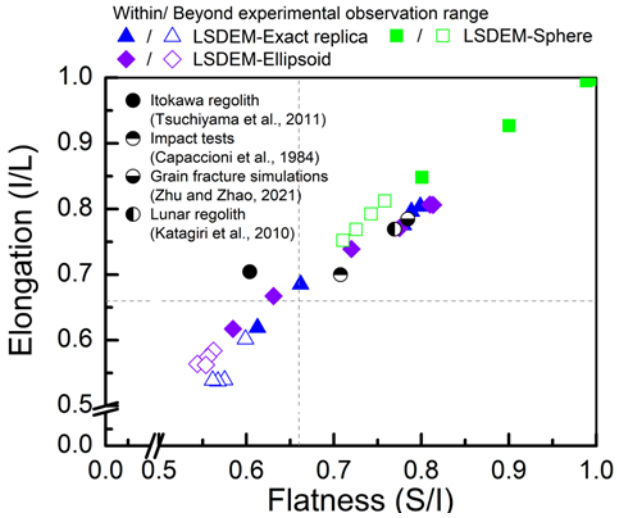

Figure 7.14. Evolution of the shape parameters computed for different virtual specimens subjected to high levels of compressive deformation and comparison with data from previous studies

7.4 Concluding Remarks

LS-DEM was used to examine the effect of the particle shape on the crushing response of sand by replicating an oedometer test conducted in situ with simultaneous X-ray tomography imaging. The goal of the study was to explore particle-scale processes, in addition to the macroscopic compression response, as well as to enrich the dataset with information not directly accessible from image analysis (e.g., contact forces). LS-DEM with three-dimensional level set splitting was calibrated based on measurements of compression response and the main findings of the study are as follows:

1. The comparison against the experimental data shows that LS-DEM accurately calibrated with digital images is able to satisfactorily predict both deformation response at assembly-scale and individual particle shape evolution. Even though the model replicates breakage through simple splitting mechanisms, the most significant metrics of crushing response have been accurately captured. This strengthens the perspective of using this strategy for future analyses involving high-pressure compression (e.g., impacts, penetration, blast).

2. A correlation between particle volume and contact forces was found. In addition, by observing the evolution of the contact forces, it was found that large forces contribute to the most significant fraction of stress bearing along the loading direction, while fragments generated from breakage contribute to the system deformation by sustaining lower-intensity forces that exert cushioning along the vertical direction and prevent buckling along the lateral direction.
3. Non-dimensional length ratios (i.e., elongation and flatness) quantifying deviations from a spherical geometry were shown to be useful metrics to quantify the ability of LS-DEM to track the evolution of particle shape attributes. It was shown that simplified ellipsoidal models accounting exclusively for the aspect ratio but losing detail in terms of fine-scale geometric features, were able to provide a satisfactory predictive performance at both grain and assembly scales. By contrast, spherical considering only the size distribution of the grains in assembly were found to yield a significant deterioration of the model performance at all length scales. This result suggests that considering one of the most easily accessible shape factors, i.e., the aspect ratio, can lead to substantial improvements of the performance of DEM models, without need to recur to computationally more expensive, and less accessible geometric representations.
4. LS-DEM was used to examine the evolution of shape attributes beyond the range of stress levels tested in the experiments, with the goal to identify the possible tendency towards a shape attractor. While non-dimensional shape factors were found to converge to values of 0.55 in terms of flatness and elongation, the mismatch with respect to values reported in the literature indicates the need to further study the existence of ultimate shape attractors both experimentally and computationally.

Chapter 8. CONCLUSIONS

8.1. Main Conclusions

Particle morphology is one of the key factors influencing the mechanical behavior of granular materials. Despite its importance, the quantification of the particle shape and its use in modeling is a challenging task, especially for granular systems susceptible to changes in the morphology of individual particles due to breakage. In this context, the goal of this thesis was to enhance our understanding of the breakage of granular materials in light of particle shape effects. The objectives of the study were: (1) to quantify the sequential evolution of different morphological indicators of sand grains under uniaxial compression tests with the aid of 3D X-ray tomography; (2) develop energy-based, shape-dependent breakage models at both grain and continuum scales, and (3) explore the response of granular materials by complementing measured datasets with DEM analyses fed with digital images.

To achieve these objectives, the research presented in this thesis used a diverse range of methods. First, recent advances in non-destructive testing based on 3D X-ray synchrotron tomography were used to capture the sequential response in granular media. High-pressure compression experiments with concurrent synchrotron X-ray tomography were conducted on packed sand samples. To measure the particle-scale attributes under continuous breakage, an algorithm was developed to track the sequence of breakage events stemming from compression, as well as the evolving morphology of the resulting fragments. Such method allowed the isolation of individual breakage events and the quantification of number and geometry of the fragments resulting from each grain rupture. Three modes of breakage (i.e., splitting, chipping, and comminution) were identified and

the breakage history of individual grains in the tested assembly was recorded into two types of failure events (i.e., incremental failure, accumulated failure). To quantify the evolving grain shape, three fitting protocols are proposed and used in conjunction with a tracking algorithm recording the breakage history of individual particles. This strategy enables detection of incremental breakage events, as well as quantification of correlations between the morphological properties before (parent particles) and after breakage (child particles). In addition, to extend the framework to assess the role of the particle shape on the macroscopic crushability of sand, the algorithm was used in combination with ellipsoidal fitting strategies able to track the evolution of three principal lengths and their associated aspect ratios in 3D both prior to and after crushing. The resulting non-spherical shape descriptors were incorporated into different contact laws, fracture criteria, and statistical failure models providing closed-form expressions of particle strength as a function of their size and shape. To corroborate the accuracy of these models against a series of compression experiments on Ottawa sand grains, laboratory experiments on grains characterized by varying geometry were conducted. Finally, LS-DEM simulation was performed to explore the evolving statistics of contact forces between particles in granular media during comminution. By creating level-set one-to-one particle replicas of an Ottawa sand from 3D tomography images, a virtual experiment replicating the compression response measured during a physical experiment was conducted. Through this exercise, the capability of LS-DEM to replicate the measurements was verified. In addition, the evolution of contact forces, not accessible through standard digital image analysis, was obtained as an outcome of the numerical analyses and used to explain the spatial and sequential characteristics of breakage nucleation across the specimen. The calibrated model was also used to examine the role of geometric model for the simulated particles on DEM predictions, as well as to examine the crushing response at stress levels higher than those applicable through

the testing setup used in this work. In the former case, emphasis was given to the optimal level of particle geometry representation that enables satisfactory model performance. In the latter case, the focus was on the possibility to track shape evolution at extreme stress levels, thus examining the possibility of attaining ultimate size and shape attractors.

The main conclusions deriving from these activities are summarized as follow:

1. It was found that particle strength is influenced by morphological attributes and its effect manifest in macroscopic assembly-scale properties, such as compressive yielding strength and grading evolution. Specifically, both experiments and new analytical models showed that the strength of particles tends to decrease by passings from subround to irregular shape.
2. At assembly-scale, the degree of grain shape evolution depends on the initial morphology of the particles, with subrounded particles exhibiting the most severe shape alterations. However, it was found that at high compressive stress all morphological indices approach similar values. Such a tendency is achieved when crushing involves primarily the finer grain fractions – that is, when cushioning hinders the rupture of larger particles.
3. It was revealed that comminution (i.e., the pervasive fragmentation of individual particles) was not achieved abruptly but was rather attained by way of successive stages of splitting and chipping regardless of particle-scale features such as shape.
4. The cushioning effect was verified quantitatively by examining the correlation between the size of parent particles and new incremental failure events. In particular, splitting and chipping mainly occurred into the finer, indicating cushioning effect for large grains from further breakage.

5. The shape distribution of fragments during continuous crushing of granular materials was explored and the shape of the fragments was quantified with different fitting methods. Even though the best fit principal length to particle diameter was found to depend on the selected fitting strategy, all methods show consistency in terms of evolution of the most significant shape features. It was also found that the principal lengths change sharply upon loading, but at a stress level which is higher than the macroscopic yield pressure, thus indicating that the conventional macroscopic response does not directly reflect the dynamics of particle shape evolution.
6. Regardless of the fitting strategy, it was shown that the most frequent morphology of the child particles is correlated with that of their corresponding parents. This phenomenon, here defined shape heritability, indicates that the fracture patterns responsible for size reduction vary with the shape of the parent particles.
7. Despite shape heritability, the measurements indicate non-symmetric shape dispersion curves skewed towards low aspect ratio values. This trend can be attributed to the prevalence of small fragments at high pressure, which under continuous breakage skew the distributions towards finer, more elongated shapes and cause evolution trends characterized by steady loss of particle regularity (i.e., morphological ratios departing from unity).
8. Analytical models incorporating both contact deformation and particle failure were proposed by using readily quantifiable principal lengths and their corresponding nondimensional ratios to incorporate elements of their non-spherical geometry. While all models displayed varying performance depending on the combination of particle size and shape, they also showed consistent trends of increasing strength with the aspect ratio (i.e., moderate elongation favor higher resistance) and decreasing strength with size (i.e., larger particles tend to be weaker).

9. It was shown through single particle compression tests that elongated grains tend to break at lower stress than spherical particles of equal size and that their strength depends more on their shape than their size. These results offer an experimental and analytical foundation to rationalize the effect of shape on the bulk crushability of granular materials.
10. LS-DEM was used to perform virtual oedometric experiments and quantify the evolution of inter-particle contact forces during simulated crushing events. It was found that large particles are more likely to carry contact forces of higher magnitude which tend to align along the vertical direction. This indicates that the specimen yielding resistance is determined primarily by the large forces acting along the loading direction. By contrast, the smaller fragments were found to carry forces of lower intensity and to support laterally the large particles by contributing to stabilize the strong force chains.
11. LS-DEM simulations were conducted to examine the performance of virtual specimens characterized by different levels of accuracy in the representation of sand grains scanned with X-ray tomography. It was shown that the use of ellipsoidal particles initialized with the goal to preserve the volume, aspect ratio, orientation, and gradation measured in the real sand specimen were able to replicate the compression response of the tested crushable sand in light of multiple metrics at both grain-scale and assembly-scale. This performance was comparable to that obtained through exact replicas of each sand grains, while being noticeably superior to that resulting from standard spherical models. These results suggests that the use of a limited range of shape indicators is a viable alternative to the exact rendering of the actual particle geometry, thus offering promising perspectives in terms of reducing the computational cost of DEM analyses.

8.2 Future Research Directions

Multiple future directions can be suggested as follow:

1. The experimental and numerical analyses explored in this thesis can be further expanded to encompass multi-physical forcing, such in case of fluid-saturated systems. While this study considers that dry granular materials under uniaxial compression, triaxial testing can also be used to measure shearing response accompanied by significant particle rotation and volume change, thus developing improved frameworks able to reconcile the effect of the pore fluid pressure evolution with the pore-scale kinematics.
2. This study focused on the comminution events tracked within small assemblies for which high-resolution synchrotron tomography was applicable. A future direction is to examine these processes through larger specimens able to increase the number of multi-particle interactions leading to collective emerging effects, at the cost of lower image resolution. Such perspective may enable an even broader examination of macroscopic response and comminution, which is ubiquitous in nature and technology. From a geophysical standpoint, it influences strain localization in granular rocks, the friction of fault gouge and sediment compaction. From a technological perspective, it is fundamental to a number of industries, ranging from mining to infrastructure development. Therefore, this work can be further extended to multi-scale experiments to elucidate the link between stress state, compaction, and comminution.
3. This study has mainly delved into shape distribution and shape heritability. These results can support the analysis of evolving shape characteristics in sand and of the role of particle-scale fractures in determining the ultimate morphology of particles in highly comminuted particle systems. Such results can be expanded in the future to examine more systematically the

underlying fracture mechanisms that promote shape heritability and the influence of multi-particle interactions in their manifestation.

4. Future applications of the proposed single particle failure models may involve the connection with continuum breakage frameworks based on the analytical determination of the strain energy associated with particle failure (an activity which involves the connection of each failure criterion with an underlying contact model, as already inherent for some of the derivations proposed here). This has the potential to bridge the macroscopic yielding stress of sand packing to grain scale processes and properties, including particle shape effects.
5. Along with the application of the proposed models, another perspective is to use the proposed analytical expressions in conjunction with discrete element modeling frameworks able to resolve the geometry of individual particles, thus feeding contact models (including particle failure criteria) with particle-specific geometric variables (e.g., aspect ratio, local curvature). Of course, while this study focused on the isolation of particle shape and size effects by employing grains from the same sand, it was recognized that this procedure led to inevitable restrictions in the range of global and local shape features used in the model verification process. As a result, a natural extension of this work will involve an expansion of the testing program to a broader set of particle geometries assessing the model performance in more diverse scenarios and possibly augment the models with further shape descriptors not considered in this study (e.g., local curvature, particle angularity).
6. DEM modeling techniques based on an extended set of particle shape descriptors, such as the LS-DEM platform used in this work, can be used in the future to complement experimental datasets either by providing quantities not accessible from direct measurements (e.g., contact forces) or by enabling virtual testing at stress levels currently not accessible through testing

apparatuses. These virtual measurements can be a springboard for the development of new constitutive laws for geomaterials rooted on the heterogeneity of sand microstructure, thus benefiting the geotechnical community at large. Such research outcome can provide guidance for engineering design, as well as new tools to reduce risks related with ground subsidence, fault seismicity, and long-term reservoir management.

REFERENCES

Afshar, P., Heidarian, S., Naderkhani, F., Oikonomou, A., Plataniotis, K. N., & Mohammadi, A. (2020). Covid-caps: A capsule network-based framework for identification of covid-19 cases from x-ray images. Pattern Recognition Letters, 138, 638-643.

Alikarami, R., Andò, E., Gkiousas-Kapnisis, M., Torabi, A., & Viggiani, G. (2015). Strain localisation and grain breakage in sand under shearing at high mean stress: insights from in situ X-ray tomography. Acta Geotechnica, 10(1), 15-30.

Alonso, E. E., Olivella, S., Soriano, A., Pinyol, N. M. & Esteban, F. (2011). Modelling the response of Lechago earth and rockfill dam. Géotechnique 61, No. 5, 387–407, https://doi.org/10.1680/geot.SIP11.P.013.

Alonso, E. E., Olivella, S., Soriano, A., Pinyol, N. M. & Esteban, F. (2011). Modelling the response of Lechago earth and rockfill dam. Géotechnique 61, No. 5, 387–407, https://doi.org/10.1680/geot.SIP11.P.013.

Alshibli, K. A., Druckrey, A. M., Al-Raoush, R. I., Weiskittel, T. & Lavrik, N. V. (2014). Quantifying morphology of sands using 3D imaging. J. Mater. Civ. Engng 27, No. 10, 04014275.

Alshibli, K., Cil, M. B., Kenesei, P., & Lienert, U. (2013). Strain tensor determination of compressed individual silica sand particles using high-energy synchrotron diffraction. Granular matter, 15(5), 517-530.

Altuhafi, F. N. & Coop, M. R. (2011). Changes to particle characteristics associated with the compression of sands. Géotechnique

Andò, E., Hall, S. A., Viggiani, G., Desrues, J., & Bésuelle, P. (2012). Grain-scale experimental investigation of localised deformation in sand: a discrete particle tracking approach. Acta Geotechnica, 7(1), 1-13.

Andrade, J. E., Avila, C. F., Hall, S. A., Lenoir, N. & Viggiani, G. (2011). Multiscale modeling and characterization of granular matter: from grain kinematics to continuum mechanics. J. Mech. Phys. Solids 59, No. 2, 237–250.

Anthony, J. L., & Marone, C. (2005). Influence of particle characteristics on granular friction. Journal of Geophysical Research: Solid Earth, 110(B8).

Antoine, J. F., Visa, C., Sauvey, C., & Abba, G. (2006). Approximate analytical model for Hertzian elliptical contact problems. Transactions of the ASME, DOI: 10.1115/1.2197850

Antonellini, M. A., Aydin, A. & Pollard, D. D. (1994). Microstructure of deformation bands in porous sandstones at Arches National Park, Utah. J. Struct. Geol. 16, No. 7, 941–959.

Arshad, M. I., Tehrani, F. S., Prezzi, M. & Salgado, R. (2014). Experimental study of cone penetration in silica sand using digital image correlation. Géotechnique 64, No. 7, 551–569, https://doi.org/10.1680/geot.13.P.179.

Bagheri, G. H., Bonadonna, C., Manzella, I., & Vonlanthen, P. (2015). On the characterization of size and shape of irregular particles. Powder Technology, 270, 141-153.

Barrett, P. J. (1980). The shape of rock particles: a critical review. Sedimentology 27, No. 3, 291–303

Ben-Nun, O., & Einav, I. (2010). The role of self-organization during confined comminution of granular materials. Philosophical Transactions of the Royal Society A: Mathematical, Physical and Engineering Sciences, 368(1910), 231-247.

Ben-Zion, Y. & Sammis, C. G. (2003). Characterization of fault zones. Pure Appl. Geophys. 160, No. 3, 677–715.

Bernard, D., Guillon, O., Combaret, N. & Plougonven, E. (2011). Constrained sintering of glass films: microstructure evolution assessed through synchrotron computed microtomography. Acta Mater. 59, No. 16, 6228–6238.

Blott, S.J., Pye, K. (2008). Particle shape: a review and new methods of characterization and classification. Sedimentology 55, 31–63

Brewe, D. E., & Hamrock, B. J. (1977). Simplified solution for elliptical-contact deformation between two elastic solids.

Bryant, M. D., & Keer, L. M. (1982). Rough contact between elastically and geometrically identical curved bodies. Trans. ASME J. Appl. Mech., 49(2, Jun. 1982), 345-352.

Brzesowsky, R. H., Spiers, C. J., Peach, C. J., & Hangx, S. J. T. (2011). Failure behavior of single sand grains: theory versus experiment. Journal of Geophysical Research: Solid Earth, 116(B6).

Buscarnera, G., & Einav, I. (2021). The mechanics of brittle granular materials with coevolving grain size and shape. Proceedings of the Royal Society A, 477(2249), 20201005.

Capaccioni, F., Cerroni, P., Coradini, M., Farinella, P., Flamini, E., Martelli, G., Paolicchi, P., Smith, P.N. and Zappala, V., (1984). Shapes of asteroids compared with fragments from hypervelocity impact experiments. Nature, 308(5962), 832-834.

Cavarretta, I., O'sullivan, C. & Coop,M. R. (2017). The relevance of roundness to the crushing strength of granular materials. Géotechnique 67, No. 4, 301–312, https://doi.org/10.1680/jgeot.15.P.226.

Cheng, Y. P., Nakata, Y., & Bolton, M. D. (2003). Discrete element simulation of crushable soil. Geotechnique, 53(7), 633-641.

Chester, J. S., Lenz, S. C., Chester, F. M. & Lang, R. A. (2004). Mechanisms of compaction of quartz sand at diagenetic conditions. Earth Planet. Sci. Lett. 220, No. 3, 435–451.

Cho, G. C., Dodds, J. & Santamarina, J. C. (2006). Particle shape effects on packing density, stiffness, and strength: natural and crushed sands. J. Geotech. Geoenviron. Engng 132, No. 5, 591–602.

Chuhan, F. A., Kjeldstad, A., Bjørlykke, K., & Høeg, K. (2002). Porosity loss in sand by grain crushing—Experimental evidence and relevance to reservoir quality. Marine and Petroleum Geology, 19(1), 39-53.

Chuhan, F. A., Kjeldstad, A., Bjrlykke, K. & Heg, K. (2003). Experimental compression of loose sands: relevance to porosity reduction during burial in sedimentary basins. Can. Geotech. J. 40, No. 5, 995–1011.

Cil, M. B., & Alshibli, K. A. (2014). 3D evolution of sand fracture under 1D compression. Géotechnique, 64(5), 351-364.

Cil, M. B., Hurley, R. C., & Graham-Brady, L. (2019). A rate-dependent constitutive model for brittle granular materials based on breakage mechanics. Journal of the American Ceramic Society, 102(9), 5524-5534.

Cil, M. B., Xie,M. & Packman, A. I. (2017). Solute mixing regulates heterogeneity of mineral precipitation in porous media: effect of solute mixing on precipitation. Geophys. Res. Lett. 44, No. 13, 6658–6666.

Coop, M. R., Sorensen, K. K., Bodas Freitas, T., & Georgoutsos, G. (2004). Particle breakage during shearing of a carbonate sand. Géotechnique, 54(3), 157-163.

Cundall, P. A., & Strack, O. D. (1979). A discrete numerical model for granular assemblies. geotechnique, 29(1), 47-65.

Das, A., & Bajpai, P. K. (2018). A hypo-plastic approach for evaluating railway ballast degradation. Acta Geotechnica, 13(5), 1085-1102.

Domokos, G., Kun, F., Sipos, A. A., & Szabó, T. (2015). Universality of fragment shapes. Scientific reports, 5(1), 1-6.

Donev, A., Cisse, I., Sachs, D., Variano, E.A., Stillinger, F.H., Connelly, R., Torquato, S. and Chaikin, P.M., (2004). Improving the density of jammed disordered packings using ellipsoids. Science, 303(5660), 990-993.

Dyson, A. (1965). Approximate calculations of Hertzian compressive stresses and contact dimensions. Journal of Mechanical Engineering Science, 7(2), 224-227.

Einav, I. (2007). Breakage mechanics – Part I: theory. J. Mech. Phys. Solids 55, No. 6, 1274–1297.

Farber, L., Tardos, G., & Michaels, J. N. (2003). Use of X-ray tomography to study the porosity and morphology of granules. Powder Technology, 132(1), 57-63.

FEI Company (2019). Avizo 3D image analysis software. Waltham, MA, USA: FEI Visualization Sciences Group.

Fonseca, J., O'sullivan, C., Coop, M. R., & Lee, P. D. (2012). Non-invasive characterization of particle morphology of natural sands. Soils and Foundations, 52(4), 712-722.

Frost, N. E., Marsh, K. J., & Pook, L. P. (1999). Metal fatigue. Courier Corporation.

Ganju, E., Kılıç, M., Prezzi, M., Salgado, R., Parab, N., & Chen, W. (2021). Effect of particle characteristics on the evolution of particle size, particle morphology, and fabric of sands loaded under uniaxial compression. Acta Geotechnica, 1-28.

Ghoraiby, M. E., Park, H., & Manzari, M. T. (2020). Physical and mechanical properties of Ottawa F65 sand. In Model tests and numerical simulations of liquefaction and lateral spreading (pp. 45-67). Springer, Cham.

Goddard, J. (1990). Nonlinear elasticity and pressure-dependent wave speeds in granular media. Proc. R. Soc. Lond. Ser. A: Math. Phys. Sci. 430, No. 1878, 105–131.

Goldenberg, C., & Goldhirsch, I. (2005). Friction enhances elasticity in granular solids. Nature, 435(7039), 188-191.

Gong, J., & Liu, J. (2017). Effect of aspect ratio on triaxial compression of multi-sphere ellipsoid assemblies simulated using a discrete element method. Particuology, 32, 49-62.

Greenwood, J. A. (1985). Formulas for moderately elliptical Hertzian contacts.

Gur, Y., Shklarsky, E., & Livneh, M. (1967). Effect of coarse-fraction flakiness on the strength of graded materials. In Asian Conf Soil Mech & Fdn E Proc/Is/.

Hagerty,M. M., Hite, D. R., Ullrich, C. R. & Hagerty, D. J. (1993). One-dimensional high-pressure compression of granular media. J. Geotech. Engng 119, No. 1, 1–18.

Harmon, J. M., Arthur, D., & Andrade, J. E. (2020). Level set splitting in DEM for modeling breakage mechanics. Computer Methods in Applied Mechanics and Engineering, 365, 112961.

Harmon, J. M., Seo, D., Buscarnera, G., & Andrade, J. E. (2022). Insight into Contact Forces in Crushable Sand using Experiments and Predictive Particle-Scale Modeling. Géotechnique, 1-35.

Hill, P. J. & Ng, K. M. (1996). Statistics of multiple particle breakage. AIChE J. 42, No. 6, 1600–1611.

Hiramatsu, Y. & Oka, Y. (1966). Determination of the tensile strength of rock by a compression test of an irregular test piece. Int. J. Rock Mech. Min. Sci. & Geomech. Abstr. 3, No. 2, 89–90.

Hiramatsu, Y., & Oka, Y. (1966). Determination of the tensile strength of rock by a compression test of an irregular test piece. In International Journal of Rock Mechanics and Mining Sciences & Geomechanics Abstracts (Vol. 3, No. 2, pp. 89-90). Pergamon.

Hurley, R. C., Lind, J., Pagan, D. C., Akin, M. C. & Herbold, E. B. (2018). In situ grain fracture mechanics during uniaxial compaction of granular solids. J. Mech. Phys. Solids 112, 273–290.

Ikeda, S., Nakano, T., & Nakashima, Y. (2000). Three-dimensional study on the interconnection and shape of crystals in a graphic granite by X-ray CT and image analysis. Mineralogical Magazine, 64(5), 945-959.

Indraratna, B., Ionescu, D. & Christie, H. D. (1998). Shear behavior of railway ballast based on large-scale triaxial tests. J. Geotech. Geoenviron. Engng 124, No. 5, 439.

ISO (2007) 14688-1: 2017: Geotechnical investigation and testing – Identification and classification of soil – Part 1: Identification and description. Geneva, Switzerland: ISO.

ISO (2008). ISO 9276-6:2008: Representation of results of particle size analysis – Part 6: Descriptive and quantitative representation of particle shape and morphology. Geneva, Switzerland: ISO

Jäger, J. (1999). Uniaxial deformation of a random packing of particles. Arch. Appl. Mech. 69, No. 3, 181–203.

Karatza, Z. (2017). A study of temporal and spatial evolution of deformation and breakage of dry granular materials using X-ray computed tomography and the discrete element method. PhD thesis, The University of Edinburgh, Edinburgh, UK.

Karatza, Z., Ando, E., Papanicolopulos, S. A., Ooi, J. Y., & Viggiani, G. (2018). Evolution of deformation and breakage in sand studied using X-ray tomography. Géotechnique, 68(2), 107-117.

Karatza, Z., Andò, E., Papanicolopulos, S. A., Viggiani, G. & Ooi, J. Y. (2019). Effect of particle morphology and contacts on particle breakage in a granular assembly studied using X-ray tomography. Granul. Matter 21, No. 3, 44.

Kassir,M. & Sih, G. C. (1966). Three-dimensional stress distribution around an elliptical crack under arbitrary loadings. J. Appl. Mech. 33, No. 3, 601–611.

Katagiri, J., Matsushima, T., & Yamada, Y. (2010). Statistics on 3D particle shapes of lunar soil (No. 60501) obtained by micro x-ray CT and its image-based DEM simulation. In Earth and Space 2010: Engineering, Science, Construction, and Operations in Challenging Environments (pp. 254-259).

Katagiri, J., Matsushima, T., Yamada, Y., Tsuchiyama, A., Nakano, T., Uesugi, K., Ohtake, M., & Saiki, K. (2015). Investigation of 3D grain shape characteristics of lunar soil retrieved in Apollo 16 using image-based discrete-element modeling. Journal of Aerospace Engineering, 28(4), 04014092.

Kendall, K. (1978). The impossibility of comminuting small particles by compression. Nature 272, No. 5655, 710.

Kim, J. H., Ochoa, J. A., & Whitaker, S. (1987). Diffusion in anisotropic porous media. Transport in porous media, 2(4), 327-356.

Krumbein, W. C. (1941). Measurement and geological significance of shape and roundness of sedimentary particles. Journal of Sedimentary Research, 11(2), 64-72.

Le Pen, L. M., Powrie, W., Zervos, A., Ahmed, S., & Aingaran, S. (2013). Dependence of shape on particle size for a crushed rock railway ballast. Granular Matter, 15(6), 849-861.

Lei, W. S., Qian, G., Yu, Z., & Berto, F. (2019). Statistical size scaling of compressive strength of quasi-brittle materials incorporating specimen length-to-diameter ratio effect. Theoretical and Applied Fracture Mechanics, 104, 102345.

Li, D., Li, Y., Wang, Z., Wang, X., & Li, Y. (2016). Quantitative, SEM-based shape analysis of sediment particles in the Yellow River. International Journal of Sediment Research, 31(4), 341-350.

Liu, Z., & Zhao, Y. (2020). Multi-super-ellipsoid model for non-spherical particles in DEM simulation. Powder Technology, 361, 190-202.

Mair, K., Frye, K. M., & Marone, C. (2002). Influence of grain characteristics on the friction of granular shear zones. Journal of Geophysical Research: Solid Earth, 107(B10), ECV-4.

Marone, C., Vidale, J. E. & Ellsworth, W. L. (1995). Fault healing inferred from time dependent variations in source properties of repeating earthquakes. Geophys. Res. Lett. 22, No. 22, 3095–3098.

Marsal, R. J. (1967). Large scale testing of rockfill materials. Journal of the Soil Mechanics and Foundations Division, 93(2), 27-43.

Masson, S., & Martinez, J. (2000). Effect of particle mechanical properties on silo flow and stresses from distinct element simulations. Powder Technology, 109(1-3), 164-178.

McDowell, G. (2002). On the yielding and plastic compression of sand. Soils Found. 42, No. 1, 139–145.

McDowell, G. R., & Bolton, M. D. (1998). On the micromechanics of crushable aggregates. Géotechnique, 48(5), 667-679.

McDowell, G. R., & de Bono, J. P. (2013). On the micro mechanics of one-dimensional normal compression. Géotechnique, 63(11), 895-908.

Mitchell, J. K. & Soga, K. (2005). Fundamentals of soil behavior, 3rd edn,. New York, USA: Wiley

Moss, A. J. (1972). Technique for assessment of particle breakage in natural and artificial environments. Journal of Sedimentary Research, 42(3), 725-728.

Nakata, A., Hyde,M. & Hyodo,H. (1999). A probabilistic approach to sand particle crushing in the triaxial test. Géotechnique 49, No. 5, 567–583, http://dx.doi.org/10.1680/geot.1999.49.5.567.

Nakata, Y., Kato, Y., Hyodo, M., Hyde, A. F., & Murata, H. (2001). One-dimensional compression behaviour of uniformly graded sand related to single particle crushing strength. Soils and foundations, 41(2), 39-51.

Ng, T. T. (2009). Particle shape effect on macro-and micro-behaviors of monodisperse ellipsoids. International journal for numerical and analytical methods in geomechanics, 33(4), 511-527.

Oldecop, L. A., & Alonso, E. E. (2001). A model for rockfill compressibility. Géotechnique, 51(2), 127-139.

Pestana, J. M., & Whittle, A. J. (1995). Compression model for cohesionless soils. Géotechnique, 45(4), 611-631.

Pestana, J. M., & Whittle, A. J. (1995). Compression model for cohesionless soils. Géotechnique, 45(4), 611-631.

Radjai, F., Roux, S., & Moreau, J. J. (1999). Contact forces in a granular packing. Chaos: An Interdisciplinary Journal of Nonlinear Science, 9(3), 544-550.

Reid Kawamoto, Edward Andò, Gioacchino Viggiani, & José E. Andrade, (2016). Level set discrete element method for three-dimensional computations with triaxial case study, J. Mech. Phys. Solids 91 1–13.

Rivers, M. L. (2012). Tomorecon: high-speed tomography reconstruction on workstations using multi-threading. In Proceedings of the International Society for Optical Engineering (SPIE), vol. 8506, pp. 85060U–85060U-13. San Diego, CA, USA: SPIE.

Rivers, M. L. (2016). High-speed tomography using pink beam at GeoSoilEnviroCARS. In Proceedings of the International Society for Optical Engineering (SPIE), vol. 9967, pp. 99670X–99670X-10. San Diego, CA, USA: SPIE.

Rothenburg, L., & Bathurst, R. J. (1991). Numerical simulation of idealized granular assemblies with plane elliptical particles. Computers and geotechnics, 11(4), 315-329.

Sandeep, C. S., & Senetakis, K. (2018). Effect of Young's modulus and surface roughness on the inter-particle friction of granular materials. Materials, 11(2), 217.

Santamarina, J. C., & Cho, G. C. (2004). Soil behaviour: The role of particle shape. In Advances in geotechnical engineering: The Skempton conference: Proceedings of a three day conference on advances in geotechnical engineering, organised by the Institution of Civil Engineers and held at the Royal Geographical Society, London, UK, on 29–31 March 2004 (pp. 604-617). Thomas Telford Publishing.

Seo, D., Sohn, C., Cil, M. B., & Buscarnera, G. (2020). Evolution of particle morphology and mode of fracture during the oedometric compression of sand. Géotechnique, 0(0), 1–13. https://doi.org/10.1680/jgeot.18.P.300

Shahin, G., Viggiani, G., & Buscarnera, G. (2020). Simulating spatial heterogeneity through a CT-FE mapping scheme discloses boundary effects on emerging compaction bands. International Journal of Solids and Structures, 206, 247-261.

Shin, H., & Santamarina, J. C. (2013). Role of particle angularity on the mechanical behavior of granular mixtures. Journal of Geotechnical and Geoenvironmental Engineering, 139(2), 353-355.

Sohn, C., Zhang, Y. D., Cil, M., & Buscarnera, G. (2017). Experimental assessment of continuum breakage models accounting for mechanical interactions at particle contacts. Granular Matter, 19(4), 67.

Tanaka, N. (2001). A new calculation method of Hertz elliptical contact pressure. J. Trib., 123(4), 887-889.

Tang, C. A., Xu, X. H., Kou, S. Q., Lindqvist, P. A., & Liu, H. Y. (2001). Numerical investigation of particle breakage as applied to mechanical crushing—part I: single-particle breakage. International journal of rock mechanics and mining sciences, 38(8), 1147-1162.

Tang, C. A., Xu, X. H., Kou, S. Q., Lindqvist, P. A., & Liu, H. Y. (2001). Numerical investigation of particle breakage as applied to mechanical crushing—part I: single-particle breakage. International journal of rock mechanics and mining sciences, 38(8), 1147-1162.

Tenthorey, E., Cox, S. F. & Todd, H. F. (2003). Evolution of strength recovery and permeability during fluid–rock reaction in experimental fault zones. Earth Planet. Sci. Lett. 206, No. 1–2, 161–172.

Timoshenko, S. & Goodier, J. (1951). Theory of elasticity, p. 412. New York, NY, USA: McGraw-Hill.

Ting, J. M., Khwaja, M., Meachum, L. R., & Rowell, J. D. (1993). An ellipse-based discrete element model for granular materials. International Journal for numerical and analytical methods in geomechanics, 17(9), 603-623.

Ting, J. M., Khwaja, M., Meachum, L. R., & Rowell, J. D. (1993). An ellipse-based discrete element model for granular materials. International Journal for numerical and analytical methods in geomechanics, 17(9), 603-623.

Todisco, M. C., Wang, W., Coop, M. R. & Senetakis, K. (2017). Multiple contact compression tests on sand particles. Soils and Foundations 57, No. 1, 126{140, doi: 10.1016/j.sandf.2017.01.009. 20, 53, 60, 66, 110, 162

Tsuchiyama, A., Uesugi, M., Matsushima, T., Michikami, T., Kadono, T., Nakamura, T., Uesugi, K., Nakano, T., Sandford, S.A., Noguchi, R. and Matsumoto, T., (2011). Three-dimensional structure of Hayabusa samples: origin and evolution of Itokawa regolith. science, 333(6046), 1125-1128.

Tudisco, E., Andò, E., Cailletaud, R., & Hall, S. A. (2017). TomoWarp2: A local digital volume correlation code. SoftwareX, 6, 267-270.

Tuitz, C., Exner, U., Frehner, M., & Grasemann, B. (2012). The impact of ellipsoidal particle shape on pebble breakage in gravel. International Journal of Rock Mechanics and Mining Sciences, 54, 70-79.

Ueda, T.,Matsushima, T. & Yamada, Y. (2013). DEM simulation on the one-dimensional compression behavior of various shaped crushable granular materials. Granul. Matter 15, No. 5, 675–684.

Unland, G. (2007). The principles of single-particle crushing. Handbook of Powder Technology, 12, 117-225.

Viggiani, G., Andò, E., Takano, D., & Santamarina, J. C. (2015). Laboratory X-ray tomography: a valuable experimental tool for revealing processes in soils. Geotechnical Testing Journal, 38(1), 61-71.

Wadell, H. (1932). Volume, shape and roundness of rock particles. J. Geol. 40, No. 5, 443–451.

Wadell, H. (1935). Volume, shape, and roundness of quartz particles. J. Geol. 43, No. 3, 250–280.

Walton, W. H. (1948). Feret's statistical diameter as a measure of particle size. Nature 162, No. 4113, 329.

Wan, J., Chen, Z., Chu, X., & Liu, H. (2020). Dependency of single-particle crushing patterns on discretization using peridynamics. Powder Technology, 366, 689-700.

Wang, W. & Coop, M. R. (2016). An investigation of breakage behaviour of single sand particles using a high-speed microscope camera. Géotechnique 66, No. 12, 984–998, https://doi.org/10.1680/jgeot.15.P.247.

Weibull, W. (1951). A statistical distribution function of wide applicability, J. Appl. Mech., 18, 293–297.

Wiącek, J., Molenda, M., Horabik, J., & Ooi, J. Y. (2012). Influence of grain shape and intergranular friction on material behavior in uniaxial compression: Experimental and DEM modeling. Powder Technology, 217, 435-442.

Xia, X., Zhou, L., Ma, H., Xie, C., & Zhao, Y. (2022). Reliability study of super-ellipsoid DEM in representing the packing structure of blast furnace. Particuology.

Xue, D., Shahin, G., Seo, D., Lü, X., & Buscarnera, G. (2022). Simulation of heterogeneous breakage in sand based on full-field X-ray tomography measurements. Computers and Geotechnics, 147, 104746.

Yang, J., & Luo, X. D. (2015). Exploring the relationship between critical state and particle shape for granular materials. Journal of the Mechanics and Physics of Solids, 84, 196-213.

Yang, Z. X., Jardine, R. J., Zhu, B. T., Foray, P. & Tsuha, C. H. C. (2010). Sand grain crushing and interface shearing during displacement pile installation in sand. Géotechnique 60, No. 6, 469–482, https://doi.org/10.1680/geot.2010.60.6.469.

Yao, T., Baudet, B. A., & Lourenço, S. D. (2021). Evolution of surface roughness of single sand grains with normal loading. Géotechnique, 1-13.

Yashima, S., Kanda, Y. & Sano, S. (1987). Relationships between particle size and fracture energy or impact velocity required to fracture as estimated from single particle crushing. PowderTechnol. 51, No. 3, 277–282.

Yury (2021). Ellipsoid fit (https://www.mathworks.com/matlabcentral/ fileexchange/24693-ellipsoid-fit), MATLAB Central File Exchange. Retrieved September 1, 2021.

Zhang, J., Wong, T. F. & Davis, D. M. (1990). Micromechanics of pressure-induced grain crushing in porous rocks. J. Geophys. Res.: Solid Earth (1978–2012) 95, No. B1, 341–352.

Zhang,Y.D., Buscarnera,G. &Einav, I. (2016). Grain size dependence of yielding in granular soils interpreted using fracture mechanics, breakage mechanics and Weibull statistics. Géotechnique 66, No. 2, 149–160, https://doi.org/10.1680/jgeot.15.P.119.

Zhao, B., & Wang, J. (2016). 3D quantitative shape analysis on form, roundness, and compactness with μCT. Powder technology, 291, 262-275.

Zhao, B., Wang, J., Andò, E., Viggiani, G., & Coop, M. R. (2020). Investigation of particle breakage under one-dimensional compression of sand using X-ray microtomography. Canadian Geotechnical Journal, 57(5), 754-762.

Zhao, B., Wang, J., Andò, E., Viggiani, G., & Coop, M. R. (2020). Investigation of particle breakage under one-dimensional compression of sand using X-ray microtomography. Canadian Geotechnical Journal, 57(5), 754-762.

Zhao, B., Wang, J., Coop, M. R., Viggiani, G. & Jiang, M. (2015). An investigation of single sand particle fracture using X-ray micro-tomography. Géotechnique 65, No. 8, 625–641, https://doi.org/10.1680/geot.4.P.157.

Zheng, J., & Hryciw, R. D. (2015). Traditional soil particle sphericity, roundness and surface roughness by computational geometry. Géotechnique, 65(6), 494-506.

Zheng, J., Sun, Q., Zheng, H., Wei, D., Li, Z., & Gao, L. (2020). Three-dimensional particle shape characterizations from half particle geometries. Powder Technology, 367, 122-132.

Zhu, F., & Zhao, J. (2019). Modeling continuous grain crushing in granular media: A hybrid peridynamics and physics engine approach. Computer Methods in Applied Mechanics and Engineering, 348, 334–355. https://doi.org/10.1016/j.cma.2019.01.017

Zhu, F., & Zhao, J. (2021). Interplays between particle shape and particle breakage in confined continuous crushing of granular media. Powder Technology, 378, 455-467.

Zingg, T. (1935) Beitrag zur schotteranalyse. Schweiz. Mineral.Petrogr. Mitt., 15, 39–140

APPENDIX A: OEDOMETRIC TEST FOR SAMPLE-SIZE EFFECTS

Image analysis is one of powerful non-destructive tools to observe the sequential response of materials. The challenge here is to explore the microscopic features in the system, high resolution is required while limiting the sample size. In granular materials, Masson & Martinez (2000) concluded that a sample size 7-8 times the largest particle size can show the macroscopic features such as porosity and coordination number. However, it is still insufficient to address the considerations in comparison to different size samples and mechanical system quantitatively. In this section, the preliminary results of comparison between two different size sample are discussed.

A.1 Oedometric test of the two different size sample

Oedometric tests were performed with two different size sample having 0.65 of void ratio, e_0, small specimen with 4.2 mm of diameter (409 particles) and large specimen with 15 mm of diameter (14,984 particles) (Figure A.1), large specimen has approximately 36 times larger system than the tested small sample. scan those sample, the tests were conducted in conjunction with tomography at two facilities, Argonne National Laboratory, Illinois, USA and Laboratorie 3SR, Grenoble, France, respectively (details in Chapter 2). Both samples were prepared in PEEK cylindrical cells to minimize the boundary effects and the test condition was same to 0.05 mm/min by strain control. To The small sample was scanned with 4.28 μm/pixel and the image resolution for larger one was 13.5 μm/pixel. Both samples were scanned at the specific stress points (0, 10, 20, 30, 40 and 50 MPa).

(a) (b)

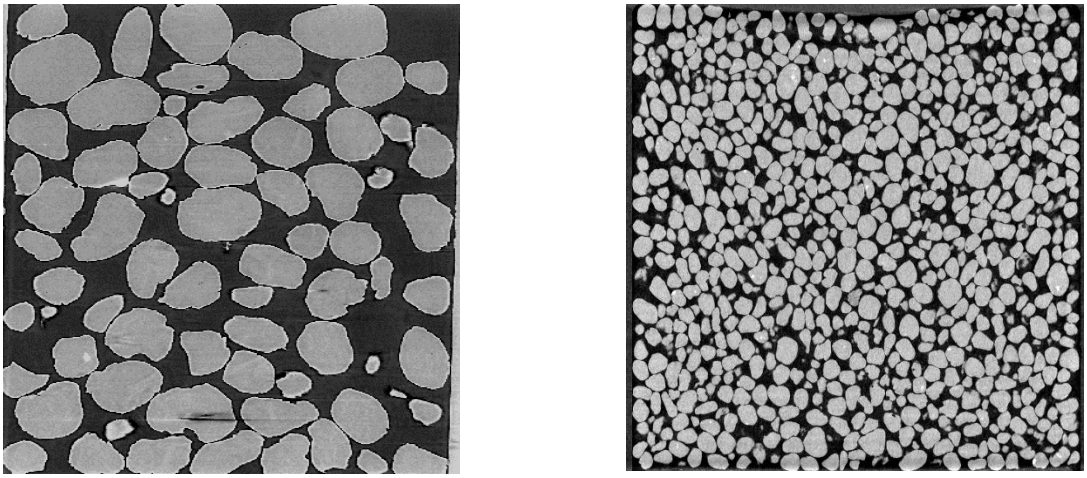

Figure A.1. (a) Small specimen (with 4.2 mm of sample diameter) (b) Large specimen (with 15 mm of sample diameter)

Figure A.2a shows the GSD for the tested sample having very close distributions regardless the sample size. Despite the identical GSD in the sample, the constitutive responses were different depending on the sample size. Figure A.2b plots the stress-strain curve under uniaxial compression test and small specimen display lightly stiffer response in pre-yielding regime. In addition, the yielding appears slightly early in small sample. In small specimen, it was observed that the particle breakage concentrated near the top of the specimen inducing the higher stiffness in that the stress near the loading plate tends to propagate strongly toward horizontal direction and results in the higher stiffness by interacting the side walls (Zhu & Zhao., 2021). While the constitutive response under continuous loading is still reasonably matched, the significant gap caused by size differences was the response for unloading. The permanent deformation after unloading was much higher in small sample than large sample.

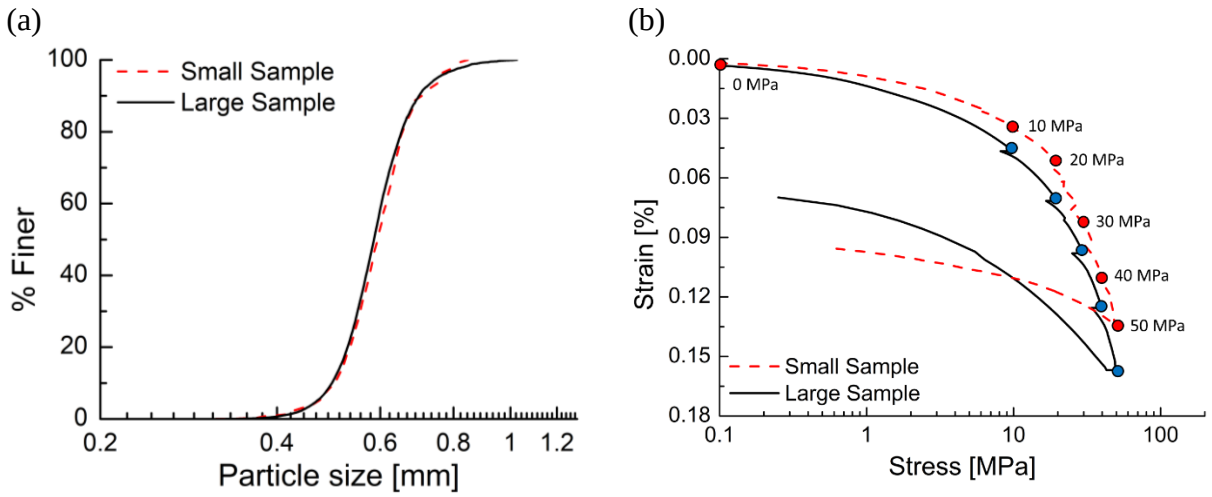

Figure A. 2. GSD of the tested particle at initial condition

A.2 Image analysis for sample-size effect

Figure A.3a shows the distribution of probability for coordination quantified through image analysis. The coordination shows similar distribution, but the large sample has higher coordination number (the average of coordination number is 7.15 with 18 of the highest coordination) than that of small sample (the average of coordination number is 6.94 with 13 of the highest coordination number). It is assumed that in case of the small sample the relatively more particles contacting to the cylindrical walls, inducing the less coordination number in the average. Therefore, such difference can be considered one of the boundary effects caused by the sample size. In both cases, the breakage initiates at 10 MPa and the ratio of breakage was 0.22 % and 0.24 % in the large and the small sample, respectively. Those breakage were concentrated near the loading plate in the sample while it was distributed to the overall specimen in the large sample. This boundary effect to the sample interrupts finding some phenomena. For example, Figure A.3b shows the comparison of coordination between the entire particles and the original particles which experiences breakage in the next step in case of only large sample. It was clear that breakage tends to initiate when the particles have less coordination than the other particles in the assembly. Note that the small sample

was not analyzed due to the breakage concentrating the particles contacting the loading plates. In conclusion, such preliminary results indicate that sample-size effect is mainly induced by the boundary effect, however further research in the sample-size effect in the granular system is required to elucidate the geomechanical response of granular system.

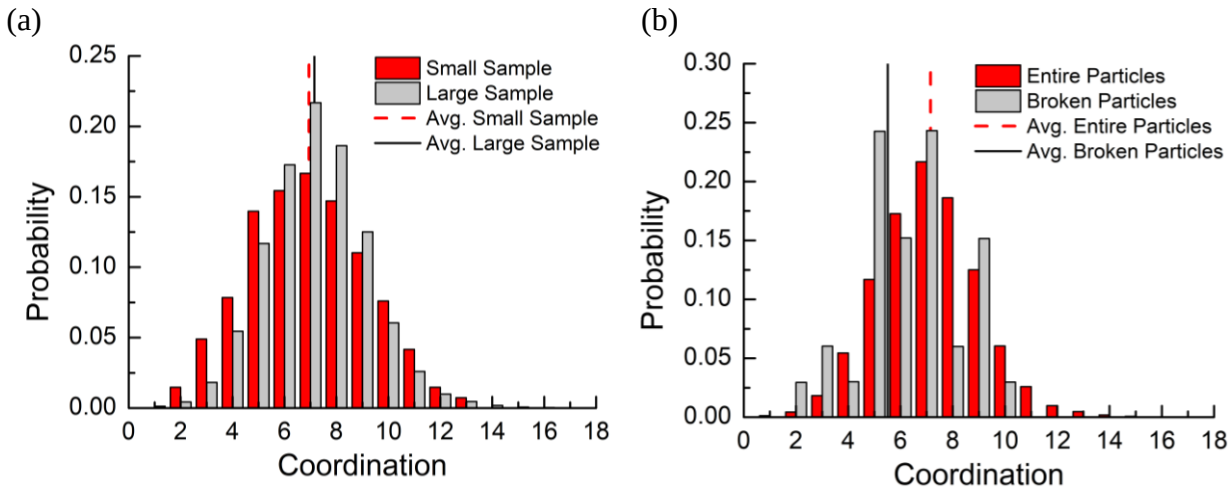

Figure A.3. Probability for coordination of (a) the entire particles in two different size sample and (b) comparison with the broken particles in the large sample

APPENDIX B: NETWORK MODEL

Network model is a statistical tool allowing characterizing the critical factors affecting the response in the system. This model describes a complex system through nodes (i.e., particles) and edges (i.e., contacts between particles). In this study, the particle-based networks were explored as preliminary research aiming to provide the fingerprint at microscale in granular system with the experimental results of oedometric test with Ottawa sand. For this purpose, the unweighted network model was assessed, which is a simple method to express the existence of binary interaction between nodes in the system.

Two oedometer tests were conducted under strain control (0.05 mm/min of displacement rate) in the sample with 4.2 mm of diameter and 8 mm of height. Figure B.1 shows the stress-strain curve of both tests having 29 MPa of yield stress and the markers indicate the scan points with 7 % of strain interval. To correlate the response between assembly-scale (i.e., stress-strain) and particle-scale (i.e., breakage, degree (coordination)), image analysis was conducted for the sequentially obtained scans.

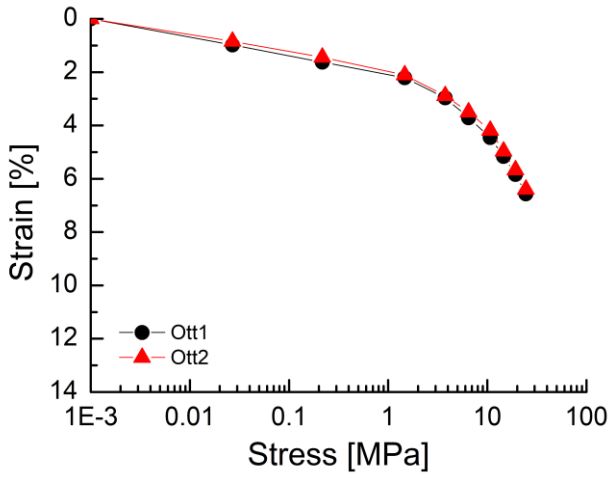

Figure B.1. Stress-strain curve with scans

Figure B.2a presents the evolution of connectivity where ε is strain, ε_d is strain at initiation of breakage, z_0 is an initial value of mean connectivity and z is mean degree. The connectivity developed until the initiation of breakage (at $\varepsilon_d - \varepsilon_d = 0$) and tended to decrease after reaching the yield point ($\varepsilon_d - \varepsilon_d > 0$). It is seemed that the degree decreases as damage proceeds in that the increasing number of small fragments under successive breakage contributes to reduction of the degree on average. The mean shortest-path distance *l* of a pair of nodes is an average value of the summing edges on the shortest distance between two nodes. Figure B.2b plots the normalized mean shortest-path distance with the initial mean value, l_0. It shows the reduction until the yield point and presents the sharp increase. This means that *l* between nodes decreases as the granular system is compacted under the load and then fragments which are significantly generated in the post-yielding regime lengthened *L*.

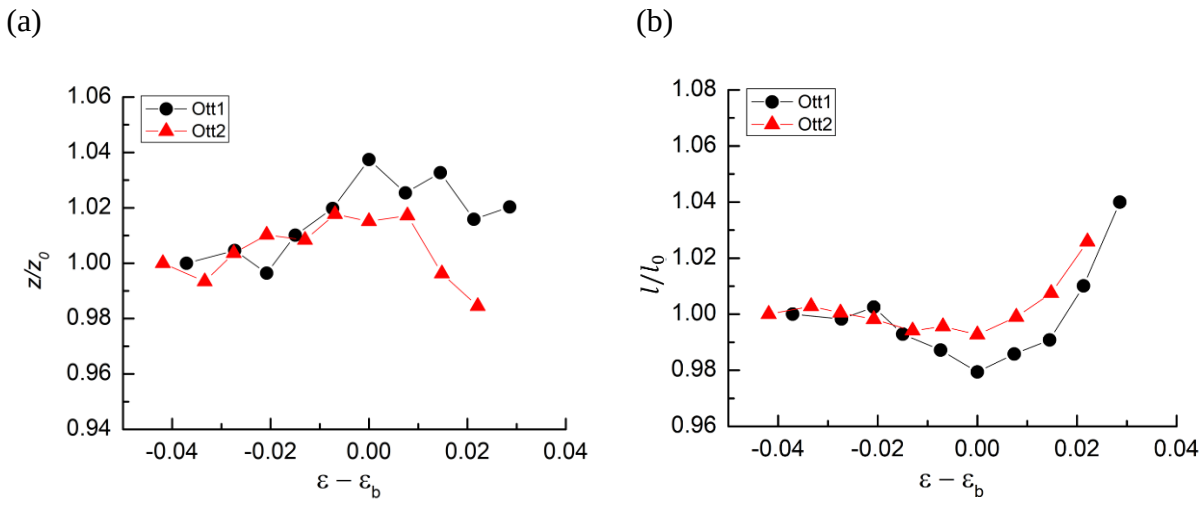

Figure B.2. Experimental results for (a) normalized degree, $\boldsymbol{z/z_0}$ and (b) normalized mean shortest-path distance, $\boldsymbol{l/l_0}$

One of the network properties, betweenness centrality (BC) was calculated to quantify the contribution in the shortest paths across pair particles, presenting the importance of particular nodes, edges or other structures in a network. As an example, the heterogeneity of force patterns

in granular networks can be shown through distribution of betweenness centrality. With the calculated BC, particle volume and degree, the correlation was explored with spearman coefficient (Figure B.3). Spearman coefficient is a statistical measure of the strength of a monotonic relationship between paired values having strong correlation towards +1. As shown in Figure B.3, overall tendency of both cases displays increasing coefficient after the yield, having stronger correlation in volume-BC and volume-degree. Such results can contribute to setting the order of the contribution of the key variables to the onset of breakage to conduct the following step.

(a) (b)

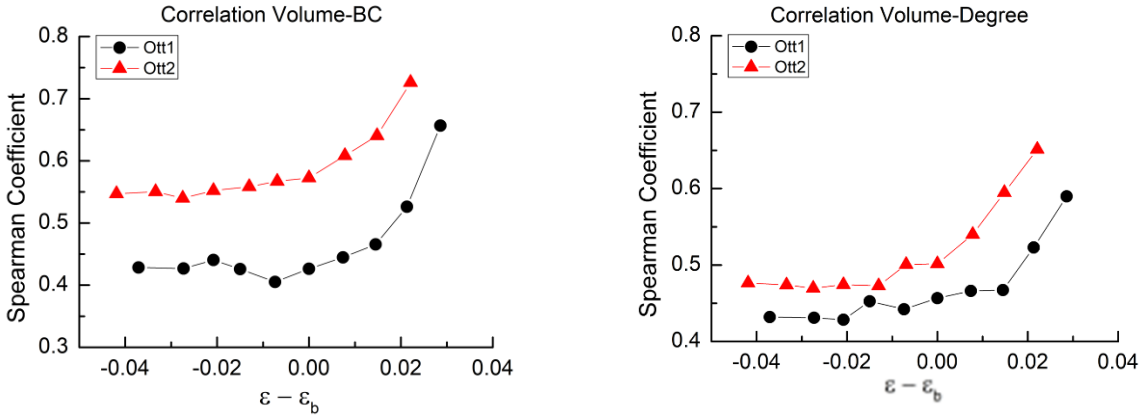

Figure B.3. Correlation between (a) volume and BC and (b) volume and degree

APPENDIX C: COMPUTERZIED-TOMOGRAPHY TO FINITE-ELEMENT (CT-FE)

This section discusses the application of scanned images of granular materials to continuum-scale computational model conducted in Xue et al., 2021 considering evolving microscale attributes under continuous breakage. To consider the initial field heterogeneities and boundary conditions of crushable granular materials in continuum-scale model, the computerized-tomography to finite-element (CT-FE) was performed based on the concept of representative elementary volume (REV). By confirming the performance of linking two different features of domains, it shows the possibility of future study to link microscopic mechanics to macroscopic continuum.

C.1 Porosity-dependent Continuum Breakage Mechanics

To predict the response of granular materials in continuum scale, continuum breakage mechanics is adapted by introducing breakage index, B to yield function, y_B (discussed in Chapter 2). However, to explore the post-yielding region, the continuum breakage was extended to involve breakage and plastic strain corresponding to breakage. The extended flow rules for those viscoplastic responses as follows:

$$dB = \Phi \frac{2(1-B)^2 cos^2\omega}{E_c} \tag{C.1}$$

$$d\varepsilon_{ij}^{vp} = \Phi \left[-2 \frac{(1-B)^2 E_B sin^2\omega}{pE_c} \frac{\delta_{ij}}{3} + \frac{3s_{ij}}{M^2 p^2} \right] \tag{C.2}$$

where $d\varepsilon_{ij}^{vp}$ is the rate of viscoplastic strain tensor and ω is the breakage-friction coupling angle.

With those parameters, the rate of energy dissipation of the system, Φ can be obtained with yield function y_B in the McCauley brackets and breakage growth rate $\dot{B}$,

$$\Phi = \frac{E_c \dot{B}_0}{2(1-B)^2} \langle y_B^{\frac{n}{2}} \rangle \tag{C.3}$$

where n is the stress corrosion value and B_0 is the reference breakage index. The details of derivations and the engineering meaning can be found in Xue et al., 2021.

C.2 Mapping of X-ray Image to Finite Element

To perform the breakage response of granular materials under odometric compression through CT-FE, the initial spatial heterogeneities of granular system was replicated with the obtained X-ray tomography in Chapter 5. The important feature in this activity is the concept of REV to transfer the measured attributes from experiments into Gauss integration points in FE simulations (Figure C.1a). The average experimental measurements are assigned to each Gauss integration point in their corresponding REVs. Note that REV size can be determined as the minimum size of window box enabling allocated REVs in the overall sample domain to result consistent value (detailed in Shahin et al., 2020). Through REV using tomography images, the realistic description of the initial spatial heterogeneities in granular materials can be preserved in CT-FE. The general FE simulation conditions were designed by considering the experimental features. In experiments, it was found that the boundary condition influence significantly to breakage in granular system (Karatza et al, 2019) and this was reflected in the CT-FE as shown in Figure C.1b. In specific, the floating ring used in experiment was considered in that this strategy prevent deformation to the radial direction while minimizing the friction effect between wall and particles.

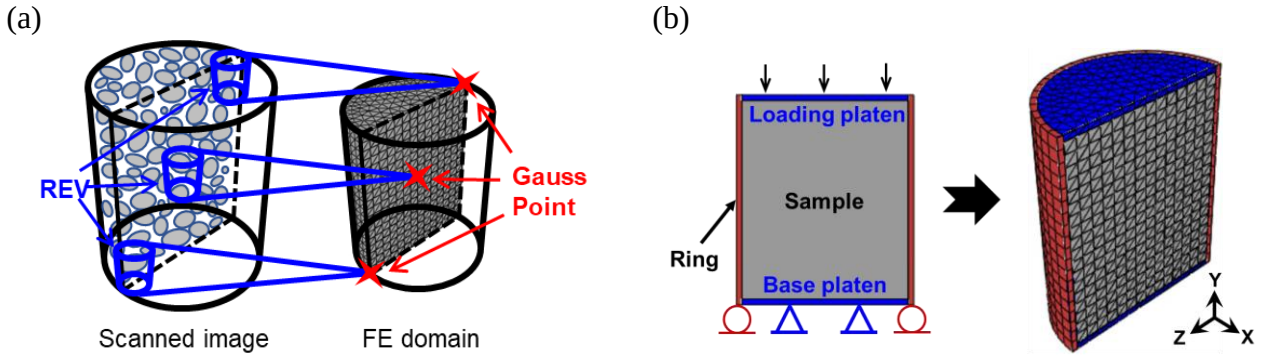

Figure C.1. (a) Schematic of CT-FE mapping to assign each Gauss integration point with the corresponding REV from X-ray CT images (b) computational domain with boundary conditions and discretized FE meshes

C.3 CT-FE Mapping Scheme Oedometric Compression

The constitutive response is well predicted by CT-FE as shown in Figure C.2. Next, the performance of computational model incorporating initial spatial heterogeneities was assessed by qualitatively comparing the spatial heterogeneities at the same point of scanning points associated with experiments over time (Figure C.2).

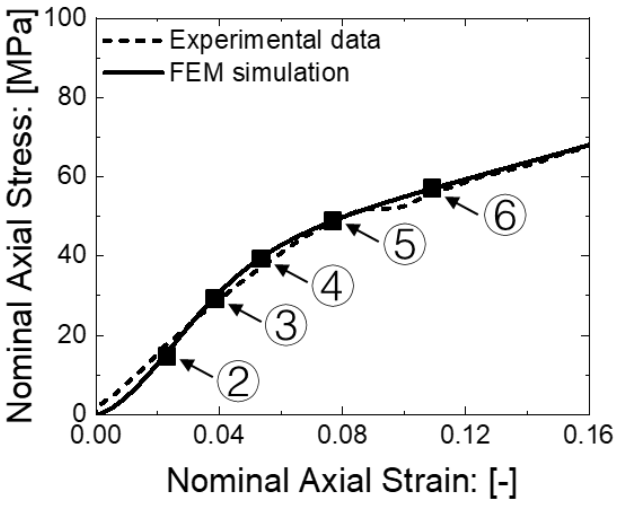

Figure C.2. Mechanical response compared to experiment and FEM simulation

Figure C.3 shows the one of the representative results showing the correspondence between experimental and computational results. The porosity field, ϕ and the breakage index, B were

explored, and evolution of both fields mapped in Figure C.3 presents a satisfactory match in the spatial distribution of heterogeneities over time. This indicates that particle breakage propagation can be captured reasonably by CT-FE based on continuum mechanics.

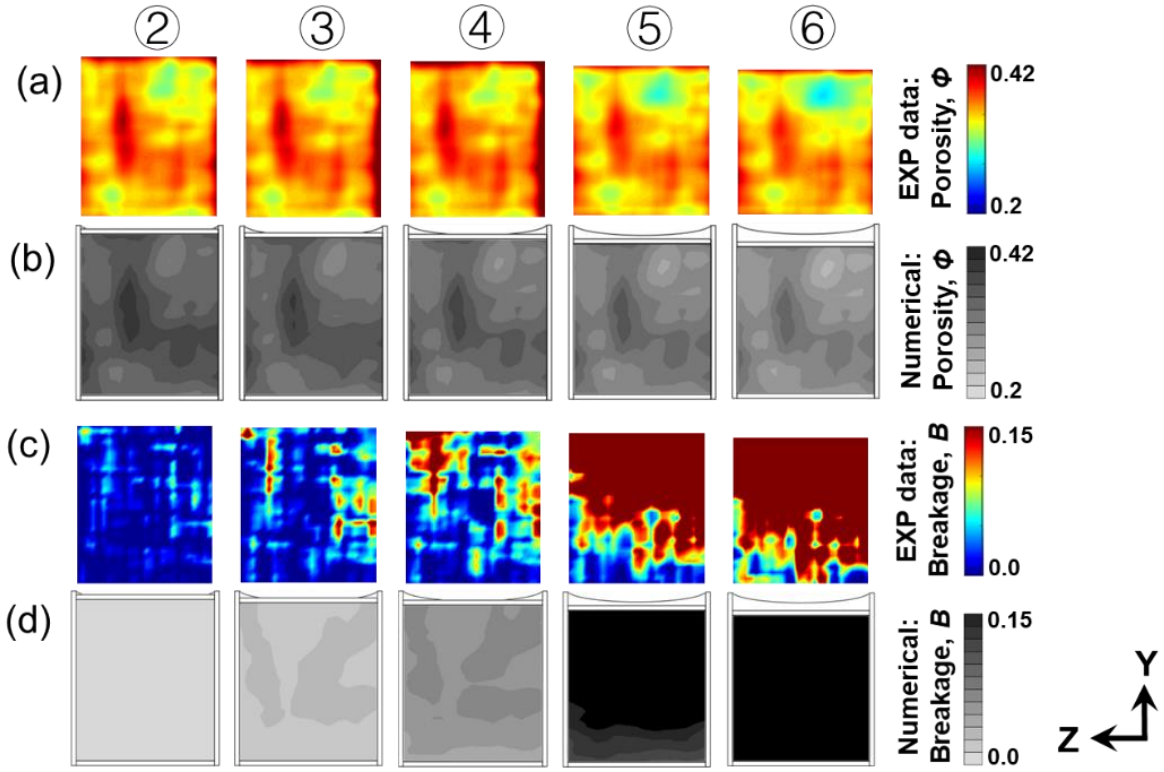

Figure C.3. Comparisons in porosity field, $\boldsymbol{\phi}$ between (a) experimental data and (b) numerical simulations, and breakage field, B between (c) experimental data and (d) numerical simulations.